An assessment of alkali metal-O_2 chemistry: perspectives and prospectives

Honorio Valdés Espinosa de los Monteros

A dissertation
submitted in partial fulfillment of the
requirements for the degree of

Doctor of Philosophy

University of Washington

2018

Reading Committee:

Stuart B. Adler, Chair

Eric M. Stuve, Chair

Charles T. Campbell

Program Authorized to Offer Degree:
Chemical Engineering

University of Washington

Abstract

An assessment of alkali metal-O_2 chemistry: perspectives and prospectives

Honorio Valdés Espinosa de los Monteros

Co-Chairs of the Supervisory Committee:
Associate Professor Stuart B. Adler
Chemical Engineering

Professor Eric M. Stuve
Chemical Engineering

Alkali metal-O_2 batteries (AOB) have emerged as a promising technology for energy storage due to their large discharge capacity compared to technologies such as lithium-ion batteries. In AOBs, the discharge process involves the formation of superoxides or peroxides, while charge involves oxygen evolution from discharge deposits. However, the discharge deposits are electronically insulating, requiring high overpotentials that can cause electrolyte degradation and limit battery cyclability. As a consequence, there has been significant interest in understanding battery chemistry to improve battery performance. Most studies have focused on battery cathodes, however, and the complexity of such systems makes it difficult to gain fundamental understanding of the system. In this work, several experimental frameworks are described to characterize alkali metal-O_2 chemistry.

First, an attempt to use field ionization to describe battery chemistry is described. Field ionization experiments can provide a controlled environment for obtaining fundamental, semi-quantitative information about reactions such as intermediates, relative rates of formation, and location of active reaction sties. Other areas of fundamental research that can provide key information for AOBs and other technologies related to metal-O_2 chemistry are defined. These include solvation characterization, parasitic chemistry studies, side product charge characterization, and

catalyst exploration. In addition, a series of fundamental experiments are proposed to understand phenomena such as the initial stages of discharge and charge, electrolyte solvent reactions with discharge deposits, and spatial distribution of discharge products within discharge deposits. The concept of key states for battery chemistry characterization is described, where a key state is defined as a region where the charge/discharge curve changes behavior such as plateaus or inflection points. Finally, several case studies are presented to show the application of key states to describe battery phenomena such as cell death and transitions between stages of a charge/discharge profile.

TABLE OF CONTENTS

LIST OF FIGURES

LIST OF TABLES

ACKNOWLEDGMENTS

First, I would like to thank my advisers Profs. Stu Adler and Eric Stuve for their patient mentoring and guidance throughout the last 6 years. Also, I would like to thank Profs. Guozhong Cao and Charles T. Campbell for being part of my committee. I would also like to thank my lab mates Tim Geary and TJ McDonald for their patient mentoring when I joined the lab, as well as Kelly Carpenter, Jon Witt, and Brian Gerwe for creating a positive and fun environment in the lab. Also, I would like to thank my GAANN group Brandon Borst, Wilson Chan, and Bihui Lin for providing me the opportunity to being their instructor and competing at the 2014 Environmental Innovation Chalenge. I would like to also thank the ChemE staff Allison, Dave, Joanne, Karen, Dan D, Ao, Noel, Katia, Shoko, Arne, Rex, Kameron, Jesse, and Winston for their help throughout the last 6 years. In addition, I would liek to the thank the graduate students at the department for fostering a friendly and cooperative environment.

In particular, I would like to thank Ali and Megan for their help and support in the most complicated moments of my PhD. Also, thanks to my friends Pablo, Sara, Josh, Ryan Kastilani, Ted, Ian and Kim Braly for their advice and support in finishing grad school. I would also like to thank Fer, Archi, Chava, and Tin for their support throughout the last 6 years and for the fun moments. In addition, I would like to thank the UW Taekwondo Club for providing a friendly and fun environment to destress, particularly Grand Master Sung Lim, Master Woory Lim, and Master Philip Lim for training me and providing me the opportunity to become a black belt. In addition, I would like to thank Svet, Hiro, Nick, Yingying, Stacy, Drew, Brandon, and Gavin for making the training sessions more fun.

I would also like to thank the Everett Branch of the Mountaineers for providing a friendly and supporting environment for learning mountaineering and enjoying the freedom of the hills. In

particular, I would like to thank Jenni and Jon Schwegler, Elaina Jorgensen, and John Fang, as well as Everett Mountain Rescue, Snohomish County SAR, Chelan County SAR, the Canadian Border Patrol, and the 70+ volunteers that participated in my rescue at Sloan Peak in June 18th, 2017. Also, I would like to thank my friends and climbing partners Ryan Stoddard, Bora, Mountainbeering (in particular Evan, Damon, Grant, Josh Noble, Joseph, Cassidy, and Jordan), Alexey, and Momona for the great outdoor experiences.

Also, I would like to thank my parents, siblings, uncles, and cousins for their support throughout my life. Finally, I would like to thanks my friends both in Mexico and the US for their support and friendship.

DEDICATION

To my family and friends

Chapter 1

BACKGROUND

Fossil fuels have been the predominant source of energy for humankind since the 19th century [1]. In 2017, 80% of the energy consumed in the United States was produced from fossil sources [2]. Concerns such as a limited supply, increased CO_2 concentrations, and global warming have led to a push for the development of renewable energies. Energy sources such as wind or solar have become more prominent in recent years. Despite recent developments in renewable energy, several issues such as an intermittent supply and the need for efficient storage methods remain [3]. Current storage methods involve heat storage via molten salts, chemical processes such as thermochemical production of hydrogen, or electrochemical storage [4]. Among these methods, electrochemical storage has attracted interest both as a direct way to store electricity and as an indirect route for storage via fuel synthesis.

1.1 Electrochemical Energy Storage

Electrochemical energy storage involves the storage of electricity through the use of electrochemical cells. Electrochemical cells consist of two electrodes: an anode where an oxidation reaction takes place and a cathode where a reduction reaction takes place. Both electrodes are separated by an ionically conductive electrolyte where the ionic component of the electrolyte is involved in the anode and cathode electrochemical reactions. Meanwhile, electrons flow through an external circuit [5]. Electrochemical cells used for energy storage include batteries and electrolysis cells [3]. In an electrolysis cell, a feedstock is delivered to the cathode side and reduced to produce a fuel with electrical work provided by an external source such as a wind turbine or photovoltaic panel. Commonly, the feedstock is water and is reduced to produce H_2 and O_2. Additional advantages of electrolysis cells include the possibility of synthesis gas production (a mixture of hydrogen and

CO) which can then be used for fuel synthesis via the Fischer-Tropsch process [6], as well as operation as fuel cells. In fuel cell mode, a fuel is oxidized in the anode and the cell produces electrical work [4, 7].

An alternative to electrolysis cells is the use of batteries for direct storage of electrical energy. Currently used battery technologies include lead-acid, Ni-Cd, or Li-ion chemistries [3]. Among these technologies, Li-ion batteries have attracted significant attention due to improved energy and power densities. Since their early development and commercialization in the 1990's, Li-ion batteries have become ubiquitous and their applications range from portable electronics to electric vehicles [8]. Current Li-ion batteries consist of a graphite anode, a lithium intercalation cathode (made of Li-containing ceramics such as $LiCoO_2$), and a liquid electrolyte based on an organic solvent. The reactions occuring at the anode and cathode are shown as Equations (1.1) and (1.2), respectively. Any species in solution have the subscript (sol) and M is a metal such as Mn or Co [8].

$$C_{6(s)} + Li^{+}{}_{(sol)} + e^{-} \longleftrightarrow LiC_{6(s)} \tag{1.1}$$

$$LiMO_{2(s)} \longleftrightarrow \frac{1}{2}Li^{+}{}_{(sol)} + \frac{1}{2}e^{-} + Li_{0.5}MO_{2(s)} \tag{1.2}$$

Despite recent improvements, Li-ion batteries do not provide energy and power densities comparable to liquid fuels for applications such as electric vehicles [9]. As a consequence, further research has focused on developing new battery chemistries such as flow batteries, sodium-beta alumina, or alkali metal-O_2 batteries [10]. In contrast to lithium ion batteries, where charge and discharge occurs via lithium intercalation, the operating principle of an alkali metal-air battery involves the formation and removal of metal oxide deposits on the cathode. In an ideal battery, the discharge product is either an alkali metal superoxide or a peroxide. During charge, oxygen is evolved from the discharge deposits. The observed discharged products are heavily dependent on the nature of the cation, with peroxides dominating in Li-O_2 batteries [11] and superoxides in K-O_2 batteries [12]. NaO_2 and Na_2O_2 have been reported as discharge products in Na-O_2 batteries [13].

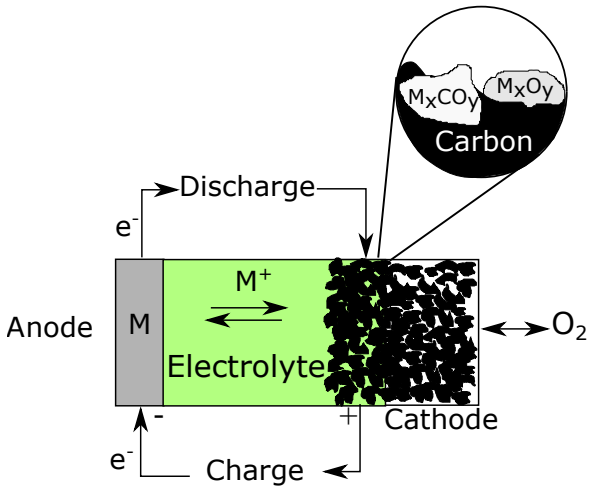

Figure 1.1: Schematic of an alkali metal-O_2 battery. The insets shows discharge products from the desired discharge reactions, such as MO_x, as well as a sample product from side reactions, M_xCO_y.

1.2 Battery architecture and operation overview

Figure 1.1 shows the architecture of an alkali metal-O_2 battery. The typical battery uses a metal-foil anode, a carbon-based cathode, and an electrolyte based on an aprotic solvent. Metal-foil anodes are typically used in order to achieve higher energy densities. However, the anode can exhibit side reactions with the electrolyte, and thus, a solid-electrolyte interface (SEI) is needed to prevent corrosion [14]. Cathodes are prepared by forming carbon slurries and coating them onto a metal grid or foam via film-casting or by ultrasonic treatment [15]. Meanwhile, typical electrolyte formulations use aprotic solvents such as glymes or dimethyl sulfoxide (DMSO) with a Li-based salt such as lithium bis(trifluoromethanesulfonyl)imide (LiTFSI) [14]. Alternative formulations include aqueous [16] or solid-state electrolytes [17]. In addition to single electrolyte architectures, several workers have developed cells with aqueous and aprotic electrolytes separated by a Li-conductive ceramic in order to prevent water reaction with the anode [17].

The nature of the discharge products for each battery chemistry can be determined using the

Discharge product	n	ΔG_f^o (kJ/mol)	U_{rev} (V)
LiO_2	1	-289.66 [18]	3.0 V
Li_2O_2	2	-570.95 [19]	2.96 V
Li_2O	4	-562.10 [19]	2.91 V
NaO_2	1	-218.71 [19]	2.27 V
Na_2O_2	2	-449.63 [19]	2.33 V
KO_2	1	-240.59 [19]	2.49 V

Table 1.1: Reversible potentials for the different discharge products

reversible potential, which is the potential at which the net battery current is zero. The reversible potential,U_{rev} can be determined using Equation 1.3, where ΔG_f^o is the standard Gibbs free energy of formation, n is the number of electrons involved in the reaction, and F is faraday's constant. Table 1.1 shows the reversible potentials for several possible discharge products.

$$U_{rev} = \frac{-\Delta G_f^o}{nF} \tag{1.3}$$

Typically, battery characterization involves galvanostatic cycling, where a battery is charged and discharged at constant current for multiple cycles. An example of battery cycling is shown in Figure 1.2. Plot (a) shows the first 5 charge-discharge cycles of a K-O_2 battery with a Na-K liquid alloy anode. Meanwhile, plot (b) shows the evolution of the charge-discharge profiles throughout 70 cycles. Results show that the batteries have initial charge and discharge overpotentials under 50 mV. As the battery is cycled, the discharge overpotential increases to a value of about 100 mV, while the charge overpotential increases to about 200 mV. In addition, battery capacity initially increases, followed by a decrease as the number of cycles increases. Further analysis showed that this was attributed to electrolyte degradation [20].

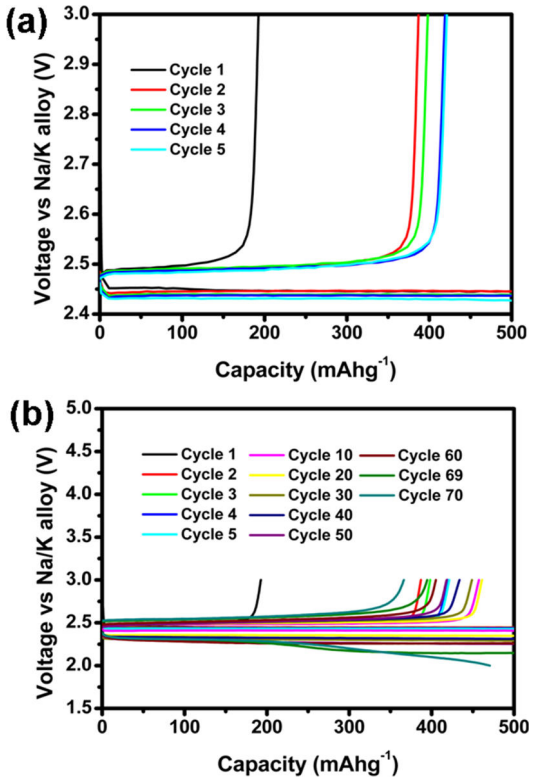

Figure 1.2: Galvanostatic cycling usage for alkali metal-O_2 characterization. The upper inset shows the first 5 charge/discharge cycles of a battery with a Na/K alloy anode, while the lower isnet shows further charge/discharge cycles for the same battery. Reprinted (adapted) with permission from [20]. Copyright (2017) American Chemical Society.

1.2.1 Cathode design

Good cathode designs require a morphology such that discharge products do not clog pores or block the active surface. The most common cathode material is carbon black. Other carbon materials such as graphene or graphene oxide have attracted interest due to high activity towards ORR [21, 22]. In addition to carbon-based cathodes, there has been interest in developing carbon-free cathodes with materials such as indium-tin oxide (ITO) [23], nanoporous gold [24], titanium carbide (TiC) [25] or Co_3O_4 [26]. Such cathodes have advantages such as mitigating electrode degradation [27], reduction of the charging voltage and enhanced electrical contact with the substrate [24, 26]. A comparison between cathode materials and electrode binders is shown in Table 1.2.

1.3 Electrolyte formulations

Most work on alkali metal-O_2 batteries has focused on aprotic organic electrolytes [32]. The use of such solvents provides several advantages such as increased anode stability via the formation of a SEI and the absence of dendrite formation. A good electrolyte solvent has to be stable to avoid degradation at the high potentials during charge, resistant to reaction with oxygen and the cathode, have a high oxygen solubility, and wet the electrode.

1.3.1 Organic electrolytes

Organic solvents are most commonly used in alkali metal-O_2 batteries due to their widespread use in Li-ion batteries. Several organic solvents have been considered such as acetonitrile (ACN), carbonates, ethers, and dimethyl sulfoxide (DMSO) [9, 33]. Carbonates were among the first organic solvents to be used in both Li- and Na-O_2 batteries. However, parasitic reaction products such as Li_2CO_3 or Na_2CO_3 are observed due to poor solvent stability, leading to degradation [33, 34]. As a consequence, most work has focused on the use of more stable solvents such as ethers, dimethyl sulfoxide, or acetonitrile [9, 33].

Ethers such as dimethoxyethane (DME) [35,36], polyethylene glycol dimethyl ether (PEGDME),

Material	Advantages	Disadvantages
Cathode materials		
Carbon black	Ease of manufacturing, high conductivity [28]	Degradation above 3.5 V [28]
ITO	High cyclability [23]	Poor recyclability and recovery from waste [29]
Nanoporous gold	Minimal side reactions, high capacity retention [24]	Reduced specific energy density [24]
TiC	Light weight, minimal side reactions [25]	Lower specific capacity and energy than carbon [25]
Co_3O_4	Improved electrical contact with substrate, controllable morphology, no binder is needed [26]	Multi-step manufacturing [26]
Binders		
Polyvinylidene fluoride (PVDF)	Electrochemically stable, ease of processability [30]	Reacts with lithium [30]
Polytetrafluoroethylene (PTFE)	Electrochemically stable, ease of processability [30], can be used in aqueous suspensions [31]	Reacts with lithium [30]
Cellulose	Environmentally friendly, low cost [31]	Low solubility in water and non-aqueous solvents [31]

Table 1.2: Comparison between cathode materials and binders

or ring ethers such as γ-butyrolactone, tetrahydrofuran, and tetrahydrofuran have been studied for use in Li-, Na-, and K-O_2 batteries [12,13,33]. However, such electrolytes still present degradation issues when used in Li-O_2 batteries [35,36]. Despite these issues, ether solvents such as DME and TEGDME have become the electrolytes of choice due to the large energy barrier for nucleophilic attack by O_2^- [37].

Alternatives to ether and carbonate electrolytes, such as ACN, have also been considered for Li-O_2 batteries. ACN has been widely studied as solvent for the oxygen evolution (OER) and oxygen reduction (ORR) reactions and has shown to be stable towards superoxide parasitic attack [38,39]. However, its use has been limited due to its reactivity towards lithium metal [40] and high volatilty [41]. A solution to this problem is the use of superconcentrated electrolytes, in which lithium salt concentrations higher than 3 M are used [42] and improve the electrolyte's reductive and oxidative stability, but can decrease conductivity [43]. In addition to ACN, dimethyl sulfoxide (DMSO) has been considered as a solvent due to an increased solubility of reaction products. However, DMSO can react with Li_2O_2 [39,44] and sodium metal [37]. Another alternative involves the use of ionic liquids [45]. Ionic liquids have several advantages such as greater electrochemical and chemical stability, no volatility, and tunability of the battery chemistry by variation of the anion-cation pairs [41]. Despite these advantages, ionic liquids suffer from low Li salt solubility and poor Li^+ conductivity [41].

1.3.2 Aqueous electrolytes

In contrast to organic electrolytes, aqueous electrolytes provide benefits such as no flammability and soluble discharge products such as LiOH in alkaline solutions or Li^+ in acidic solutions [9,15]. The charge and discharge reactions for acid and basic electrolytes are shown in Equations 1.4 and 1.5, with their reversible potentials [9,46]. The typical electrolyte is a mixture of LiOH-LiCl in water, with varying concentrations [9]. Other electrolyte formulations include NH_4Cl or nitrate salts [47,48]. For acidic electrolytes, H_2SO_4 can be used in the electrolyte, leading to the formation of Li_2SO_4 [9].

$$2\mathrm{Li}_{(s)} + \frac{1}{2}\mathrm{O}_{2(g)} + \mathrm{H_2O}_{(l)} \rightleftarrows 2\mathrm{LiOH}_{(sol)} \; U_{rev} = 3.35V \tag{1.4}$$

$$2\mathrm{Li}_{(s)} + \frac{1}{2}\mathrm{O}_{2(g)} + 2\mathrm{H}_{(aq)}{}^{+} \rightleftarrows 2\mathrm{Li}_{(aq)}{}^{+} + \mathrm{H_2O}_{(l)} \; U_{rev} = 3.0 - 3.3V, \text{ pH dependent} \tag{1.5}$$

Aqueous electrolytes present several issues. In basic electrolytes, LiOH can precipitate at high concentrations [15]. The precipitates can block pores in the cathode and thus decrease battery performance. A solution to this problem involves the inclusion of a discharge product reservoir, where the discharge product does not form in the cathode and precipitates at the reservoir [16]. In addition to solubility issues, Li is highly reactive with water [9]. Strategies for anode protection include artificial SEIs [49] or two-compartment cells, where the anode is contained in an aprotic electrolyte, the cathode in an aqueous electrolyte, and the separator is Li-conductive [50].

1.3.3 Solid state electrolytes and SEI formation

An alternative to liquid electrolytes is the use of solid state electrolytes. Despite the use of a solid polymer electrolyte on the first reported aprotic Li-air battery [51], the use of solid electrolytes has been limited due to their poor Li^+ conductivity [9]. Compared to aprotic electrolytes, the most significant advantage of solid electrolytes is the absence of parasitic reactions between the electrolyte and the cathode [52]. Some examples of solid electrolytes include $Li_{1+x}Al_xTi_{2-x}(PO_4)_3$ [49] or polymer-based electrolytes [17]. Polymeric electrolytes are prepared by mixing polymer powder, such as poly(ethylene oxide), with Li-containing salts and casting the mixture in a membrane [53]. However, one limitation of poly(ethylene oxide) is oxidation of the membrane at the cathode/electrolyte interface [54].

As described previously, alkali metals are coated by a layer known as the SEI after contact with aprotic solvents. The concept of a SEI was first developed in 1979 and its formation occurs upon contact of the metal with the electrolyte [55]. The SEI consists of insoluble products formed by reactions between the electrolyte and metal and behaves as a solid electrolyte with a thickness of

about 20 nm [56]. Currently, three models have been proposed to explain SEI formation: single stepwise surface reactions leading to a uniform layer, multiple simultaneous reactions leading to a mosaic-like layer, and alignment of decomposition products [56]. Due to the presence of multiple components in the electrolyte, the SEI is complex and includes products such as LiF, lithium esters, Li_2CO_3, Li_2O, LiF, lithium sulfide, and LiOH [56–58].

1.4 Charge-discharge profiles

Charge-discharge profiles for Li-, Na-, and K-O_2 batteries are shown in Figure 1.3. Superoxide discharge products are observed when sodium and potassium are used, while peroxide discharge products are observed when lithium and sodium are used. The reasons for such phenomena will be further discussed in Chapters 2 and 3. The figure categorizes the curves based on the nature of the discharge product: Li_2O_2, NaO_2, Na_2O_2 (hydrated or non-hydrated), and KO_2. Superoxide-based chemistries exhibit constant overpotentials during discharge. Meanwhile, the charge overpotential is constant for most of the charging process, with an exponential increase towards the end of charge. In both sodium and potassium batteries, the charge overpotential is on the order of 100 mV, with K-O_2 batteries having smaller overpotentials than Na-O_2 batteries.

Peroxide-forming batteries exhibit similar behavior as superoxide-forming during discharge. However, the charge profile exhibits plateaus and ramps in overpotential. The presence of such ramps and plateaus can be attributed to different stages of peroxide decomposition [59]. In general, batteries forming peroxide products exhibit larger overpotentials than superoxide forming batteries. For example, the Na_2O_2 profile has an overpotential of about 1 V and that the Li_2O_2 profile has an overpotential of 1.5 V. Another interesting observation is a change in the charge profile of Na_2O_2 products due to discharge product hydration. When hydrated products are present, the charge overpotential is initially small, followed by stepped increases starting around 50% state of charge.

The differences between charge/discharge profiles has caused workers to develop classification systems. One such attempt classifies profiles based on the overpotential dependence as a function of charge and coulombic efficiency for charge [60]. This system does not consider the discharge behavior as all batteries behave in a similar way. Initially, the discharge overpotential is low and

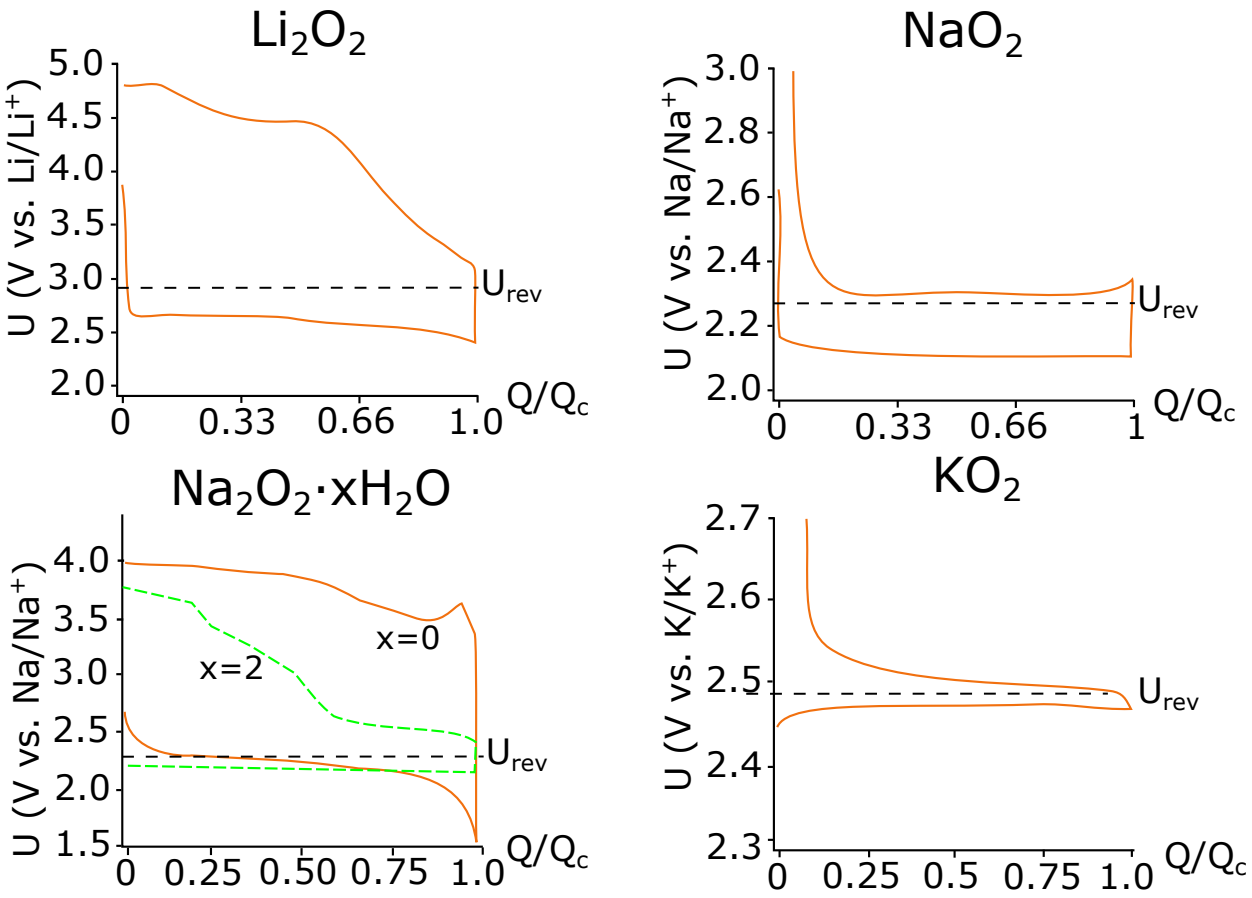

Figure 1.3: Charge-discharge profiles for different alkali metal-O_2 batteries. The $Na_2O_2 \cdot xH_2O$ plots show the anhydrous Na_2O_2 profile as an orange solid line and that of x=2 as a green dashed line. Adapted from references [14], [13], and [12]

stays constant throughout discharge. Towards the end, the discharge voltage decreases rapidly, leading to what is known as cell death. The categories described previously are shown in Figure 1.4 and can be defined as follows [60]:

1. **Type 1A:** This case involves a 100% coulombic efficiency and overpotentials near zero. The charging potential is very close to the reversible potential and increases exponentially once the discharge products are decomponsed

2. **Type 1B:** This case involves a coulombic efficiency under 100% and overpotentials near zero. As in Type 1A, the charging potential is very close to the reversible potential and increases exponentially once all active discharge products are decomposed. Any leftover discharge products might form due to irreversible reactions or have poor connectivity with the cathode.

3. **Type 1C:** This case involves a coulombic efficiency over 100% and overpotentials near zero. As in Type 1A, the charging potential is very close to the reversible potential and increases exponentially once all active discharge products are decomposed. The increased coulombic efficiency can be attributed to the formation of rechargeable products from parasitic reactions with the electrolyte or cathode material.

4. **Type 2:** In these scenarios, the overpotential is greater than zero. This indicates sluggish charge kinetics. which can be caused by multiple reasons that will be described in Chapter 3.

5. **Type 3:** In these cases, the overpotential is a function of the state of discharge. The overpotential can increase linearly, as shown by the solid red lines in Figure 1.4, or in steps, as shown by the dashed red lines in Figure 1.4. The steps can be attributed to the decomposition of multiple discharge products or incomplete discharge [60]

Using the classification system described above, batteries with superoxide discharge products

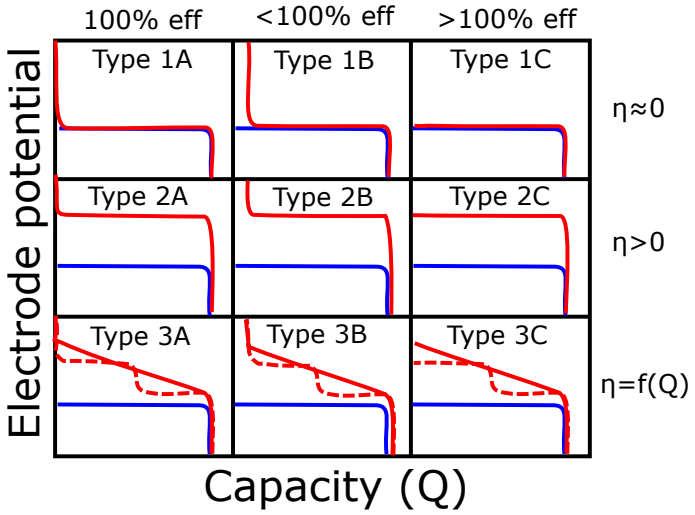

Figure 1.4: Charge-discharge profile categories. The discharge profiles are shown as blue, solid lines, while the charging curves are shown in read as either solid or dashed lines. Adapted from [60].

exhibit type 1B charge profiles. Meanwhile, batteries with peroxide (anhydrous and hydrated) discharge products exhibit either 2C, 3B, or 3C type charge profiles.

1.5 Alkali metal-O_2 battery challenges

Despite their technological promise, Li-air batteries suffer from multiple problems such as high charging overpotentials and poor cyclability. These issues are attributed to the nature of the charging and discharging reactions [61], as well as ohmic losses in the battery [62, 63]. A typical charge/discharge profile for a Li-O_2 battery is shown in Figure 1.5. The initial cycle is labelled as 1 and the third and fifth cycles are labelled as 3 and 5, respectively. The open circuit potential, U_{rev} is 2.9 V, with the charging and discharging potential reaching values of 4.5 V and 2.5 V, respectively for the initial cycle. The battery capacity for each cycle is determined as the maximum charge the battery can hold. For example, the capacity is about 550 mAh/g_c for the initial charge-discharge cycle, decreasing to 400 mAh/g_c for the third cycle, and reaching a value of 200

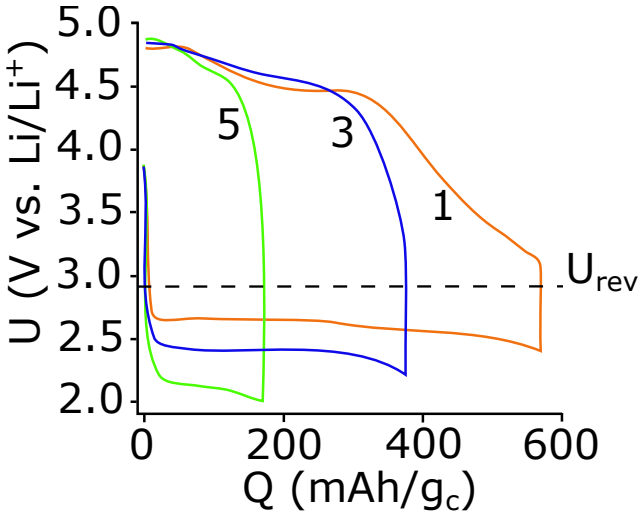

Figure 1.5: Charge-discharge cycle (adapted from McCloskey et al. [61]). The first cycle is shown as an orange curve and subsequent cycles are shown as blue and green curves, respectively

mAh/gc for the fifth cycle. The discharge overpotential shows a similar trend with an initial value of 2.75 V, decreasing to a value of 2.2 V in the final cycle. In addition, the charging overpotential increases from an initial value of 4.5 V in the initial cycle to a value of 5 V in the final cycle. The conductivity limitations and parasitic reactions described in this Section will be further discussed in Chapters 2 and 3.

Chapter 2

DISCHARGE

2.1 Introduction

Alkali metal-O_2 chemistry exhibits complex behavior, as the nature of the discharge product is heavily dependent on the metal cation. In addition, the electrolyte affects what products are observed during discharge. These qualities, coupled with other features such as discharge rate, can be used to explain experimental observations such as deposit morphology and battery capacity. This section describes how these phenomena interplay in alkali metal-O_2 chemistry. In addition, this section describes changes that can occur when contaminants such as CO_2 and H_2O are present.

2.2 Ion solvation and its effects on discharge products

The discharge and charge reaction pathways observed in alkali metal-O_2 batteries are shown in Schemes (2.1) and (2.2), respectively. During discharge, oxygen is reduced at the cathode and M_xO_y (where x,y=1,2) deposits are formed, where M is the metal cation. The first step involves oxygen reduction to superoxide O_2^-. Superoxide is further reduced to peroxide O_2^{2-} either by disproportionation (involving no charge transfer from the cathode) or by superoxide reduction. A further reduction step involving the formation of oxide is also possible [33]. Meanwhile, the charging process involves a single oxidation step where oxygen is evolved directly from the deposit. The nature of the discharge products is highly dependent on the cation used, with Li_2O_2 being the dominant product formed in Li-O_2 batteries, both NaO_2 and Na_2O_2 beign formed in Na-O_2 batteries, and KO_2 being observed in K-O_2 batteries.

Most of the original studies to characterize discharge chemistry and reversibility involved the

$$
\begin{aligned}
O_{2(g)} + M^{+}{}_{(sol)} + e^{-} &\longrightarrow MO_{2(s)} \\
2\,MO_{2(s)} &\longrightarrow M_2O_{2(s)} + O_{2(g)} \\
MO_{2(s)} + M^{+}{}_{(sol)} + e^{-} &\longrightarrow M_2O_{2(s)} \\
M_2O_{2(s)} + 2\,M^{+}{}_{(sol)} + 2\,e^{-} &\longrightarrow 2M_2O_{(s)}
\end{aligned}
\tag{2.1}
$$

$$
\begin{aligned}
MO_{2(s)} &\longrightarrow O_{2(g)} + M^{+}{}_{(sol)} + e^{-} \\
M_2O_{2(s)} &\longrightarrow O_{2(g)} + 2M^{+}{}_{(sol)} + 2e^{-} \\
M_2O_{(s)} &\longrightarrow \frac{1}{2}O_{2(g)} + 2\,M^{+}{}_{(sol)} + 2\,e^{-}
\end{aligned}
\tag{2.2}
$$

use of cyclic voltammetry (CV) [32, 64]. The upper inset of Figure 2.1 shows an application of voltammetry. The lower plot shows CV for oxygen reduction in Li, Na, and K-containing electrolytes. The separation between the reduction (peaks around -1 V) and oxidation (peaks near 1.5 V) peaks in the three scenarios indicates poor reversibility. In addition, the oxidation peak at positive voltages have a plateau-like shape, indicating sluggish kinetics [64]. Meanwhile, the upper left inset shows voltammograms in Li-O_2 taken at different sweep rates. At lower sweep rates, reduction peaks Ep1 and Ep2 are observed. As the sweep rate increases, only one peak is observed. Using this information, Ep1 was attributed to LiO_2 formation, while Ep2 was attributed to electrochemical formation of Li_2O_2 from LiO_2 on the basis that Ep1 occurs closer to the reversible potential. In addition, only one oxidation plateau is observed, indicating that Li_2O_2 is directly oxidized. If the oxidation process occured in 2 distinct electrochemical steps, then 2 oxidation peaks would be expected [64].

The difference in discharge products as a function of solvent can be explained with hard-soft acid-base (HSAB) theory [32, 64]. HSAB theory dictates that strong acids have a high affinity for strong bases, while soft acids have strong affinity for soft bases [65]. For example, Li^+ and K^+ are Lewis acids (electron pair acceptors), with Li^+ being the harder acid due to its smaller size (Li^+ has an ionic radius of 90 pm, while K^+ has a radius of 152 pm). Meanwhile, O^{2-} and

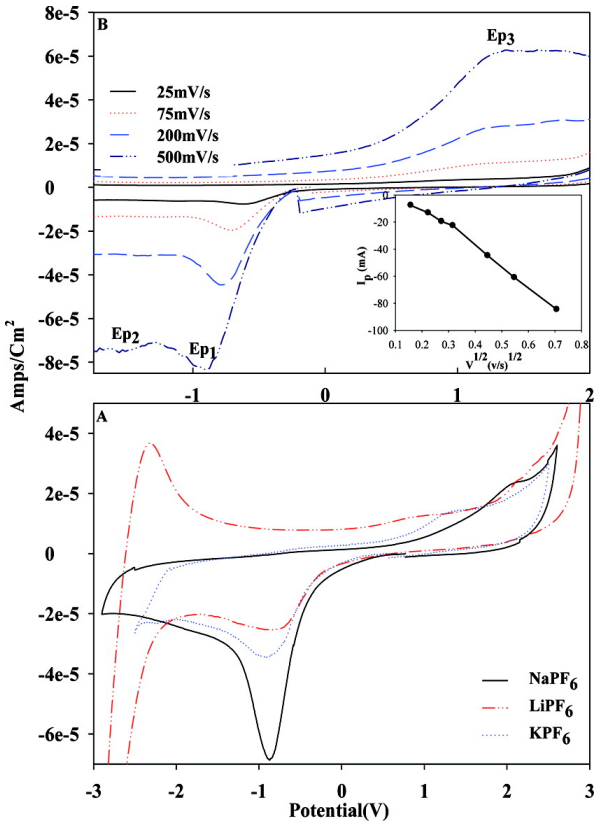

Figure 2.1: Cyclic voltammetry use for alkali metal-O_2 characterization. The upper inset shows an application of voltammetry, while the lower inset shows cyclic voltammograms for oxygen reduction in Li (red), Na (black), and K (blue) containing electrolytes. Reprinted (adapted) with permission from [64]. Copyright (2009) American Chemical Society.

O_2^{2-} are harder bases than O_2^{-}. As a consequence, a softer acid (such as K^+) will react with a softer base (such as O_2^{-}) and the predominant discharge product in an electrolyte containing K^+ will be KO_2. This process is shown in Figure 2.2. Initially, a solvated cation is formed by metal oxidation of the anode, followed by solvation. The solvated cation then forms an adduct with superoxide formed in the cathode. The stability of this adduct is dependent on the solvent, with harder basic solvents forming more stable adducts. When a soft basic solvent is used, O_2^{-} readily undergoes disporportionation or reduction to form O_2^{2-}. In turn, this leads to the formation of M_2O_2. Meanwhile, when a hard solvent is used, MO_2 is formed [65].

The basicity of solvents can be assessed using the donor number (DN), with harder bases having larger DN. The DN is defined as the negative enthalpy of formation (in kcal/mol) of an acid-base adduct [66]. For example, DMSO is a stronger base than DME and ACN, with DMSO having a DN of 29.8 while DME and ACN have values of 20 and 14.1, respectively [65]. Solvents with harder basicity will have bigger affinity to strong acids and will form stable solvation clusters of about 4 solvent molecules, as shown in inset b) of Figure 2.2 [32]. This will soften the acidity of Li^+ due to enhanced charge screening, allowing it to react with O_2^{-}. In weakly basic solvents, O_2^{-} reduction to either O_2^{2-} or O^{2-} is favored. These observations can explain why Li_2O_2 and KO_2 are the dominant product in Li^+ and K^+ containing electrolytes [32], as well as the observation of both NaO_2 and Na_2O_2 in Na^+ containing electrolytes. Similar to Li^+, the ability of a solvent to solvate O_2^{-} is dependant on the acidity of the solvent, which can be described using the acceptor number (AN) [66]. The acceptor numbers of DMSO, DME, and ACN are 19.3, 10, and 18.9, respectively [66, 67]. This implies that DMSO and acetonitrile are stronger acids that DME. Table 2.1 shows the properties of several solvents of choice for alkali metal-air batteries.

The nature of the solvation structure is dependent on factors such as the nature of the solvent, electrolyte concentration, and the degree of salt dissociation [75]. Based on how the cation interacts with the solvent and anion, three different types of solvation structures can be defined: solvent-separated ion pairs (SSIP), contact ion pairs (CIP), and aggregates (AGG). In SSIPs, the cation is solvated by solvent molecules only and segregated from the anion, which is not solvated. In the CIP and AGG structures, the anion is coordinated to one or more cations and anions are coordinated

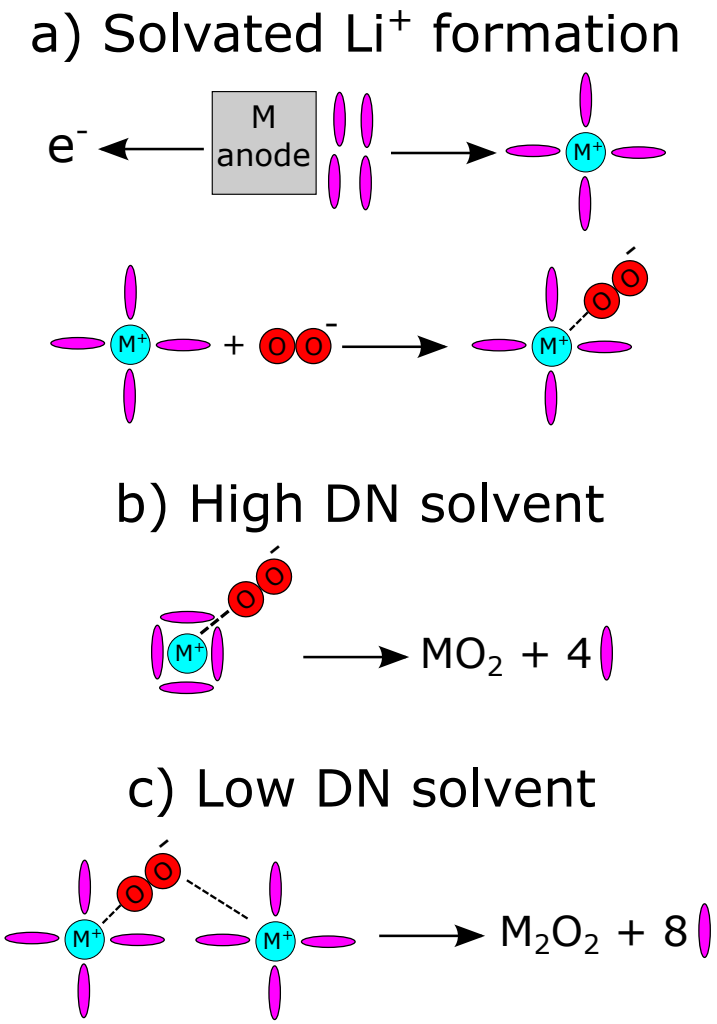

Figure 2.2: HSAB theory in Li-Air battery chemistry. Inset a) shows the formation of a solvated cation upon via metal oxidation at the anode, with the solvent being represented by purple ovals. The solvated cation can then form an adduct with a superoxide anion, which originates at the cathode. The reaction pathways for high and low DN solvents is shown in insets b) and c), respectively.

Solvent	DN (kcal/mol)	AN	ε (25°C)	Discharge products
ACN	14.1	18.9	36.64	Li_2O_2 [38]
DME	20.0	10.2	7.2	Li_2O_2 [68], NaO_2 [69], Na_2O_2 [70], KO_2 [12]
DMSO	29.8	19.3	48.0	Li_2O_2 [24]
TEGDME	16.6	11.7	7.79	Li_2O_2 [71], NaO_2 [72], Na_2O_2 [73]

Table 2.1: Commonly used organic electrolyte solvent properties. DN refers to the donor number, AN refers to the acceptor number, and ε is the dielectric constant. Adapted from [74] and [32]

to one anion in CIP and 2 or more anions in AGG structures, respectively [76]. A depiction of such structures is shown in Figure 2.3. SSIP structures are the dominant structure at lower concentrations, while CIP and AGG dominate at higher concentrations.

The nature of the cation solvation can be further affected by the presence of contaminants such as H_2O [78]. In low DN solvents, cations such as Li^+ have solvation shells made exclusively of water. Meanwhile, in high DN solvents, such as DMSO, Li^+ will be solvated by both water and the solvent [79]. H_2O solvation by the electrolyte solvent also plays a role in the kinetics of the O_2^- disproportionation , with decreased kinetics in solvents with stronger H_2O solvation such as DMSO [80].

2.3 Deposit morphology

Since most battery designs involve the use of porous cathodes, aggregation of M_xO_y species can clog pores and affect battery performance. Previous experimental work has shown that superoxide and peroxide products have different discharge product morphologies depending on factors such as the dishcarge rate and electrolyte solvent [81]. This section describes the general morphology of the discharge products.

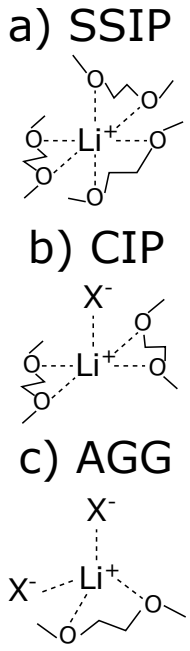

Figure 2.3: Solvation structures for DME. Inset a) shows a solvent-separated ion pair (SSIP), inset b) shows a contact ion pair (CIP), and inset c) shows an aggregate (AGG). Adapted from [77].

In addition to affecting the nature of the discharge product, where peroxides are formed when harder cations are used in the electrolyte, solvents can also affect the morphology. A general mechanism for deposit formation is shown in Figure 2.4. Discharge starts when solvated M^+ reacts with superoxide to form MO_2 on the surface of the cathode. In low DN solvents with hard cations, the following step involves the formation of M_2O_2 by either disproportionation or further reduction. This mechanism is referred to as the surface mechanism in Figure 2.4 and it leads to deposits forming thin films coating the cathode [67]. Meanwhile, when high DN solvents (such as DMSO) or weaker cations (such as Na^+ and K^+) are used, MO_2 can be dissoved to yield solvated $O_2{}^-$ and M^+. After solvation, MO_2 can precipitate on M_2O_2 deposits, where MO_2 undergoes disproportionation to M_2O_2. This mechanism involving $O_2{}^-$ is referred as the solution mechanism in Figure 2.4. The presence of three dimensional discharge deposits has been described using the solution mechanism [13, 67]. Solution mediated discharge can also be observed in low DN solvents, such as DME, when the electrolyte salt contains high DN anions such as $NO_3{}^-$ and Br^- [82]. In addition to solvation, temperature also affects morphology with larger deposits (with constant aspect ratio) being observed at higher temperature, as well as leading to an increased number of particles due to the presence of more nucleation sites [83].

Morphology can be characterized using techniques such as scanning electron mciroscopy (SEM) or transmission electron microscopy (TEM) [84]. Characterization with these techniques is typically done after cell cycling, limiting understanding of morphological evolution during charge and discharge [59]. In recent years, *in operando* techniques have been developed to characterize such processes [85]. In contrast to conventional characterization techniques where button cells can be used, special cell designs are needed for *in operando* techniques [86]. One such example is X-ray tomography [87]. In tomography experiments, the *in operando* cell is rotated and a series of 2D x-ray images are used to reconstruct a 3D image. X-ray tomography can be performed with both conventional and synchrotron x-ray sources. However, synchrotron x-rays allow for better temporal and spacial resolution [88]. The lower inset of Figure 2.5 shows the size distribution of NaO_2 deposits on a Na-O_2 battery. The results show that NaO_2 deposit growth exhibits a spatial gradient across the electrode, with larger particles growing in regions of the electrode closer to the

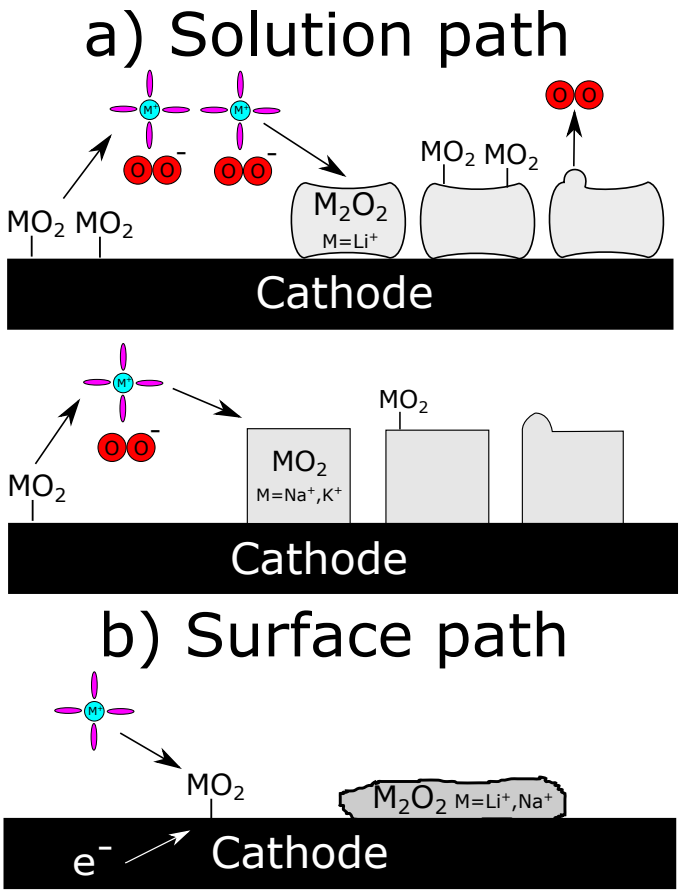

Figure 2.4: Discharge via surface and solution pathways. Inset a) shows discharge via the solution pathway for peroxides and superoxides, while inset b) shows discharge via the surface pathway for peroxides. The solvent is shown as purple ovals, M^+ as a blue circle, and O_2 and its reduction products as two connected red circles.

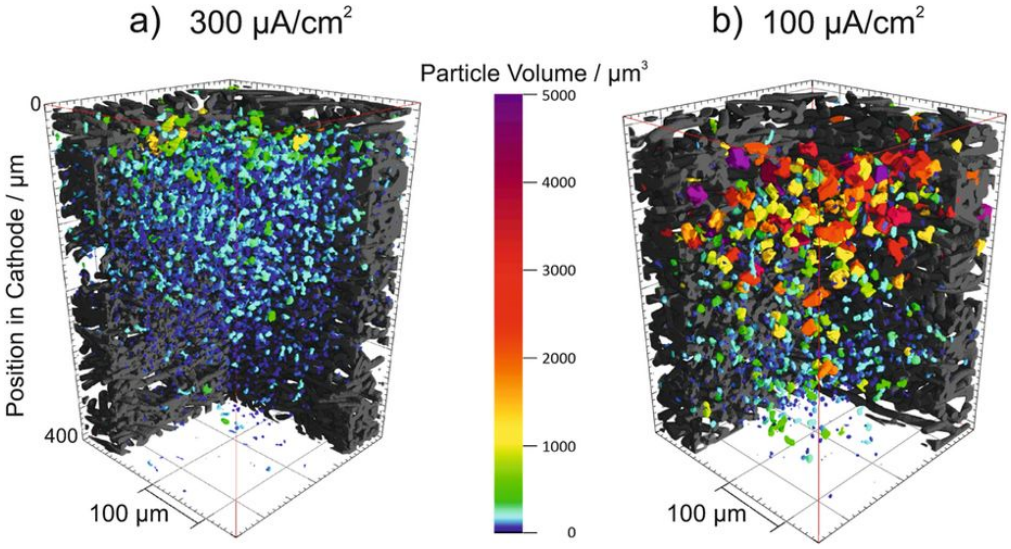

Figure 2.5: X-ray tomography experimental data. The lower portion shows NaO_2 particle size distribution in a cathode as a function of position [89].

gas-electrolyte interface. Generally, larger cubic deposits were formed at lower current densities, with a transition to octahedral and pyramidal morphologies at high current densities [89].

2.3.1 Peroxide-based products

Li_2O_2 deposits can exhibit a toroidal shape when Li^+ and O_2^- are strongly solvated [67]. This occurs when high DN solvents or anions or anions are used [82]. However, when Li^+ and O_2^- are weakly solvated, the discharge products coat the cathode until discharge stops. This observation has been attributed to the solution-mediated mechanism described previously in high DN solvents, while discharge is dominated by reduction in the surface of the cathode in low DN solvents [67]. Meanwhile, Na_2O_2 deposits typically exhibit amorphous morphologies, with grains forming at low current densities and films at high current densities [90].

The observed morphology in Li_2O_2 deposits depends on both the state of charge and discharge rate [81,91]. The deposits exhibit a spherical shape at low state of discharge and evolve to a toroidal

shape at higher states of discharge [81, 83, 91, 92]. Figure 2.6 shows a depiction of the toroid formation mechanism. At the beginning of discharge, Li_2O_2 platelets form on the cathode. As the depth of discharge increases, nucleation can occur between platelets, leading to the formation of toroid-like deposits [91]. Further discharge can lead to the formation of a defect-rich, superoxide-like shape in the edges of the toroid [93]. At low discharge current densities, nucleation initially occurs in the cathode and the rate of LiO_2 solvation is favored over further reduction to Li_2O_2, leading to the formation of toroid-like deposits [94]. An increase in the discharge rate leads to an increase in the toroid aspect ratio (height/diameter) [94, 95]. For very large discharge rates and state of charges, the deposits become amorphous aggregates, as Li_2O_2 nucleation occurs faster than LiO_2 solvation [94].

Superoxide detection in Li-O_2 batteries has been possible thanks to Raman spectrocopy. Raman spectroscopy is a technique that uses the inelastic scattering of monochromatic light to detect molecular vibrations in polarizable species [96]. In this technique, a laser is shined at a sample, leading to excitation of molecules. After excitation, the molecule relaxes and emits photons. In Raman spectroscopy, photons with energies higher (Stokes shift) or lower (anti-Stokes shift) than the laser energy are detected. Since Stokes shifts are more intense, they are typically detected in Raman spectroscopy [97]. The applicability of Raman is limited to the detection of polarized species. For example, O_2^- will have a strong Raman signal due to its strong dipole, while O_2^{2-} will have a negligible signal [96]. One advantage of Raman spectroscopy is that it can be used as an *in operando* technique with aprotic solvents since it does not require vacuum [98]. In this case, signals can be very weak and therefore, surface enhanced Raman spectroscopy (SERS) is typically used [96]. SERS uses an effect where certain substrates can selectively enhance Raman scattering for materials in close proximity. Such substrates include gold, silver, and copper [97]. Figure 2.7 shows the use of SERS for superoxide detection in different electrolytes as a function of time under different applied potentials. Spectra show the presence of Li_2O_2 (800 cm^{-1}), LiO_2 (1140 cm^{-1}), and O_2^- (1100 cm^{-1}). The results show that no LiO_2 is detected in high DN electrolytes, indicating the presence of solution-mediated discharge. This is further supported by the presence of O_2^- peaks at lower overpotentials. Meanwhile, in low DN solvents, LiO_2 peaks are observed. The

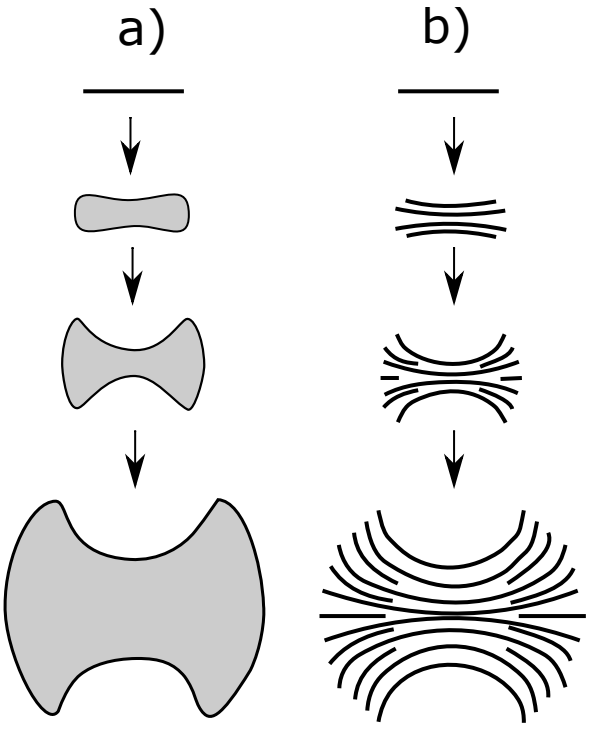

Figure 2.6: Li-air battery deposit growth. The left side shows the morphological evolution of a toroid. The right side shows how Li_2O_2 platelets stack, leading to the formation of toroids. Adapted from [91].

lifetime of LiO_2 will depend on the DN of the solvent, with lower DN solvents having a smaller LiO_2 lifetime [99].

2.3.2 Superoxide-based products

Superoxide discharge products typically form three-dimensional shapes, with cubes being formed in Na^+ and K^+-based chemistries [12, 100]. In contrast, Na_2O_2 deposits are typically amorphous. The presence of both NaO_2 and Na_2O_2 can be attributed to thermodynamic and kinetic stability. A graphical depiction of these phenomena is shown in Figure 2.8. Na_2O_2 is the stable product at standard temperature and pressure, while NaO_2 is the dominant product at oxygen rich conditions and low temperatures. The observed NaO_2 cubes in multiple battery studies has been attributed to the kinetic stability of the (100) facet of NaO_2 and its very slow disproportionation to Na_2O_2. Meanwhile, Na_2O_2 formation in some scenarios can be explained by oxygen diffusion limitations [101]. Similar to what has been observed in superoxides, an increase in the discharge current reduces cube size due to increased nucleation rate, as well as causing deposition of MO_2 as thin films [102]. In addition, O_2 partial pressure can also have an effect on deposit size and morphology. At low P_{O2}, cubic crystals are observed. Meanwhile, at higher P_{O2}, thick films covering the cathode. These observations can be attributed to enanced O_2 availability on the electrolyte at higher pressures [103].

Morphological effects due to operation pressure can be proved indirectly using electrochemical techniques such as Electrochemical Impedance Spectroscopy (EIS) [102]. An example of EIS data is shown in Fig 2.9. The right inset shows an application of EIS for characterization of Na-O_2 batteries. The figure shows the evolution of the ionic and charge transfer resistances, as well as the cathode capacitance as a function of state of discharge at a single operating pressure. The plotted parameters were obtained by fitting experimental EIS results to an equivalent circuit model. For more information about equivalent circuit models, refer to reference [104]. The ionic resistance within the pores (shown in red) remains essentially constant throughout the charging process. Meanwhile, the cathode/electrolyte charge transfer resistance (shown in blue) increases throughout the discharge process, showing a sharper increasing trend at low discharge current density. This increase can be attributed to the formation of insulating NaO_2 discharge products.

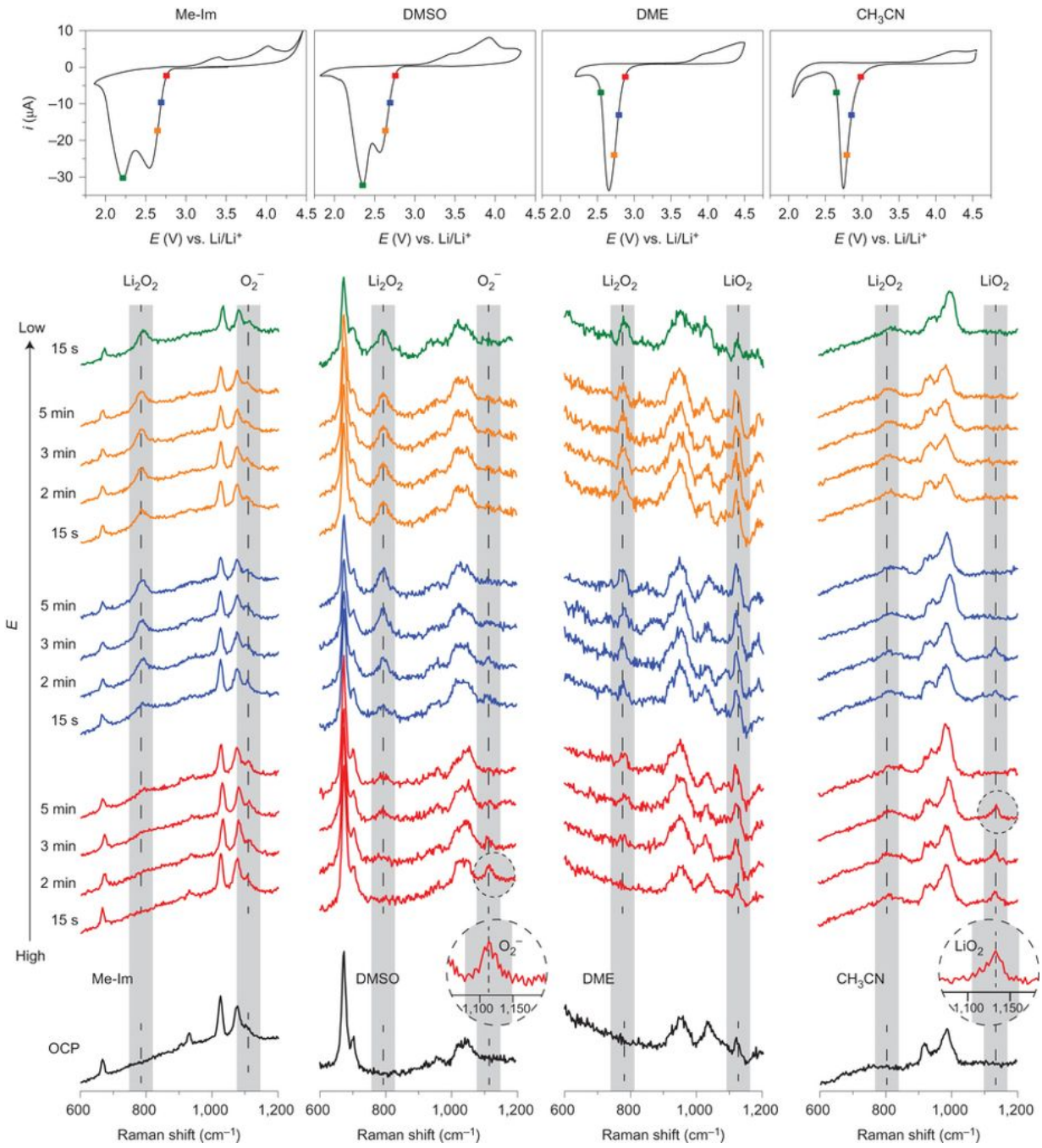

Figure 2.7: SERS spectra for different electrolytes as a function of applied potential [99]. Taken with permission of the Nature Publishing Group.

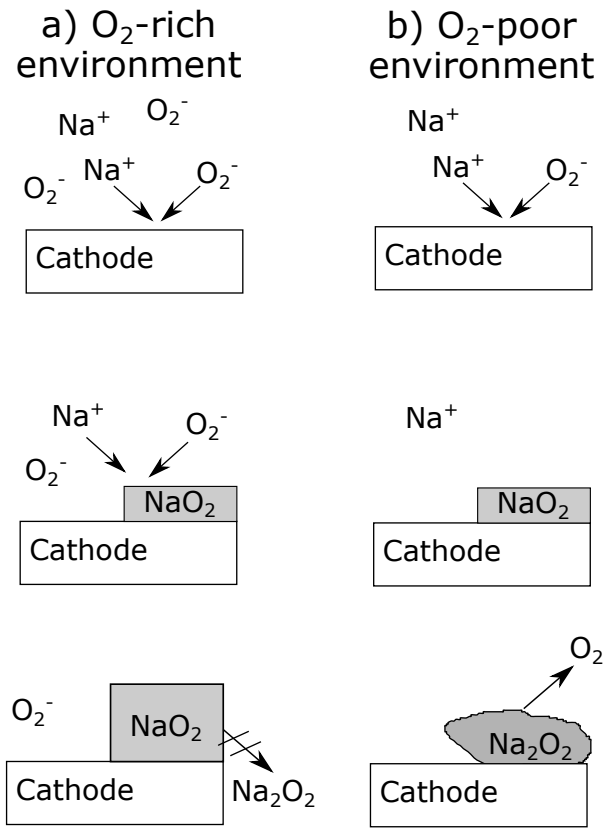

Figure 2.8: Conditions affecting Na-O_2 battery discharge products. Inset a) shows the behavior at high P_{O2}, while inset b) shows the behavior at low P_{O2}.

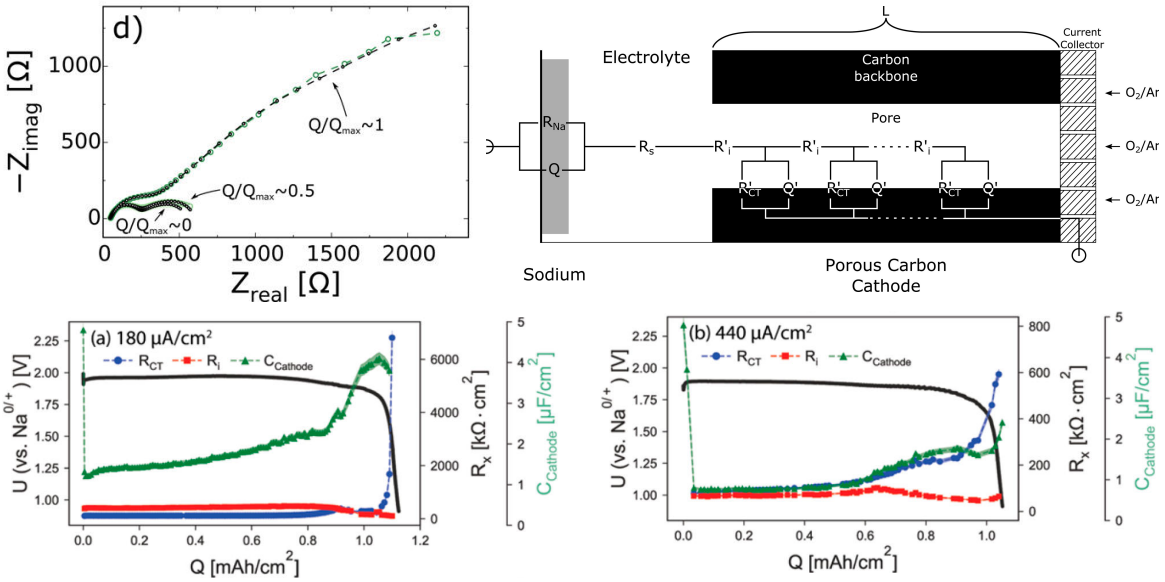

Figure 2.9: Example of EIS use for alkali metal-O_2 characterization. The upper left corner shows experimental EIS data, the upper right corner shows the equivalent circuit used to fit the data, while the bottom left and right corners show the obtained fit parameters as a function of battery capacity. Reprinted (adapted) with permission from [103] and [105]. Copyright (2016) and (2018) American Chemical Society.

This is supported by the initial decrease in capacitance (shown in green). However, the authors not discuss the reasons for the further increase in capacitance as a function of state of discharge [103].

2.4 CO_2 reactions

A signifcant challenge to the deployment of Li-air batteries is the presence of parasitic reactions with CO_2, leading to the formation of Li_2CO_3. Also, batteries operating with O_2:CO_2 mixtures between 30 and 70 % O_2 exhibit higher capacities compared to batteries using O_2 only [106, 107]. This increase in capacity has been attributed to changes in deposit morphology [106]. An additional challenge when switching from O_2 to air involves changes in the discharge reaction pathways.

Previous work has shown that O_2^- can react with CO_2 to form CO_4^- [108], which can further be reduced to $C_2O_6^{2-}$ by CO_2 and O_2^- incorporation [109]. In the presence of an alkali metal cation, this reaction pathway can lead to the formation of solid intermediates such as $LiCO_4$ [110]. This reactions are shown in Equation (2.3).

$$\begin{aligned} O_{2(g)} + CO_{2(g)} + e^- &\longrightarrow {CO_4}^-{}_{(sol)} \\ {CO_4}^-{}_{(sol)} + {Li^+}_{(sol)} &\longrightarrow LiCO_{4(sol)} \\ {CO_4}^-{}_{(sol)} + e^- + CO_{2(g)} &\longrightarrow {C_2O_6}^{2-}{}_{(sol)} \end{aligned} \tag{2.3}$$

The nature of the electrolyte solvent seems to have an effect on the extent of Li_2CO_3 formation, with Li_2CO_3 formation being minimized in solvents with low dielectric constant, such as DME, due to weaker solvation and favored Li_2O_2 [110]. Meanwhile, Li_2CO_3 is formed in high dielectric constant solvents, such as DMSO [110] In the case of strong solvation, O_2^- preferentially reacts with CO_2 to form CO_4^- [108]. Several reaction pathways for the formation of Li_2CO_3 have been proposed involving the formation of intermediates such as $LiCO_4$, $C_2O_6^{2-}$, or reactions between CO_2 and either LiO_2 and Li_2O_2 [110, 111]. A diagram of these pathways is shown in Figure 2.10. M_2CO_3 (M=Li, Na, K) formation is not limited to the cathode and can also occur in the anode via direct reaction between the metal and CO_2 [112].

The presence and distribution of Li_2CO_3 can be detected with techniques such as transmission x-ray microscopy (TXM). One advantage of TXM is the possibility of obtaining both spatial and composition distributions [113]. Similar to SEM and TEM, TXM characterization requires removal of the sample prior to characterization. The upper inset of Figure 2.5 shows the spatial distribution of Li_2CO_3, Li_2O_2, and LiO_2 on discharge deposits of a Li-O_2 battery. These results show that the deposits have a surface layer of Li_2CO_3 of constant thickness with a Li_2O_2 core. In addition, Li_2O_2 toroids can have varying composition of LiO_2. Besides toroids, some Li_2CO_3 deposits were

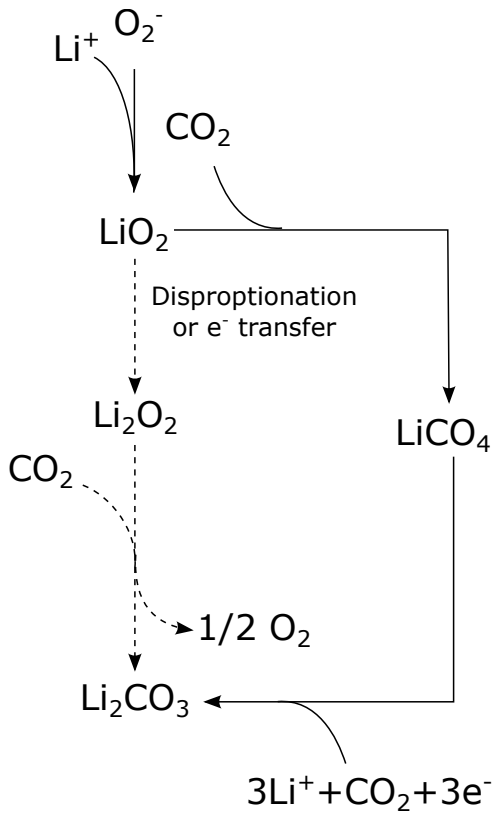

Figure 2.10: Proposed pathways for Li_2CO_3 formation (adapted from Lim *et al.*)

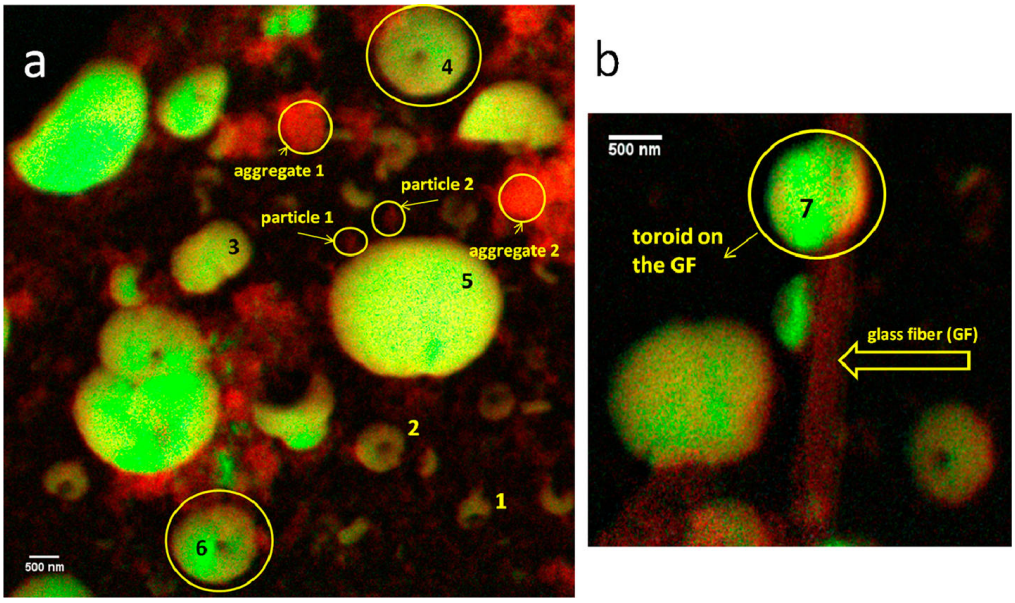

Figure 2.11: TXM experimental data. Inset a) shows TXM data from a Li-O_2 cathode. Li_2CO_3 is shown in red, Li_2O_2 is shown in green, and LiO_2 in cyan. Inset b) shows a discharge deposit formed on a glass fiber separator used to separate the anode from the cathode [113]. Reprinted (adapted) with permission from [113]. Copyright (2014) American Chemical Society.

detected. Based on these observations, the authors proposed a growth mechanism where Li_xO_2 deposits grow underneath a Li_2CO_3 shell [113].

2.5 H_2O reactions

The presence of H_2O leads to complex behavior depending on its concentration [114]. Such behavior can be observed as changes in deposit morphology and parasitic reactions. The presence of H_2O in low DN solvents causes the formation of toroid [67] or nest-shaped [115] deposits and enhanced capacity [114]. These experimental observations have been attributed to improved solvation of LiO_2 during discharge, leading to the presence of solution-mediated discharge. In this case, H_2O aids both Li^+ and O_2^- solvation due to its high DN and AN [67]. Interestingly, some studies

have also shown that water is consumed during the charge process [115], as will be described later. This water consumption has been shown to also aid in charge to some degree [46]. The enhancing effects of H_2O are heavily dependent on concentration, with discharge capacity increasing monotonically as H_2O content increases, reaching a saturation point where further increments in H_2O content do not lead to increased discharge capacity [115]. However, H_2O is detrimental to the cyclability of Li-O_2 batteries due to anode corrosion [116, 117].

The effect of water on oxygen reduction in aprotic solvents has been widely studied in aprotic solvents including DMSO and acetonitrile [80, 118–121]. A series of reactions thought to occur when H_2O is present are shown in Equation 2.4. Water has been shown to induce superoxide disproportionation to form $HO_2^{\cdot}$ and OH^- [119]. This can be followed by an additional O_2^{-} disproportionation step, yielding HO_2^- and O_2. In addition, $HO_2^{\cdot}$ can disproportionate to form H_2O_2 and O_2. H_2O_2 can further react to produce $OH^{\cdot}$, an extremely reactive radical that might induce electrolyte degradation [115]. The nature of the reaction pathway for water-induced O_2^- disproportionation is pH dependent. In acidic solutions, Reaction 2.9 can also take place. H_2O solvation by the electrolyte solvent also plays a role in the kinetics of the O_2^- disproportionation reactions described previously, with decreased disproportionation kinetics in solvents with stronger H_2O solvation such as DMSO. Such interactions can block H_2O from interacting with peroxides, thus reducing the availability of H_2O protons [80].

$$O_2^{\cdot -}{}_{(sol)} + H_2O_{(sol)} \rightleftharpoons HO_2^{\cdot}{}_{(sol)} + OH^-{}_{(sol)} \tag{2.4}$$

$$O_2^{\cdot -}{}_{(sol)} + HO_2^{\cdot}{}_{(sol)} \longrightarrow O_{2(g)} + HO_2^-{}_{(sol)} \tag{2.5}$$

$$2\,O_2^{\cdot -}{}_{(sol)} + H_2O_{(sol)} \rightleftharpoons HO_2^-{}_{(sol)} + OH^-{}_{(sol)} + O_{2(g)} \tag{2.6}$$

$$2\,HO_2{}^{\cdot}{}_{(sol)} \longrightarrow O_{2\,(g)} + H_2O_{2\,(sol)} \tag{2.7}$$

$$O_2{}^{\cdot-}{}_{(sol)} + H_2O_{2\,(sol)} \longrightarrow HO^{\cdot}{}_{(sol)} + OH^{-}{}_{(sol)} + O_{2\,(g)} \tag{2.8}$$

$$O_2{}^{\cdot-}{}_{(sol)} + e^{-} + H^{+}{}_{(sol)} \rightleftharpoons HO_2{}^{\cdot}{}_{(sol)} \tag{2.9}$$

Most work aimed at understanding the effect of H_2O in alkali metal-O_2 batteries has focused on Li. In contrast to what is observed with CO_2 side chemistry, H_2O can induce side reactions with the anode [117] and Li_2O_2, as well as potentially aiding charge via proton attack of Li_2O_2 [115]. Such studies have shown that the presence of water in the electrolyte leads to the formation of products such as LiOH, LiOOH, H_2O_2, and H^+ [67, 80, 115, 120–123]. A series of all the possible reactions involved are shown in Equation 2.10-2.13. The presence of H^+ by either addition of acid or water electrolysis can aid in the charging process by reacting with Li_2O_2 to produce H_2O_2 and Li^+ [46]. Further studies have shown that water can also behave as a catalyst when adsorbed in surfaces. In such a case, water can form $LiO_2\cdots H_2O$ complexes that can facilitate proton transfer. The proposed reaction sequence for this phenomenon is shown in Reaction 2.13, where hydrogen bonds are shown as $\cdots$ [124].

$$Li_2O_{2(s)} + H_2O_{(sol)} \rightleftharpoons LiOOH_{(s)} + LiOH_{(s)} \tag{2.10}$$

$$2\,H_2O_{(sol)} + Li_2O_{2(s)} \rightleftharpoons 2\,LiOH_{(s)} + H_2O_{2(sol)} \tag{2.11}$$

$$O_2{}^{\cdot-}{}_{(sol)} + e^{-} + H_2O_{(sol)} \rightleftharpoons HO_2{}^{-}{}_{(sol)} + OH^{-}{}_{(sol)} \tag{2.12}$$

$$\begin{aligned} \mathrm{LiO_{2ad}\cdots H_2O + O_2 + e^- \longrightarrow LiO_2\cdots OH_2\cdots {O_2}^-{}_{ad}} \\ \mathrm{LiO_2\cdots OH_2\cdots {O_2}^-{}_{ad} + e^- \longrightarrow LiO_2\cdots O^-H_2\cdots {O_2}^-{}_{ad}} \\ \mathrm{LiO_2\cdots O^-H_2\cdots O_2-_{ad} + 2Li^+ \longrightarrow Li_2O_2 + LiO_{2ad}\cdots H_2O} \end{aligned} \tag{2.13}$$

2.6 Electrolyte reactions

A major challenge towards the commercial development of alkali metal-air batteries is the presence of electrolyte degradation due to superoxide species that might react with the solvent. Poor superoxide stability has been observed in most typical alkali metal-O_2 battery solvents to some extent. For example, solvents such as carbonates exhibit significant degradation, while glymes or DMSO exhibit a decreased extent of degradation. Due to the strong basicity of superoxide, good electrolyte solvents must have a low pKa in order to avoid parasitic reactions with superoxide [41]. In addition to solvent reactions, several studies have detected the presence of anion reactions. Anions such as ${PF_6}^-$ and TFSI degrade forming products such as LiF [125, 126].

Most reactions involving solvent degradation are initiated via superoxide attack of alkyl carbon sites [127–131], leading to proton or hydrogen abstraction from the solvent molecule. Some classes of electrolytes, such as lactones and nitriles, can exhibit reactions involving ketone, nitrile, or amide groups [41, 127]. Typically observed degradation products in carbonate and ether solvents include Li_2CO_3, formates ($CH_3-COO-X$), and acetates ($CH_3-CH_2-COO-X$), among others [35, 37, 112, 132, 133]. An alternative to prevent superoxide attack involves the usage of ionic liquids. However, care must be taken as some cation and anion combinations are susceptible to nucleophilic attack [134, 135]. An alternative for superoxide attack mitigation consists in partial fluorination of the solvent molecule [127, 136]. Another advantage of electrolyte fluorination include fast oxygen dissolution kinetics. However, such solvents have poor lithium salt solubility [137].

Degradation products can be detected with techniques such as nuclear magnetic resonance (NMR) spectroscopy. In NMR, a strong magnetic field (fields between 2 and 20 T are used) with bursts of radiofrequency radiation is used to induce transitions between energy levels in the

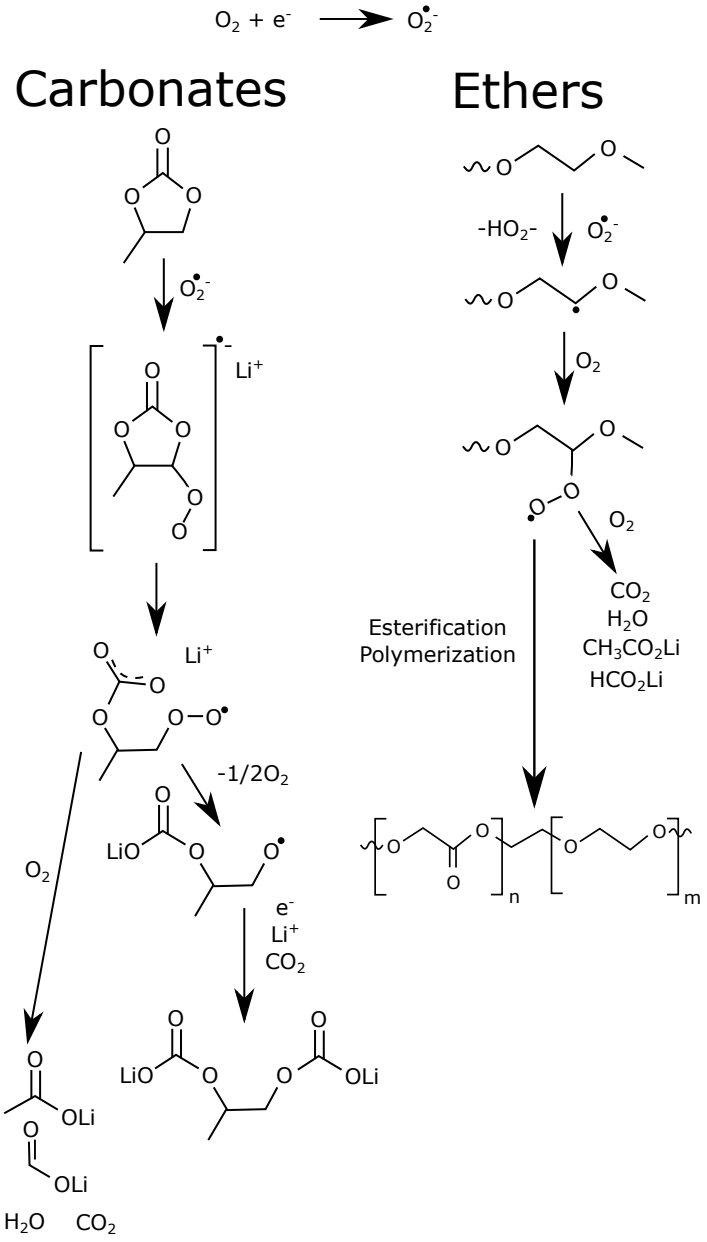

Figure 2.12: Solvent degradation reactions. The pathway on the left side of the figure shows the mechanism for carbonate degradation, while the pathway on the right shows the pathway for ether degradation.

nucleus. The transitions can only occur at a particular resonance frequency. The resonance frequency will depend on factors such as the chemical environment (how atoms are bonded to each other) [138]. The field frequency is determined based on the element of interest, typically ^{1}H and ^{13}C [132]. Nuclear magnetic resonance is particularly useful as a method to determine the molecular structure of electrolyte degradation products that form [125, 132], as well as detecting the presence of solid products such as LiOH via solid state NMR (ssNMR) [139] and for characterization of solvation strength [78, 79]. An example of degradation product characterization in an ether electrolyte using NMR is shown in Figure 2.13. Inset a) shows ^{1}H NMR spectra indicating the presence of formate (peak 8 ppm) as a degradation product and ether groups (peaks between 3 and 4 ppm). Salt stability can be characterized using ^{19}F, ^{11}B, and ^{35}Cl NMR. Insets b) and c) show ^{19}F NMR spectra of discharge products for different anions. In all cases, LiF is the main degradation product. Inset d) shows ^{11}B NMR spectra for several anions. Such spectra show peak broadening and shifts compared to the pure salts, indicating that decomposition occurs. Finally, inset e) shows ^{35}Cl NMR spectra for $LiClO_4$ electrolytes. Such spectra only show a peak for ClO_4^-, indicating that this anion is stable in Li-O_2 batteries [125].

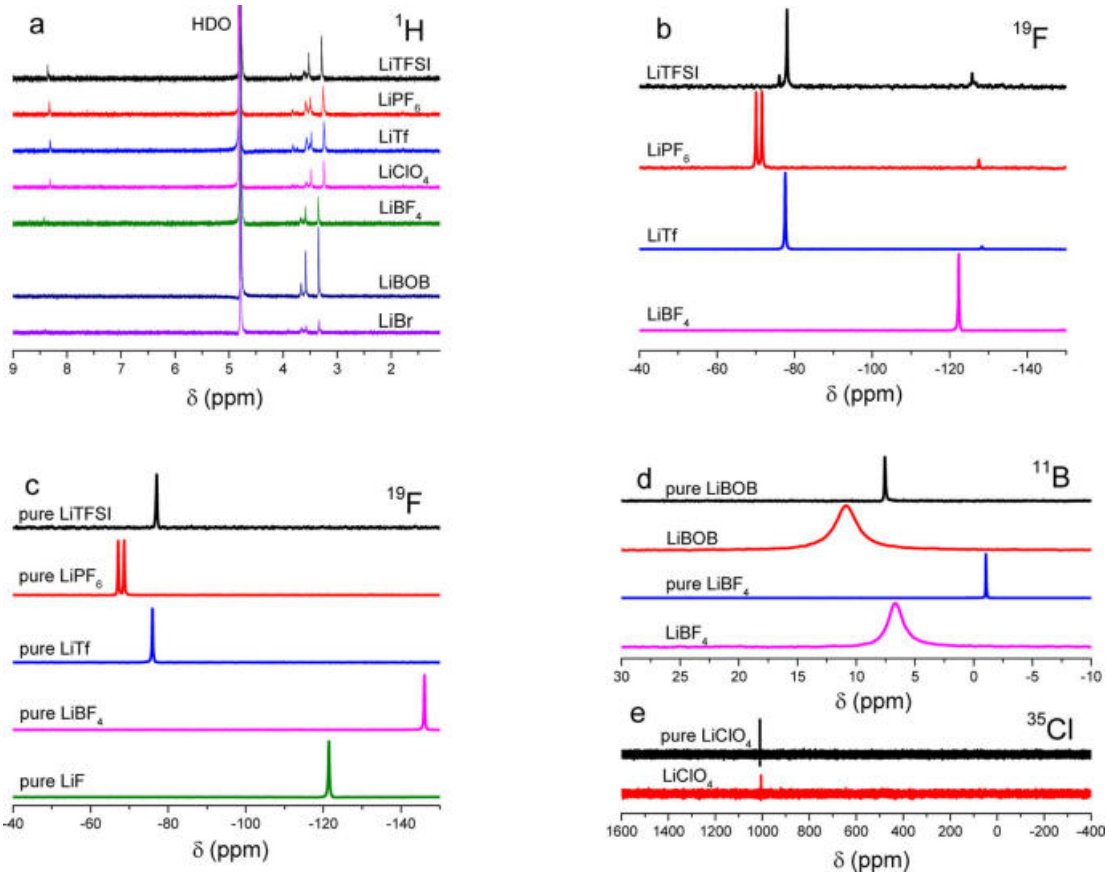

Figure 2.13: NMR usage to characterize electrolyte degradation products for different ether-based electrolytes. Inset a) shows ^{1}H NMR spectra, inset b) shows ^{19}F NMR spectra for discharge products in D_2O, inset c) shows ^{19}F NMR spectra for pure salts in DMSO, inset d) shows ^{11}B NMR spectra, and inset e) shows ^{35}F NMR spectra for discharge products in D_2O and pure salts in DMSO. Reprinted (adapted) with permission from [125]. Copyright (2013) American Chemical Society.

Chapter 3

CHARGE REACTIONS

3.1 Introduction

The biggest challenge in the commercial development of alkali metal-O_2 batteries is reducing the high charging overpotentials caused by the non-conductive nature of the discharge deposits. Such high overpotentials hinder performance by causing side reactions that lead to electrode and electrolyte degradation. The goal of this section is to provide a description of the charging process, focusing on the phenomena that occur at the different stages of charge, including the effects of CO_2 and H_2O. Figure 3.1 shows a schematic of how these stages are defined for both superoxide and peroxide products. The discussion will start with a description of the electronic properties of alkali metal superoxides and peroxides, followed by a description of the phenomena occuring at the different stages of charge. Finally, the use of performance enhancers such as redox mediators is discussed.

3.2 Electronic characteristics of discharge deposits

Previous work has shown that electron tunneling in Li_2O_2 is limited to a thickness of about 5 nm. Beyond that thickness, higher overpotentials are needed to drive the OER [140]. The small magnitude of the tunneling length can be attributed to the insulating nature of Li_2O_2, which is an insulator with an electronic bulk conductivity of about 5×10^{-20} S/cm, while amorphous Li_2O_2 has an electronic conductivity of 2×10^{-16} S/cm [141]. Similar to Li_2O_2, Na_2O_2 has a small electronic conductivity of 1×10^{-19} S/cm [142]. A comparison of the conductivites of different discharge products is shown in Table 3.1.

The dominant defects in both Li_2O_2 and Na_2O_2 include hole polarons (holes trapped at an oxygen, leading to superoxide formation) and cation vacancies (absence of a Li^+ or Na^+ ion), making

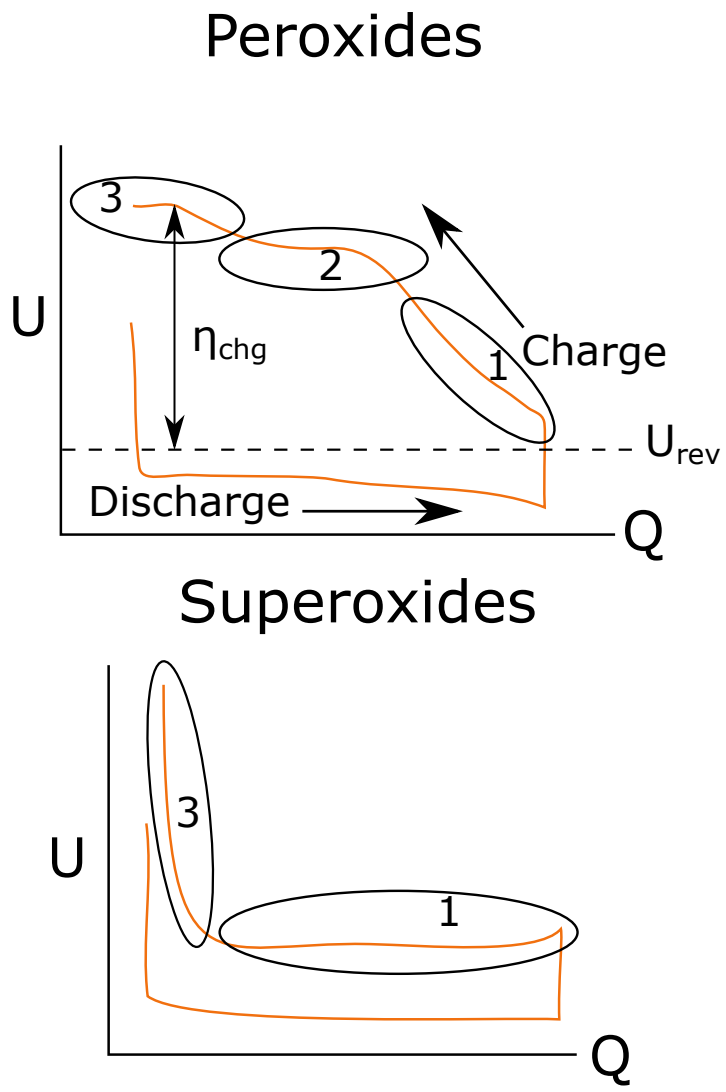

Figure 3.1: Stages of the charging process. The upper plot shows the charge/discharge profile of a battery where the dominant product is a peroxide, while the bottom plot shows the profile of a battery where a superoxide is the dominant product. The different stages of the charging process are marked with ovals, including the relevant sections that discuss each stage. The initial stage of charge is labelled as 1, the intermediate stage as 2, and the final stage as 3. The directions of charge and discharge are shown with arrows.

these peroxide p-type semiconductors. In both Li_2O_2 and Na_2O_2, ionic conductivity originates from the movement of cation vacancies [143–146]. At the equilibrium potential, lithium vacancies ($V_{Li}^{\cdot}$) exhibit positive charge and can become neutral or negative at applied overpotentials. In this case, hole transport occurs though repulsive coulombic scattering at these defects [147]. It is expected that sodium vacancies and holes will exhibit similar behavior; however, previous work has shown that Na_2O_2 cation vacancy diffusion occurs at a slower rate compared to what has been observed in Li_2O_2 [144, 148]. Electrical conductivity is expected to increase with increasing overpotential due to increased concentration of charge carriers. For example, overpotentials of 1 V can lead to conductivity increases of about 10 orders of magnitude [143, 148]. In addition, oxygen-rich Li_2O_2 surfaces exhibit an electronic conductivity over 10 orders of magnitude higher than that of the bulk due to low oxygen coordination leading to the formation of holes [149].

Superoxides exhibit enhanced ionic conductivities compared to those of peroxides. For example, NaO_2 and KO_2 have ionic conductivities around 1×10^{-9} S/cm [142, 150]. Peroxides and superoxides exhibit electronic conductivities within the same order of magnitude. In addition to the differences in ionic conductivity, previous work has found some differences in the nature and relative amounts of defects present in both peroxide and superoxide discharge products.

NaO_2 and KO_2 defect chemistry is dominated by superoxide vacancies ($V_{O2}^{'}$) and cation interstitials, as well as cation vacancies, making both superoxides n-type conductors. In addition, the majority charge carriers are electron polarons, which are electrons trapped at an oxygen in a superoxide site, leading to peroxide formation [142, 150]. Previous work has shown that both NaO_2 and KO_2 are ferromagnetic, yet this observation has no effect on the conductivity [151, 152]. However, smaller increases in overpotential lead to an enhancement in conductivity. For example, an overpotential of 0.4 V is needed to increase the conductivity of LiO_2 10 orders of magnitude, in contrast to the 1 V increase required for Li_2O_2 [145].

3.3 Initial state of charge

The initial charging stage, as shown in Figure 3.1 involves reaction and removal of superoxides and peroxides [13, 59]. However, the discharge products removed initially will have different

Product	σ_{ionic} (S/cm)	σ_{el} (S/cm)	Refs.
Li_2O_2	4×10^{-19} (crystalline), 7×10^{-8} (amorphous)	5×10^{-20} (crystalline), 5×10^{-9} (amorphous)	[141, 143, 153]
NaO_2	1×10^{-9}	1×10^{-19}	[142, 150]
Na_2O_2	5×10^{-20}	1×10^{-19}	[142]
KO_2	1×10^{-9}	N/A	[150]

Table 3.1: Conductivites of discharge products from alkali metal-O_2 batteries.

properties than those removed in further stages. When Li_2O_2 is the main discharge product, this stage will involve the oxidation of amorphous products and small crystallites [59]. This contrasts with what is observed in batteries where superoxide is the main discharge product. In this case, a single plateau at low overpotentials is observed [13, 112]. An interesting scenario occurs when anhydrous $Na_2O_2 \cdot xH_2O$ is present. At the initial steps of charge, the charge profile resembles that of a superoxide battery. This plateau has been attributed to decomposition of hydrated Na_2O_2 [72].

3.3.1 Peroxide charge

The initial stage of charge involves the removal of the most conductive products, such as amorphous Li_2O_2 or O-rich Li_2O_2 on the surface of deposits [93, 154]. In Li_2O_2, the charging process during this stage involves 2 steps: Li^+ removal to produce $Li_{2-x}O_2$, followed by another Li removal step and O_2 evolution [59]. These reactions are shown in Equation 3.1. In general, the overpotentials needed to drive the OER in both Li_2O_2 and Na_2O_2 are in the range of 0.2-0.6 V (depending on the surface) [62, 148, 155]. However, overpotentials as low as 50 mV are needed to form metal-deficient phases of discharge products [148]. For the Li-O_2 system, the proposed rate determining steps for the ORR and OER involve the formation of LiO_2 where LiO_2 formation during OER occurs by delithiation of Li_2O_2 [63]. It is expected that similar behavior will be observed in the

formation of Na_2O_2.

$$\begin{aligned} Li_2O_{2(s)} &\longrightarrow x(Li^+{}_{(sol)} + e^-) + Li_{2-x}O_{2(s)} \\ Li_{2-x}O_{2(s)} &\longrightarrow (2-x)(Li^+{}_{(sol)} + e^-) + O_{2(g)} \end{aligned} \tag{3.1}$$

The nature of the product removed in the initial stage of discharge will vary depending on the discharge product morphology. In small crystallites, it is hypothesized that $(1\bar{1}00)$ Li_2O_2 is removed initially, while O-rich (0001) Li_2O_2 is removed from toroids via solution-like delithiation [154]. Such surfaces are thought to have charging overpotentials of 0.15 V and 0.36 V, respectively [62]. Studies of the morphological evolution of deposits during charge have shown that toroidal deposits evolve to a disk-like shape due to the removal of amorphous discharge products that form at the final stages of discharge [59, 93].

3.3.2 Superoxide products

The initial plateau observed in batteries with superoxide discharge products is related to the oxidation of MO_2 [13, 112]. Similar to what is observed in Li_2O_2, OER kinetic overpotentials for NaO_2 have values in the range of up to 0.2 V [145]. The increased length of the initial charge plateau compared to that of peroxide can be attributed to enhanced solvation of superoxides compared to peroxides since charge transfer through MO_2 deposits is not needed [148]. MO_2 solvation as ionized species (M^+ and $O_2{}^-$) is more favorable compared to that of molecular MO_2 [148, 156]. In turn, this allows OER to proceed via a solution-mediated pathway shown in Equation 3.2.

$$\begin{aligned} MO_{2(s)} &\longrightarrow M^+{}_{(sol)} + O_2{}^-{}_{(sol)} \\ O_2{}^-{}_{(sol)} &\longrightarrow O_{2(g)} + e^- \end{aligned} \tag{3.2}$$

3.4 Intermediate state of charge

The intermediate stage of charge involves the removal of bulk discharge products [154]. At this stage, deposit conductivity starts to play a role in the discharge process [93]. In addition, electrolyte and cathode degradation reactions start to occur [27].

3.4.1 Peroxide products

This stage involves the oxidation of crystalline peroxide deposits [93, 154]. As explained previously, the kinetic overpotentials for delithiation are in the order of 0.2-0.6 V. However, limitations in the conductivity require larger overpotentials to overcome the charge transfer barrier [62, 155]. Meanwhile, the intermediate stage during hydrated Na_2O_2 charge involves the removal of NaOH formed during the discharge process [72].

3.4.2 Electrolyte and cathode reactions

Overpotential-induced electrolyte degradation starts at potentials around 3.5 V. For example, CO_2 evolution in glymes starts at potentials higher than 3.5 V and becomes predominant over 4 V. Also, the formation of carbonates can occur at potentials above 4.5 V [36]. In addition, previous work has shown that carbon electrodes exhibit oxidative decomposition at potentials above 3.5 V [27]. Such decomposition proceeds via superoxide attack at defects on sp^2 carbon to form carbonate and epoxy groups, with carbonate formation being reversible upon charging [157]. Density functional theory studies have shown that defect-free graphene and single walled carbon nanotube surfaces with no defects are stable due to the high energetic barrier [158]. In addition, the superoxide anion produced during discharge can react with some binders and lead to the formation of H_2O_2 [159].

3.5 Final state of charge

This stage involves the oxidation of the last remnants of charge, namely any leftover M_xO_y deposits and products from side reactions, including Li_2CO_3. In addition to having a higher reversible potential (3.82 V vs 2.96 V for Li_2O_2), Li_2CO_3 is less conductive than Li_2O_2, requiring higher

overpotentials than CO_2 for oxidation [160]. Computational work has shown that CO_2 incorporation into an Li_2O_2 deposit can increase the charge and discharge potentials compared to the kinetic overpotentials observed in Li-O_2 discharge, while also decreasing the reversible potential [161]. Experimental evidence has shown that charging overpotentials are higher compared to those of batteries using pure O_2 [106]. The final state of charge is similar to the initial state of discharge due to the small amount of discharge products, with the exception of any parasitic products formed due to degradation of the electrolyte or electrode. Due to the small amount of discharge products left on the cathode, high driving forces are needed to fully remove discharge deposits.

The origin of degradation products can be proved using techniques such as electrochemical mass spectrometry (EMS) [60, 136]. In EMS, the gaseous products evolved from an electrochemical cell are detected by mass spectrometry. Typically, the gas outlet is fed directly to the mass spectrometer for continuous detection. This approach is known as differential EMS (DEMS) and allows the determination of gas evolution rates. On the other hand, an "integrating" approach sample samples at discrete times after gas accumulation [162]. A typical cell has three components: the electrochemical cell, a PTFE membrane interface that separates the electrolyte from vacuum, and the vacuum system including the mass spectrometer [163]. With regards to gas handling, three aproaches are used: flowing a carrier gas (He or Ar) continuously to flush the cell and carry reaction products to the spectrometer, intermittent gas sampling via a closed cell, or continuous detection without using a carrier gas [85].

Differential EMS has been succesfully used to characterize parasitic reactions, as well as characterizing the nature of discharge products [60, 136]. Rreactions can be studied by tracking the evolution of species such as CO_2 and H_2 as a function of state of charge, providing information of where such reactions can occur in the charging/discharging process [164]. In order to deconvolute CO_2 evolution from the cathode and the electrolyte, isotope experiments can be used, where the electrolyte contains a different carbon isotope than the cathode [28, 165]. Characterization of discharge products can be performed by tracking oxygen consumption/evolution as a function of charge capacity. When MO_2 and M_2O_2 are the only discharge products, the expected ratios are 1 and 2 e^-/mol O_2, respectively [69]. Any deviations from these ratios are indicative of parasitic

reactions.

An example of DEMS usage for side reaction characterization is shown in Figure 3.2. Inset a) shows the galvanostatic charge-discharge profile for a Li-O_2 battery with a DME-LiTFSI electrolyte and a ^{13}C cathode. Inset b) shows that O_2 is evolved throughout the charging process, with CO_2 being evolved at voltages between 4 and 4.5 V. CO_2 evolution arised from both the cathode, as shown by $^{13}CO_2$ evolution, and the electrolyte. Inset c) shows the isotopic distribution of products evolved during charge after charging a cell with $^{18}O_2$. The results show that isotopic scrambling occurs, with all $^{x}C^{y}O_2$ evolution occurring between 4 and 4.5 V. The presence of scrambling can be attributed to reactions between the electrolyte and the carbon cathode with Li_2O_2, leading to the formation of Li_2CO_3 [166].

3.5.1 Charge characterization

The observations described in the previous sections have been obtained through the use of techniques such as intermittent titration. Intermittent titration techniques (ITT) such as galvanostatic (GITT) or potentiostatic (PITT) ITT have been used for characterization of cell kinetics and evolution of cell reversible potentials. Figure 3.3 shows experimental data for both techniques. In GITT, current pulses of duration τ and magnitude I_{pulse} are applied. While current is applied, the potential will increase monotonically. Once current is shut down, the system will reach a new steady state voltage [167]. GITT can be used to determine the reversible potential of a cell by measuring the voltage when the system reaches full relaxation after shutting down the current pulse [110, 168, 169]. GITT can be used to distingiush between products oxidized during charge due to differences in the reversible potential.

Meanwhile, in PITT, the potential is stepped a magnitude ΔV at set time intervals and the current response is recorded [170]. Typically, the duration of each voltage step is determined using a current cutoff, where the voltage is stepped once the cutoff is reached. PITT can be useful for characterizing changes in the reaction kinetics at different stages of the charging process [171]. For example, experiments on Li-O_2 batteries have shown the presence of different stages during the charges process [154, 172]. Any stages where solid state diffusion occurs within Li_2O_2 exhibit

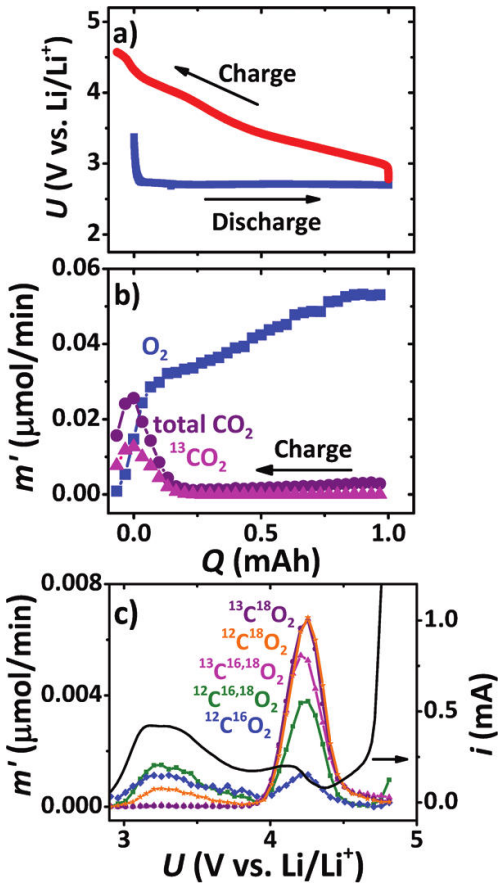

Figure 3.2: DEMS usage for characterization of side reactions. Inset a) shows the galvanostatic charge-discharge profile for a cell with a ^{13}C cathode. Inset b) shows DEMS spectra for different species during the charging process and inset c) shows DEMS spectra taken galvanostatic charge after discharge with $^{18}O_2$. Reprinted (adapted) with permission from [166]. Copyright (2012) American Chemical Society.

profiles where the current increases following a $\sqrt{t}$ behavior, as described by the Cottrell equation. Meanwhile, voltage plateaus related to Li_2O_2 oxidation will show inflection points in the current [154, 172].

The upper portion of the figure shows PITT data. Plot a) shows a charging cycle, with the potential shown in blue and the current shown in red. Three charging stages are identified: stage I, where the potential increases, stage II, where the voltage is steady, and stage III, where the voltage increases. Inset b) shows the voltage and current response in Stage I. The current monotonically decreases after every step, consistent with a diffusion-dominated process. Inset c) shows the current response in stage II. Initially, the current decreases, reaching a minimum, followed by an increase. Once a maximum is reached, the current decreases monotonically. The intial decay was attributed to the formation of defect nuclei within Li_2O_2, while the increase in currrent was attributed to nuclei growth. The later decrease in current was attributed to a decrease in Li_2O_2 content on the cathode. Li_2O_2 response exhibited similar behavior than lithium intercalation materials. Inset d) shows a comparison between the experimental current in stage II and the reported current in previous work, showing that both systems exhibit similar response [172].

The lower portion of Figure 3.3 shows GITT data. Inset a) shows the response throughout the charging process. Inset b) shows the voltage response in stage I, where the reversible potential stays below the reversible potential for Li_2O_2 oxidation, indicating that the dominant phase is non-stoichiometric Li_2O_2 with a lower reversible potential that stoichiometric Li_2O_2. In addition, the charging potential increases after every succesive step. Inset c) shows the voltage response during stage II. In this case, the current increases at every step, followed by a decrease after reaching a maximum. Inset d) shows the voltage response for stage III. In this stage, the charging potential stays steady at a value of 3.6 V, with the reversible potential having a value of around 3.4 V [172]. In addition, the charging capacity exceeds the discharge capacity, indicating the presence of side reactions [173].

In addition to ITT, *in operando* XRD experiments provide information about the nature of products consumed during charge. In contrast to traditional XRD experiments, special cell designs are needed. In-operando XRD cells are mounted in an enclosure equipped with an X-ray transparent

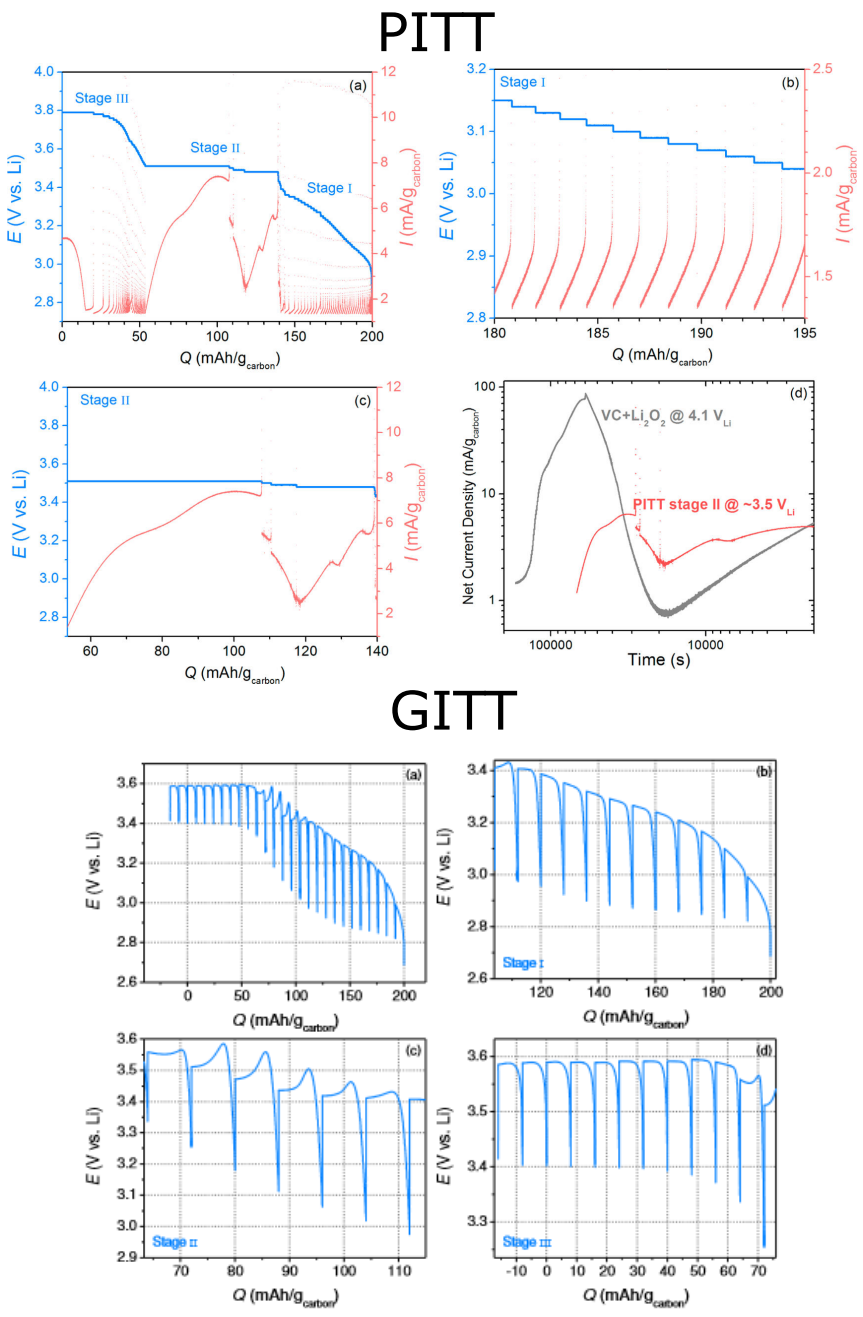

Figure 3.3: ITT experimental data for a Li-O_2 battery. The upper portion shows PITT data for 10 mV pulses with a current cutoff of 1.3 mA/g_C or 50 h duration. Insets a)-c) show current and voltage data, with voltage shown in blue and current in red. Inset d) shows a comparison between the observed PITT current in stage II) and previously reported data [173]. The lower portion shows GITT data. Inset a) shows the overall voltage response for 2 mA/g_C current pulses for 4 h, followed by relaxation for 5 h, while inset b) through d) show the response at the different stages. Reprinted (adapted) with permission from [173]. Copyright (2012) American Chemical Society.

window. Experiments can be performed either using a conventional X-ray source [59] or synchtotron sources [174]. Figure 3.4 shows experimental results from an in-operando XRD experiment on a Li-O_2 cathode. During discharge, the Li_2O_2 (100) and (101) peak intensities increase in a linear fashion. During charge, there is a plateau in the intensity of both peaks, followed by a linear decrease in peak intensity. The initial plateau in diffraction intensity during charge was attributed presence of non-crystalline phases in the surface of Li_2O_2 deposits that are removed in the early stages of charge [59]. In contrast, LiOH deposit evolution during charge and discharge is a continuous nucleation process, where the height:width ratio of the deposits does not change throughout the process [175]. One limitation of such an experiment is that it does not allow for individual particle monitoring or for depth profiling. The higher X-ray flux from a synchrotron allows monitoring the evolution of discharge deposits throughout the electrode, as well as monitoring the growth of individual deposits. Depth profiling experiments have shown that larger crystallites form closer to the cathode, while smaller crystallites form away from the cathode. This can be attributed to O_2 diffusion through the electrolyte, as the availability of oxygen will be decreased further from the air/cathode interface [174]. Meanwhile, individual particle evolution monitoring can be done with the use of a nanobeam (beam with nanometer spot size). Such experiments have revealed that Li_2O_2 oxidation prefentially occurs on the (001) facet, in agreement with previous computational studies that have shown that this surface has a lower charging overpotential [176].

3.6 Performance enhancers

The high charging overpotentials required for oxidizing discharge deposits have led to significant research on additives that might aid the charging process. Such additives include OER and ORR catalysts and redox mediators. Typically, transition metal catalysts are the material of choice. However, such catalysts not only enhance ORR and OER, but they also promote electrolyte degradation reactions [68].

Catalysts for OER and ORR have been widely studied for different applications such as fuel cells and their use has been widely explored as an alternative to reduce overpotentials in Li-air batteries. Among catalysts, transition metals such as Pt, Pd, Au, or Ru have been used in Li-air

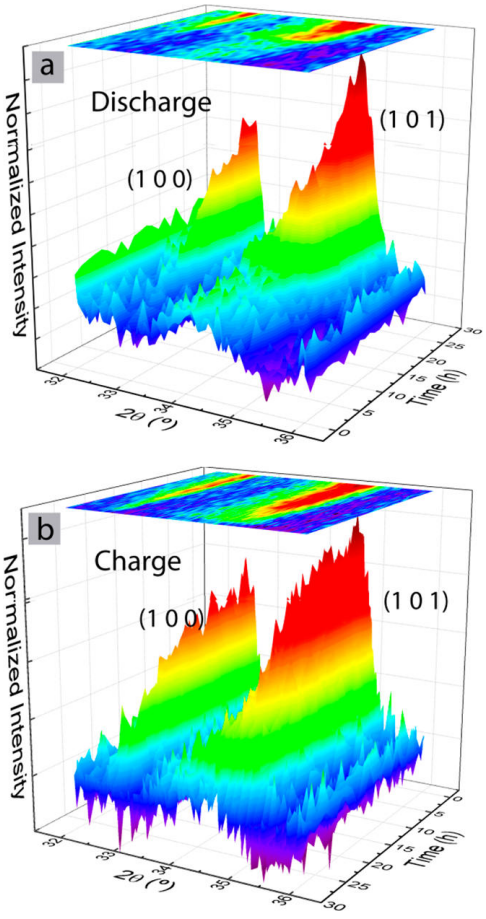

Figure 3.4: In-operando XRD data for a Li-O_2 cell. Insets a) and b) show the time evolution of the intensity of the (100) and (101) Li_2O_2 peaks [59]. Reprinted (adapted) with permission from [59]. Copyright (2014) American Chemical Society.

batteries with some success [177, 178]. Due to the high cost of metal catalysts, nanoparticles (NP) have been considered as a way to reduce loading and improve activity. In addition to electrolyte degradation, one issue is that metal catalysts can improve one property of the cathode in detriment of another. The use of bimetallic NP has been used to combine the advantages of two metals and improve multiple performance metrics [179].

Besides metals, transition metal compounds have also been studied as catalysts due to lower cost than transition metals. Some catalysts previously studied include oxides such as Fe_2O_3, Co_3O_4, MnO_2, RuO_2, or CuO [165, 180]. Other oxides that have attracted interest include transition metal perovskites that have been used as SOFC cathode materials such as LSCF [181]. The good performance of such catalysts can be attributed to multiple mechanisms. For example, the α-MnO_2 polymorph can reduce charging overpotential by its ability to incorporate Li^+ and O_2^{2-} into the crystal structure [92, 182]. In addition, Co_3O_4 and aids charge due to improved electron transfer with Li_2O_2 [170]. Meanwhile, Fe_2O_3 improves charging performance due to preferred Li_2O_2 growth on the catalyst over the carbon substrate, as well as inducing epitaxial growth of Li_2O_2 due to lattice matching between Li_2O_2 and Fe_2O_3 [183] Besides oxides, metal carbides such as Mo_2C have shown good performance. The performance of this composite was attributed to a thermodynamically favorable oxidation of Mo on the surface of the particle, with the oxide layer being metallic and noncrystalline, facilitating electronic transport [184].

Aside from catalysts, redox mediators have been considered as a way to reduce overpotentials. The mechanism of operation of redox mediators is shown in Figure 3.5. A redox mediator is a molecule that can be reversibly oxidized or reduced at a potential different than that of Li_2O_2 [185]. Upon oxidation or reduction, the mediator can act as an electron transfer agent. For example, an agent used to aid discharge will be reduced on the cathode, diffuse in solution, and then reduce O_2 to Li_2O_2. In this case, the use of a redox mediators during discharge can promote discharge via the solution mechanism. Redox mediators used to aid discharge include 2,5-ditertbutyl-1,4-benzoquinone (DBBQ) [186]. Meanwhile, an agent used to aid charge will be oxidized at the cathode, diffuse in solution, and then oxidize Li_2O_2. Some mediators that have been considered include tetrathiafulvalene (TTF) [187], 2,2,6,6-tetramethylpiperidinyloxyl (TEMPO) [188], tris[4-

(diethylaminophenyl)amine] (TDPA) [189], and LiI [190]. Some redox mediators can have more than one redox couple, such as TDPA [189] and TFF [187].

As explained previously, redox mediators can aid both discharge and charge. However, a mediator that aids charge will be ineffective during discharge and viceversa [185]. When using redox mediators, several considerations are needed. First, the mediator should not induce parasitic reactions with the electrolyte or the anode. Therefore, the reversible potential must be chosen carefully [185]. In addition, due to the ionic nature of the redox mediators during use, solvent-mediator interactions need to be considered and can be used to control the discharge or charge potential. Namely, the DN and AN of the solvent are important when using mediators for charge and discharge, respectively [185]. Another issue that can arise is poor connectivity of discharge deposits when using a mediator for discharge [186]. In such a case, it is also necessary to include a mediator for the charging process.

In addition to the mediators described previously, H_2O might also behave as a charging mediator [115]. In contrast to the mediators described previously, H_2O is consumed during the reaction. Further complications exist as H_2O can cause side reactions [115]. H^+ present in the electrolyte by either addition of acid or water electrolysis can aid in the charging process by reacting with Li_2O_2 to produce H_2O_2 and Li^+, as shown in Equation 3.3 [46].

$$\begin{aligned} H_2O_{(sol)} &\longrightarrow 2e^- + 2{H^+}_{(sol)} + 0.5\,O_{2(g)} \\ 2{H^+}_{(sol)} + Li_2O_{2(s)} &\longrightarrow H_2O_{2(sol)} + 2{Li^+}_{(sol)} \\ H_2O_{2(sol)} &\longrightarrow O_{2(g)} + 2e^- + 2{H^+}_{(sol)} \end{aligned} \tag{3.3}$$

An additional mechanism to increase discharge capacity in Li-O_2 batteries involves the use of other cations such as K^+. In such a case, the enhanced capacity was attributed to an increase in the concentration of superoxide in solution, leading to discharge via the solution pathway [191, 192].

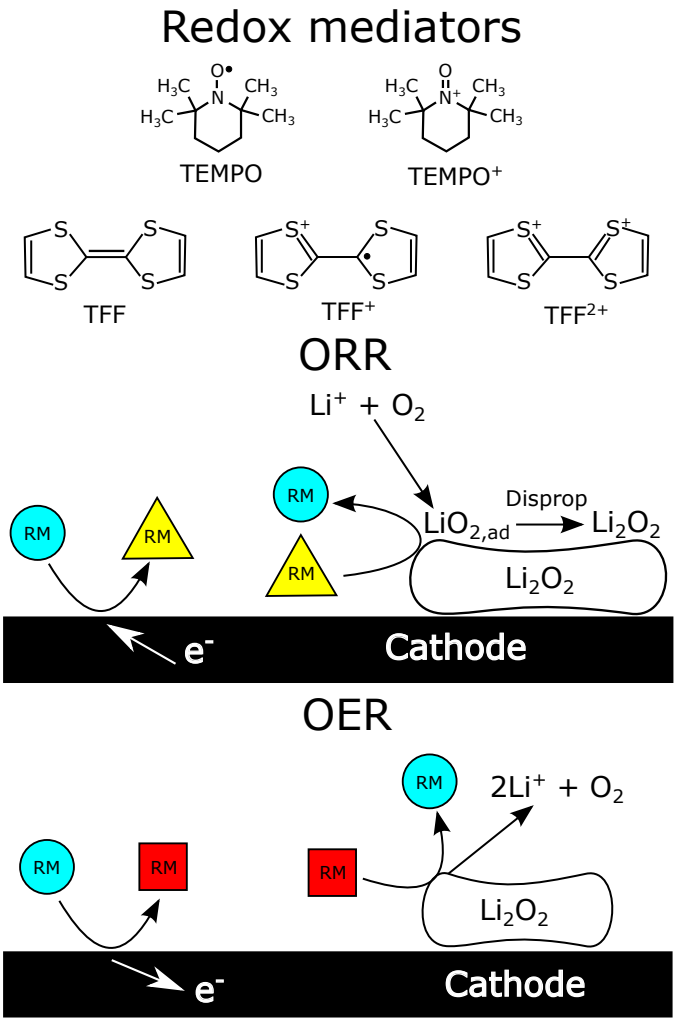

Figure 3.5: Redox mediator mechanism of operation. The upper portion shows the chemical formula of TEMPO and TFF, including their oxidation states. The middle portion of the figure shows redox mediator operation for discharge, while the lower portion of the figure shows redox mediator operation for charge. The neutral mediator state is shown as a cyan circle, the oxidized state is shown as a red square, and the reduced state is shown as a yellow triangle.

Chapter 4

STAGE-BY STAGE CHARACTERIZATION OF BATTERY CHEMISTRY

4.1 Introduction

Most studies to characterize alkali metal-O_2 chemistry involve the use of batteries, followed by post-mortem cathode analysis. This characterization is typically done at the end of one or more discharge-charge cycles; however, some studies have used characterization during partial discharge [93, 102]. A significant issue with such an approach with respect to battery technology in general is the variability in battery behavior due to different cathode materials and microstructures, as well as electrolyte formulations. Battery operation involves multiple processes occurring in concert, namely reaction kinetics, mass transport, and conductivity barriers to charge transfer. In order to better characterize each process, it is necessary to develop strategies that allow separating their effects. One alternative to study reaction chemistry in isolation involves the use of glassy carbon electrodes in electrochemical cells using techniques such as cyclic voltammetry [18, 193], rotating disk electrodes [194], or galvanostatic discharge [140]. However, most of these studies have not characterized deposit and reaction evolution as the discharge process occurs. In this section, the concepts of well-defined surface and kinetically relevant states for reaction chemistry characterization are introduced. The use of such an approach would provide information that would enable better material design, including cathode microstructure.

4.2 Comaprison with other electrochemical systems

Figure 4.1 shows a comparison between the discharge curves of a Na-O_2 battery and polymer electrolyte membrane (PEM) fuel cell polarization curves. Generally, the battery curves has 2 regions: a constant overpotential region and a steep drop-off in potential towards the end of discharge. However, as discharge rate increases, the plateau converts to a downward path of progressively

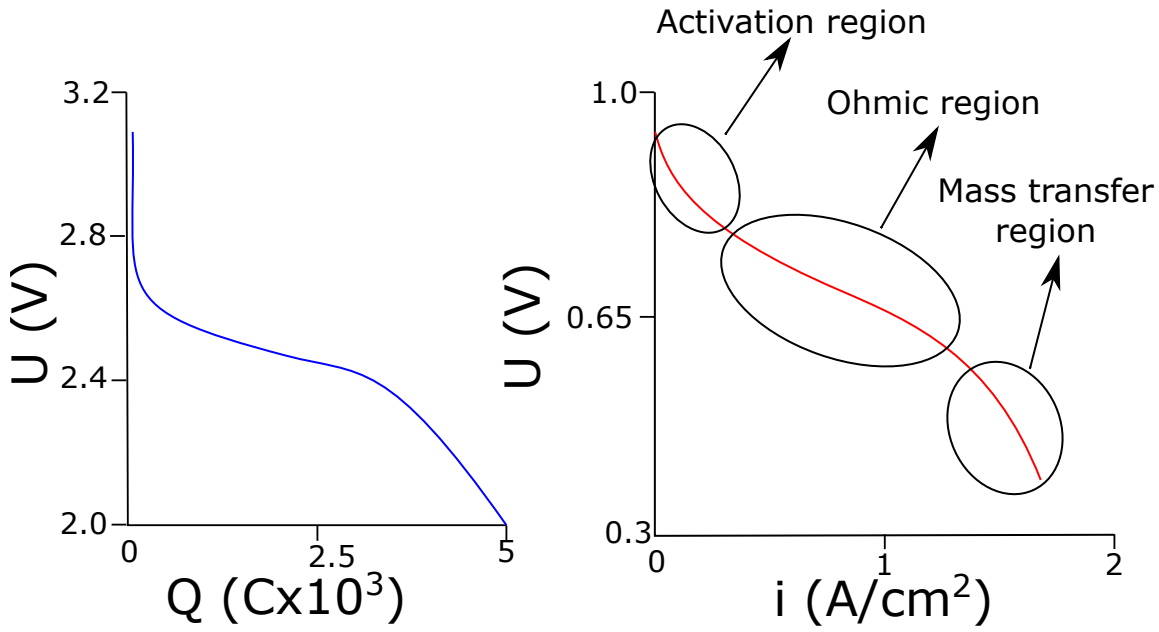

Figure 4.1: Li-O_2 battery discharge and PEM fuel cell polarization curves. The left plot shows a galvanostatic discharge profile for a Li-O_2 battery and the right plot shows a polarization curve for a PEM fuel cell. Adapted from References [140] and [196].

increasing slope. Meanwhile, the PEM polarization curve has 3 distinctive regions: a polarization region at high potentials, an ohmic region at intermediate potentials, and a diffusion (mass transfer) region at low potentials. The polarization region is attributed to kinetic barriers for electron transfer reactions at the electrodes, while the ohmic region occurs due to internal resistance of the electrolyte, and the mass transfer region occurs due to reagent depletion near the electrode [195].

Upon inspection, there are several similarities between the battery (B) and fuel cell (FC) curves. . First, both curves have 3 stages that show similar behavior. At low discharge capacity (B), the steep drop in potential may be due to kinetics limitations associated with initial deposit growth. For the FC, the steep drop at low current is known to be the result of kinetic limitations. Finally, a steep drop in potential occurs at high current/capacity. The intermediate regions, which involve an approximately linear decay in potential arise from conductivity limitations in the growing deposit

(B) and electrolyte resistance (FC). The steep decay in potential represents either mass transfer resistance or sudden loss of conductivity in the battery and mass transfer limitations in the fuel cell. While the regions of the polarization curve are well defined for the fuel cell, they are less so for the battery. The intent of this analysis to develop the framework for describing battery discharge and charge characteristics in a manner generally applicable to a range of batter chemistries. Section 4.3 describes a fundamental approach to do such a characterization using WDSS.

4.3 Well-defined surface states

A logical extension of the previous kinetic studies involves characterizing reaction kinetics [154, 172] as a function of Li_2O_2 surface coverage and deposit size. A similar approach has been used previously to characterize charge, where cathodes pre-loaded with Li_2O_2 particles were used as electrodes [197]. However, these studies used commercial Li_2O_2, and their morphologies, sizes, and compositions (crystalline vs. amorphous) did not match those of electrochemically grown deposits [59, 197]. An alternative to this involves the use of well-defined surface states (WDSS) where measurements are made of a carbon surface in a well-defined state at a particular point during the discharge process. Figure 4.2 shows a depiction of the use of WDSS for reaction characterization. The Figure shows 3 surfaces, referred to as A, B, and C, representing different stages in the discharge process. State A represents a fully charged cathode; state B represents a cathode where Li_2O_2 nucleation has started to occur; and state C represents a state of full coverage.

The use of WDSS to characterize alkali metal-O_2 battery chemistry is analogous to the use of single crystals in surface science. Their use provides significant advantages such as ease of design of *in operando* experiments and a well-defined surface for characterization of the reactions occurring during the charge and discharge processes. However, selection of such states can be complex due to a need to separate surface reaction phenomena. The exceptions are the intial states of charge and discharge, where the cathode is either completely covered with discharge deposits or a pristine electrode, respectively.

Typically, battery characterization is performed by galvanostatic discharge/charge cycles, with the corresponding voltage being recorded as a function of discharge capacity. An alternative in-

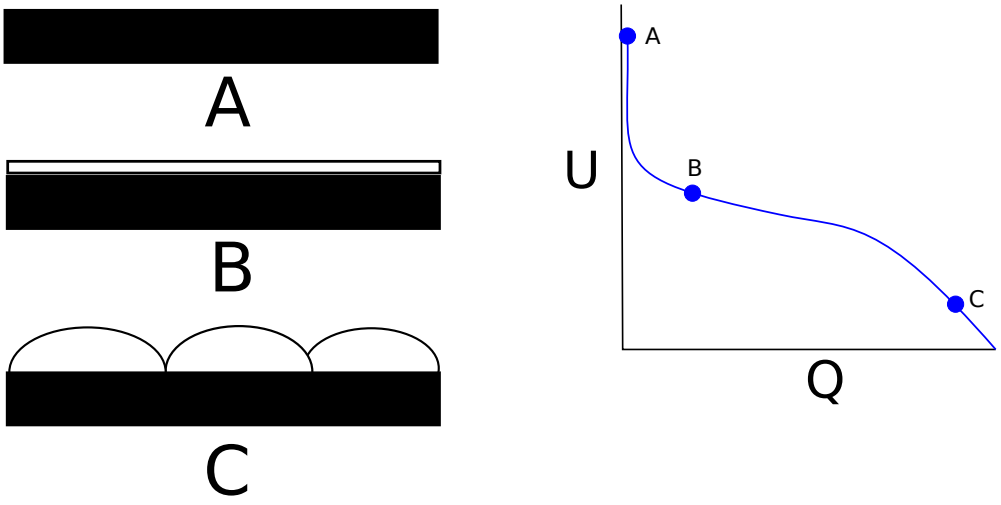

Figure 4.2: Well-defined surface state depiction for discharge. The left portion of the figure shows 3 states: A, B, and C, representing the different stages of discharge. The location of such states in a discharge curve is shown on the right.

volves potentiostatic discharge, where voltage is held at a constant value and current is recorded [154, 197]. The galvanostatic method is useful for simulating a device load on a battery, although the potential changes throughout the measurement. For a fundamental study, potentiostatic processes are advantageous, as the driving force is held to a constant, while the reaction rate changes throughout the discharge/charge process. This is analogous to what is done in catalysis and surface science studies. In addition, well-designed traditional electrochemical experiments such as cyclic voltammetry [18, 193] or impedance spectroscopy [140] can be used to obtain fundamental insight. Such experiments can be completed with the use of *in operando* techniques such as electrochemical AFM [198] or ambient pressure XPS [199] to further understand morphological evolution, as well as the chemical nature of species formed. Such experimental considerations are described in Section 4.5.

4.4 Kintetically relevant states

The WDSS described in Section 4.3 can provide fundamental information about the reactions occurring in alkali metal-O_2 batteries under conditions for which a WDSS cannot be identified. In batteries, phenomena such as reduced O_2 availability due to pore clogging [102], O_2 gradients across the pores of the electrode [89, 103], presence of active regions in the cathode, and non-uniform particles sizes and distribution require the use of an alternative way to define battery states. One alternative involves analyzing discharge/charge profiles and characterizing the state of the cathode whenever there is a change in slope or a plateau. Such states can be referred as kinetically relevant states (KRS).

Figure 4.5 shows experimental charge/discharge profiles for the categories described in Section 1.4. In all cases, the discharge curves exhibit similar behavior, with a plateau or sloping region over up to 80% of maximum charge. This is followed by a steep drop in potential and cell death. Meanwhile, the charge curves are different for each of the 4 types of profiles. For example, profile 1B exhibits 3 regions: a region with a steep increase at the beginning of charge, a moderate slope region that encompases most of the charge, and a region where the slope increases starting at 80% of charge. In such a cases, at least one key state will be required for each stage to accurately

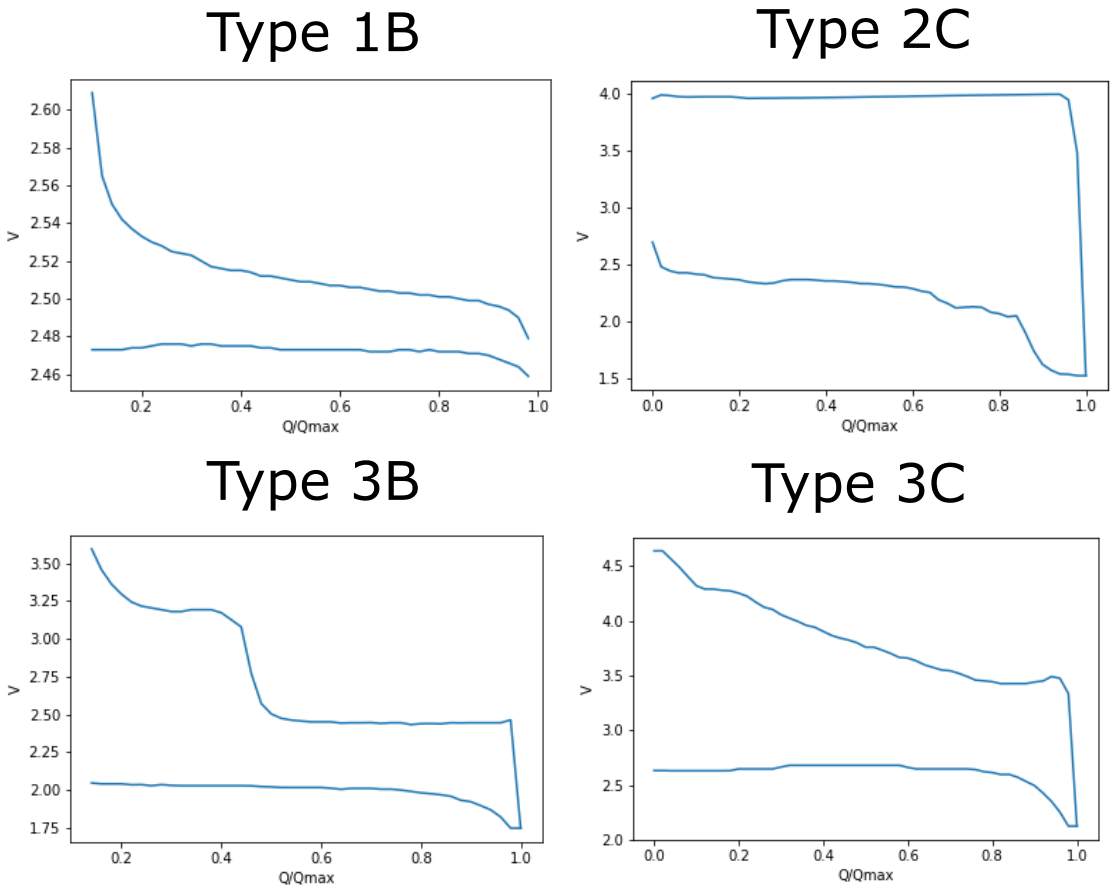

Figure 4.3: Sample charge/discharge profiles for alkali metal-O_2 batteries. The profiles are classified based on the system described in Section 1.4. Adapted from [12, 61, 70, 72].

describe the phenomena occurring in the battery. Meanwhile, profile 2C has 2 stages: an initial stage where the potential increases steeply to about 4 V, followed by a plateau that encompasses the rest of the charging process. In this case, at least 2 states will be needed to describe the system: one per region.

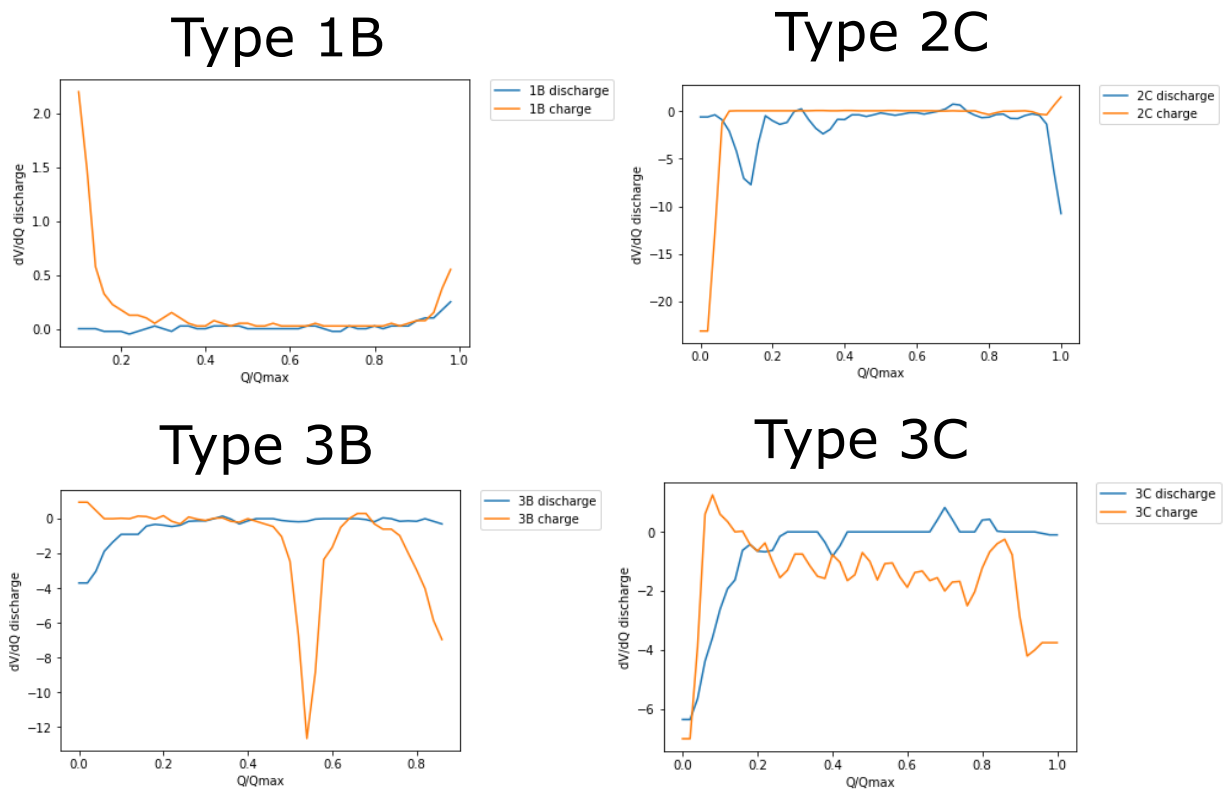

Figure 4.4: First derivative plots for the charge/discharge profiles shown in Figure 4.3.

4.4.1 Determination of KRS

In contrast to WDSS determination, the determination of KRS is straightforward. Figure 4.5 shows first derivative plots as a function of charge, Q, for the 4 charge/discharge profiles shown in Figure 4.3. Using the first derivative provides a better way to visualize plateaus and adequately identify regions where the voltage changes rapidly. In addition, other KRS choices include mid-points in plateaus or any regions where the slope is constant.

Consider case 3B in Figure 4.5, which includes 5 discharge KRS: initial (D1) and final discharge (D5), as well as 3 intermediate regions (D2, D3, and D4). Meanwhile, 7 charge KRS were identified: initial charge (C1), 2 states at the middle of plateaus (C2 and C6), and 4 additional states located in transition regions (C3, C4, C5, and C7).

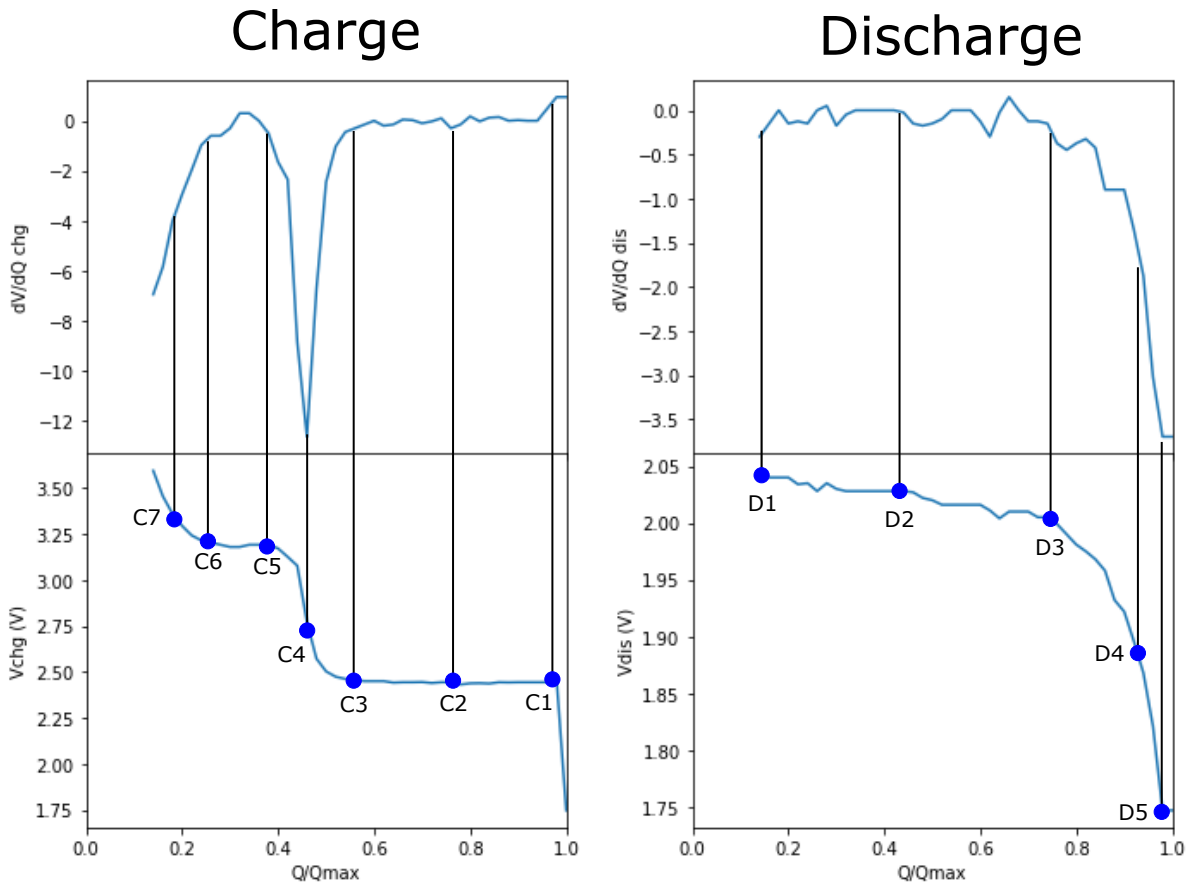

Figure 4.5: Key state selection for profile 3B in Figure 4.3. The left side shows KRS determination for the charge process, while the right side shows KRS determination for the discharge process. In each case, the first derivative of the charge/discharge profile is shown on top, while the measured voltage is shown at the bottom. The discharge states are labelled as "Dn", where n is the state number and charge states are labelled as "Cn".

4.5 Experimental considerations

In operando experiments can be used to determine each WDSS. The initial stage of nucleation proves particularly challenging due to the small size of Li_2O_2 deposits. For the initial stage of discharge, *in-situ* transmission electron microscopy (TEM) can prove useful to map deposit distribution and growth [200]. Other techniques such as transmission X-ray microscopy [113] or Raman spectroscopy [96] can prove useful as they provide spatial information about deposit location, as well as depth profiling. In addition, WDSS can potentially be used to monitor conductivity changes in deposits via the use of techniques such as electrochemical atomic force microscopy (AFM). Concerning electrochemical experiments, potentiostatictechniques such as PITT [154, 172] could be coupled with any of the techniques described previously to provide spatial and temporally resolved information about deposit growth, while relating to the different stages of a charge/discharge curve.

Another important aspect is that the use of WDSS is not limited to using carbon surfaces. For example, WDSS for Li_2O_2 can be defined to include toroidal deposit growth and nucleation. Previous work has shown that toroids grow as laminae of Li_2O_2 grow and stack-up [91]. Other studies have shown that water present in the electrolyte leads to the formation of Li_2O_2 laminae [67]. Experiments to characterize this phenomenon might include growing Li_2O_2 films and exposing them to water or electrolyte-anion combinations, followed by characterization of any species adsorbed on the laminae surface. The detection of water or adsorbed anions on the surface might indicate their role as capping agents directing the growth of Li_2O_2 [201]. In addition, the presence of adsorbed water on the surface might enhance charge transfer during charge [202].

In operando techniques can also be used to characterize KRS. For example, X-ray tomography can be useful to determine the regions of the cathode where deposit growth is preferred, as well as changes in morphology and size at the different stages of the cathode. Similar to what was described in the WDSS experiments, *in operando* techniques can be coupled with traditional electrochemical experiments to characterize the time evolution of deposit growth, as well as characterizing the effects of growth conditions (temperature, applied potential, nature of the cathode) in discharge/charge.

4.6 What can key and well-defined surface states tell us?

The concepts described previously can be used as a fundamental approach for alkali metal-O_2 chemistry characterization. In this section, three case studies focusing on the use of key and well-defined surface states will be provided, emphasizing the use of techniques and useful information that can be obtained. Most of the studies described use *in operando* techniques. However, it is possible to use *ex situ* characterization techniques when experiments are well designed.

4.6.1 Initial discharge characterization (first monolayer), nucleation, and deposit growth

Previous studies have attributed differences in initial discharge behavior to the formation of the first monolayer [172]. After monolayer formation, modeling results have shown that deposit growth occurs via a nucleation mechanism [203]. In addition, discharge current has an effect on the mechanism, where solution nucleation and precipitation occurs at low discharge currents and surface mediated growth at high discharge currents. There is a small amount of work focusing on fundamental insight regarding these processes. A better understanding of nucleation and deposit growth would allow for improved cathode material choices, enabling better morphological control and possibly, reduced charge overpotentials.

Previous work on epitaxial film growth and electrodeposition has revealed several growth mechanisms, shown in Figure 4.6. Near equilibrium, three possible growth modes are possible: Frank-van der Merwe (FM) growth, Volmer-Weber (VW) growth, and Stranski-Krastanov (SK) growth [204]. In FM growth, the material grows monolayer by monolayer, leading to a uniform film. Meanwhile, VW occurs when nuclei form and growth occurs via nucleation. SK involves both FM and VW growth, where initial growth occurs via a FM mechanism. Once the substrate is covered with a monolayer, growth proceeds via the VW mechanism. The mechanism of growth is affected by factors such as the surface free energies of the substrate, overlayer, the interfacial free energy, and lattice mismatch between the substrate and the overlayer [204]. FM growth can occur at low deposition rates, when surfactants are present, or overlayer-overlayer interactions are more favorable than overlayer-substrate interactions [205, 206]. Outside of equilibrium, VW or

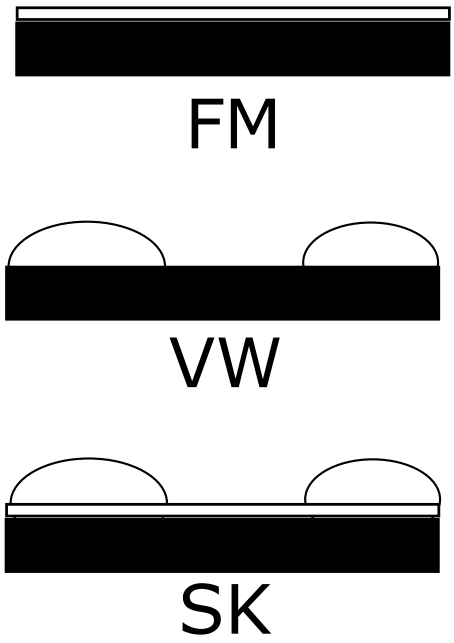

Figure 4.6: Deposit growth mechanisms. The Frank-van der Merwe mechanism is labelled as FM, the Volmer-Weber mechanism is labelled as VW, and the Stranski-Kastranof mechanism is labelled as SK.

SK growth are favored, but it is possible to achieve FM-like growth when a high density of small nuclei is present [204].

Deposit growth evolution can be characterized in a fundamental way using planar disk electrodes or single crystals. In such experiments, an electrochemical cell can be galvanostatically discharged, followed by characterization. Conventional characterization techniques can be used, but *in situ* techniques such as scanning probe microscopy can prove advantageous as analysis can be done during the experiments [198, 206, 207]. One key difference between alkali metal-O_2 batteries and a traditional epitaxial growth or electrodeposition experiment is the presence of soluble products, followed by precipitation elsewhere. Experiments can be performed using different electrolytes and substrates, as well as analyzing the effect of electrode surface treatments (ion implan-

tation, coatings, etc) on the morphological evolution. Such experiments could also provide insight about the effect of the substrate in solvation, as the adhesion strength of MO_2 might provide an energetic barrier to solvation. In substrates where strong binding occurs, deposits will grow via a FM mechanism. Meanwhile, in a substrate with weak binding, growth will occur via the VW mechanism.

4.6.2 Spacial distribution of discharge products within deposits

The use of *in operando* techniques such as X-ray diffraction [59] and X-ray tomography [87] has enabled workers to understand the nature of products removed during the different stages of charge, as well as monitoring the morphological evolution of deposits during discharge. In addition, the use of techniques such as transmission x-ray microscopy has provided information about the chemical identity and distribution of compounds within discharge deposits [113]. However, the information known about the evolution of discharge products throughout battery cycling is limited. This section will describe the use of WDSS and KRS to characterize such phenomena.

Well-defined surface states can be used to obtain chemical information via *in operando* techniques such as ambient pressure XPS [173, 199]. In such an experiment, deposits would be grown on the pristine electrode surface (the WDSS) and characterization would occur at set intervals. The experimental information obtained in such experiments could supplement previous SERS experiments that have probed the lifetime of superoxide discharge products, with the added benefit of providing spatial resolution. In addition, conductive AFM might be used to obtain local conductivity maps of discharge deposits in Li-O_2 batteries [208]. Due to the differences in conductivity between amorphous and crystalline deposits, amorphous deposits will exhibit a higher electrochemical response than crystalline deposits. By monitoring how the response changes as a function of discharge/charge, it might me possible to obtain spatiotemporal information about the evolution of the crystalline nature of discharge deposits.

Chemical information about discharge deposits, obtained at KRS on the discharge curve, can be obtained using transmission x-ray microscopy. Previous studies have done similar characterization using an *ex situ* approach, however these studies focused on characterization at the end

of discharge [113]. In addition, deposit conductivity evolution as a function of discharge capacity can be measured using conductive AFM. In such an experiment, discharge deposits could be grown in carbon nanotube electrodes, followed by cathode removal, and discharge deposit characterization. A similar approach has been used for *in situ* TEM, where carbon nanotubes were discharged, followed by construction of a solid state battery with a nanotube from the discharged cathode embedded between two electrodes: a Li-conductive Si nanowire and a gold substrate. Charge characterization was then performed at an applied bias, with the Li-conductive electrode being in contact with discharge deposits [209]. An AFM *in situ* version of this experiment would involve discharging a carbon nanotube cathode, followed by construction of an electrochemical cell using a nanotube from the discharge cathode. In contrast to the solid state battery used in the TEM experiment described previously, the AFM experiment can be performed in the presence of a liquid electrolyte.

4.6.3 Plateaus and inflection points during charge

Previous studies have shown that discharge behavior for Li-, Na-, and K-O_2 batteries is fairly uniform: an initial drop of overpotential is folllowed by a plateau that lasts throughout the discharge process, followed by a steep drop in potential. In contrast, charging behavior is more complex, with charging profiles exhibiting a series of plateaus, ramps, and exponential increases [60]. Previous studies have connected the shapes of charging profiles to the presence of certain discharge products in Na-O_2 batteries [13]. In addition, the presence of plateaus and stages has been related to the oxidation of different discharge products [13, 154]. Despite the significance of these phenomena, few fundamental studies have attempted to address these issues. This section describes a framework that could be used to obtain further insight about the processes occuring during charge.

Well-defined surface states can be used to characterize the different stages of charge using a combination of conductive AFM and isotope alternation experiments. In isotope alternation experiments, discharge is first done up to the WDSS of a monolayer (or the equivalent amount) with one isotope. After current is set to zero, the electrolyte is purged from oxygen, followed by isotope switch and continuation of discharge. A schematic of this experiment is shown in Figure

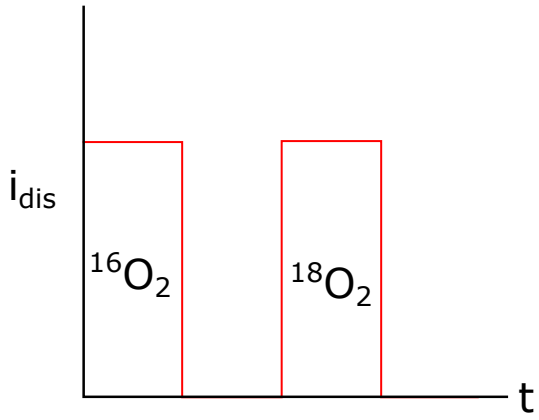

Figure 4.7: Schematic of isotope alternation experiments. The solid, red curve shows the applied current to the cell as a function of time. Meanwhile, the isotope used in each part of the discharge process is shown as a label below each step.

4.7. In between isotope transitions, *in operando* experiments can be performed to determine the nature of the products formed on the surface. At the end of the experiment, the electrolyte is purged again prior to charge. During charge, DEMS can be used to monitor isotope evolution and connect the different regions of charge to the products detected during charge. In addition to using flat electrodes, such experiments can be performed with porous electrodes using a key state approach.

Chapter 5
THEORY OF FIELD EMISSION

The phenomenon of field emission has been known since the 18th century. However, it was not properly understood until the early 20th century [210]. The development of field emission theory enabled its usage for different applications such as studying surface chemistry through the use of field emitter tips, which are sharp needles or whiskers with hemispherical apexes having a radii of a few hundred Angstroms. The use of emitter tips provides the advantage of achieving high electric fields (on the order of several V/Å) with voltages on the order of a few kV, making them ideal for reproducing electrode/electrolyte interfaces [211]. Emitter tips are commonly made with metals (such as Pt or W) or semiconductors since such materials can sustain the high voltages needed for field emission. High purity materials with ordered crystalline structures are preferred since tip failure commonly occurs at grain boundaries [212]. This chapter will provide a description of the physics occurring during field emission and ionization, techniques used to study surface chemistry with field emitter tips, and examples of the application of such techniques.

5.1 Field emission

Field emission is the emission of electrons by materials under the application of an electric field [210]. Surface electric fields can be generated in an emitter tip by applying a potential. The surface electric field in the tip can be described by Equation (5.1), where E_{app} is the applied electric field, V is the applied potential, k is a shape factor (5 for a hemispherical tip), and r is the radius of the tip [213]. A schematic of a tip is shown in Figure 5.1.

$$E_{app} = \frac{V}{kr} \tag{5.1}$$

The existence of field emission was first proposed by Fowler and Nordheim in 1928 [214]

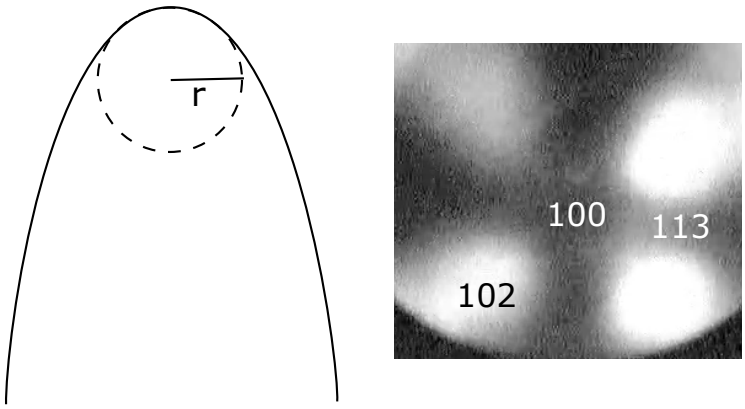

Figure 5.1: Schematic of a field emitter tip. Inset a) shows a schematic of a field emiter tip with the tip radius labeled as r. Inset b) shows a FEM image of a Pt tip. Areas with a lower work function can be seen as brighter spots.

and the first field emission microscope (FEM) was developed by Müller in 1936 [215, 216]. The principle of operation of the FEM involves modifying the barrier for electron emission to vacuum. The barrier for emission for electrons in the Fermi level (E_F) to vacuum is known as the work function (ϕ). Typical ϕ values for metals are around 5 eV. Figure 5.2 shows the barrier as a function of position. Under no applied field, the barrier can be represented as shown in inset a of Figure 5.2. However, when an electric field is applied, the barrier is bent as shown in inset b of Figure 5.2, allowing electron tunneling.

Crystal facets within the same material have different work functions, making it possible to obtain an image of the tip. In a FEM image, areas with a lower work function are shown as brighter spots. A FEM image is shown in inset b) of Figure 5.1.

5.1.1 Fowler-Nordheim equation

Field emission of electrons can be described using the model proposed by Fowler and Nordheim in 1928 [214]. The Fowler-Nordheim (FN) model was proposed as a way to simplify previous work

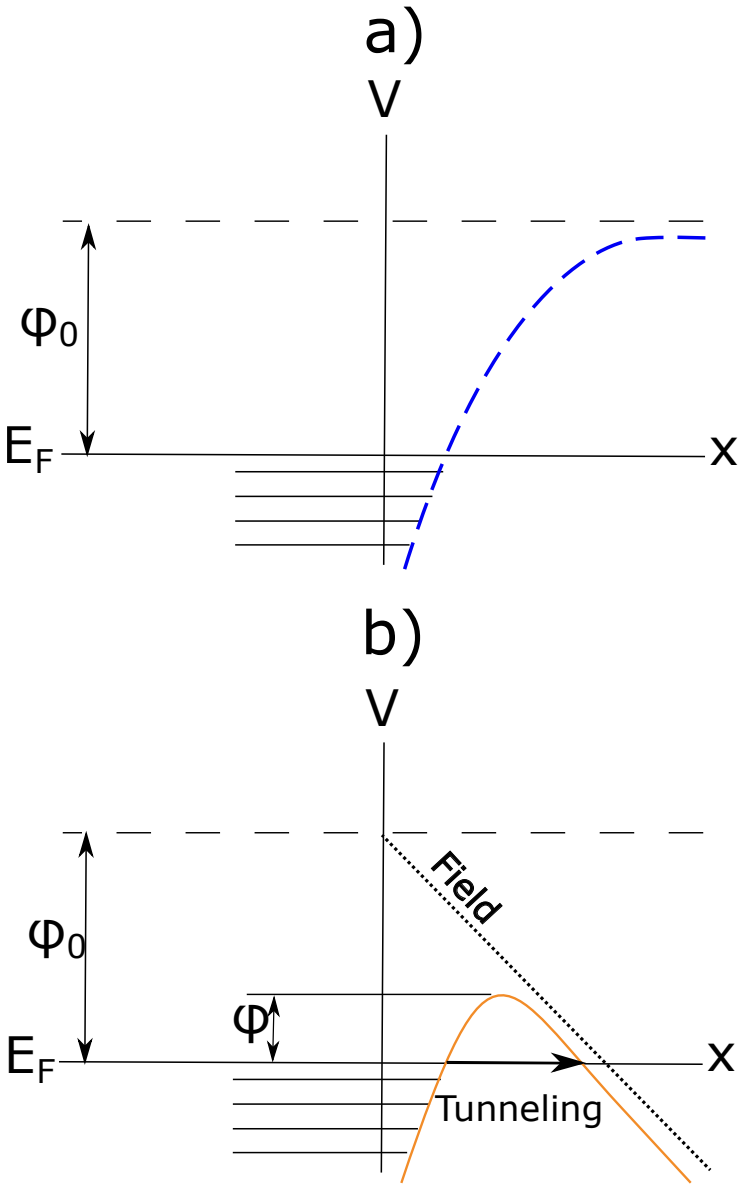

Figure 5.2: Depiction of field emission barriers. The x-axis of both plots represents the distance from the surface, while the y-axis represents electron energy. Inset a) shows the energy diagram under no applied field, while inset b) shows the diagram under an applied field. Under such a field, the work function decreases from a value of ϕ_0 to ϕ. Adapted from Tsong [216].

done in thermionic (thermally induced) emission and as a way to develop an independent model for field emission. The FN equation is the solution of Schrödinger's equation using Sommerfeld's electron theory of metals. The equation is solved for a rounded triangular barrier, similar to that shown in Figure 5.2. From this result, the tunneling probability can be calculated [214]. The FN predicted that field emission would be sensible for fields around 0.1 V/Å and becomes significant at fields around 1 V/Å (for reference, Pt can be imaged using FEM at fields around 0.43 V/Å). Unification of thermionic and field emission models was developed by Murphy in 1956 through a definite integral that is a function of temperature, electric field, and work function. The integral can then be evaluated to yield expressions for thermionic emission (high temperature and low field), field emission (high field and low temperature), and a narrow intermediate region. Murphy's model features the use of a more accurate electron potential and the use of the Wentzel-Kramers-Brillouin (WKB) approximation [217]. In addition to the use of the WKB approximation, the following assumptions are made [212]:

- Metal with free electron band surface
- Electrons in thermodynamic equilibrium and obeying Fermi-Dirac statistics
- Metal at zero temperature
- Smooth, flat surface
- Uniform local work function independent of electric field
- Uniform electric field above the emitting surface
- Applicability of a classical image potential between electrons and the surface

Murphy's form of the FN equation at low temperatures is given by Equation 5.2

$$I = \frac{\alpha E^2}{\phi} exp(-\frac{\beta \phi^{\frac{3}{2}}}{E}) \tag{5.2}$$

where E is the applied field, α and β are constants, and I is the field emission current. The FN equation is useful to determine experimental changes in ϕ caused by the adsorption of species in the surface. Introducing Equation 5.1 into Equation 5.2 yields

$$I = \frac{CV^2}{\phi} exp(-\frac{D\phi^{\frac{3}{2}}}{V}) \tag{5.3}$$

where C and D are constants. Equation 5.3 can be rearranged to yield

$$\ln \frac{I}{V^2} = \ln \frac{C}{\phi} + \frac{D\phi^{\frac{3}{2}}}{V} \tag{5.4}$$

From Equation 5.4, changes in work function can be determined experimentally using the slope and y-intercept of a $\ln I/V^2$-$1/V$ plot. If ϕ for the pristine material is known, the ratio between both slopes (pristine and adsorbed) can be used to determine the change in ϕ.

5.2 Field ionization and desorption

In contrast to field emission, field ionization occurs when adsorbed molecules become ionized due to electrons tunneling from the adsorbate into the metal. At moderate electric fields, molecules in the gas phase become attracted to the metal by dipole forces. These gas phase molecules become field adosrbed into the metal at the more protuding positions. After adsoprtion, the adsorbates hop along the tip and may become ionized by electron tunneling into the metal (in positive fields) or from the metal (in negative fields). When ionization occurs, the adsorbate is accelerated towards the detector [216]. This process is depicted in inset a) of Figure 5.3. The potential energy diagrams illustrating field ionization under positive fields are shown in Figure 5.3. When no electric field is applied, the energy diagram is shown in inset b. The energy required to remove an electron from the atom is defined as the ionization potential (I_P). When an electric field F is applied, the barrier is bent as shown in inset c) of Figure 5.3 and electrons can tunnel into the metal.

The presence of tunneling will depend on how close the molecule is to the surface. If the molecule is too close to the surface, tunneling will not occur since the energy of the highest occupied orbital will be less that the Fermi level and no empty states will be available for tunnel-

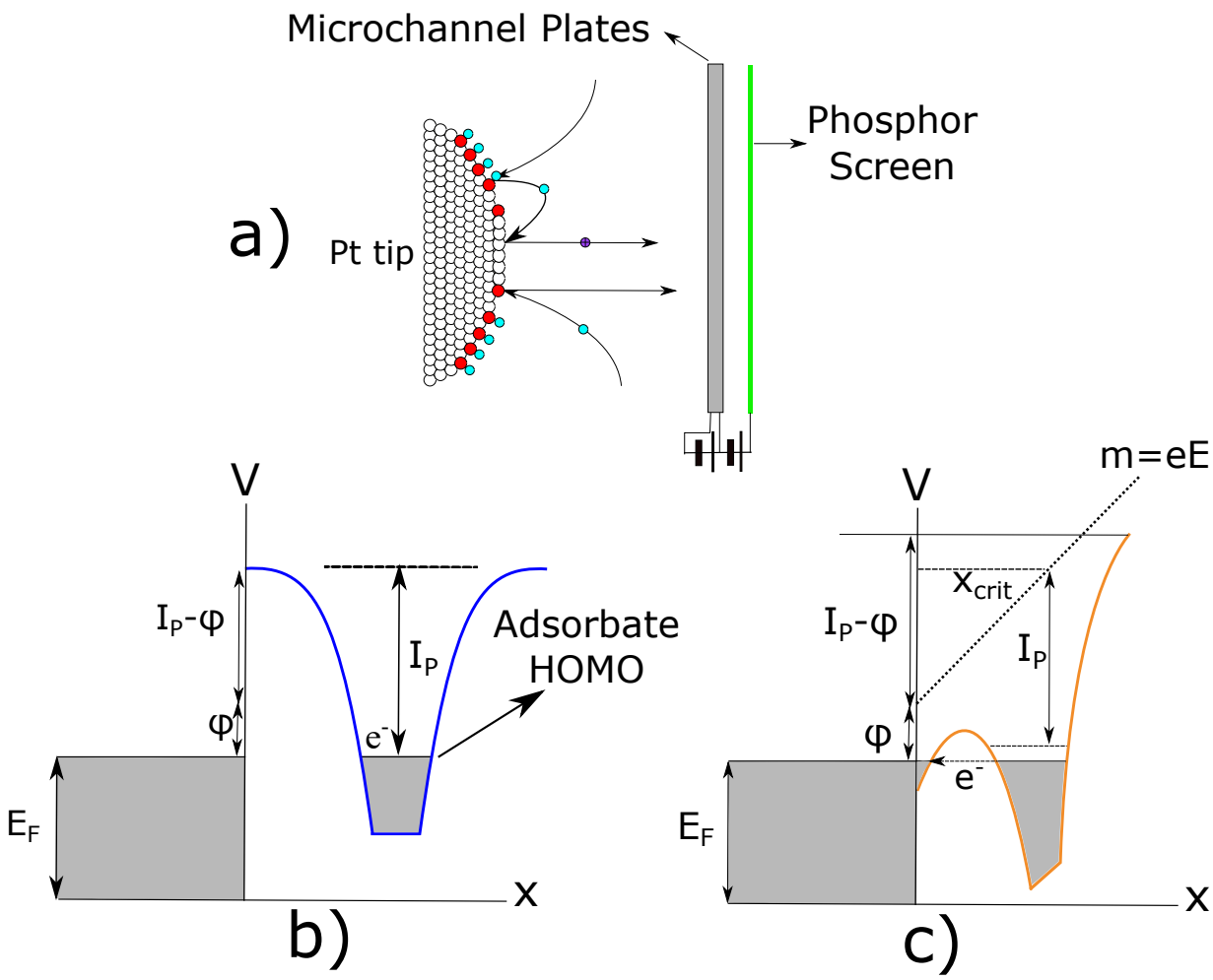

Figure 5.3: Depiction of field ionization barriers under a positive applied field. Inset a) depicts the mechanism for field ionization. Tip terrace sites are shown as white circles and step sites are shown as red circles. Neutral gas molecules are shown as light blue circles, while ionized adsorbates are depicted as dark purple circles. Insets b) and c) show the potential energy diagrams under the absence and presence of a field, respectively. The x-axis of both plots represents the distance from the surface, while the y-axis represents electron energy (adapted from [216]).

ing [218]. Tunneling can only occur at a distance known as the critical distance, given by Equation 5.5, where e is the charge of an electron.

$$x_{crit} = \frac{I_P - \phi}{eE} \tag{5.5}$$

If the barrier depicted in inset b) of Figure 5.3 is approximated as an equilateral triangle of width $(I - 2\sqrt{e^3E})$, where $2\sqrt{e^3E}$ is the Schottky barrier reduction by superposition of the Coulomb field and applied field, and a base width of $((I-\phi)/eE)$, the maximum tunneling probability is given by Equation 5.6 [216].

$$D(x_{crit}, E) = \exp(-0.683\sqrt{I - 7.59F^{1/2}}\frac{(I-\phi)}{E}) \tag{5.6}$$

5.3 FEM instrumentation

Field emission microscopes are among the simplest instruments for obtaining near-atomic resolution images of surfaces. The instrumentation for FEM and field ionization microscopes (FIM) is similar and will be described in this section. A FEM consists of a field emitter tip connected to a high voltage source and an anode coated with a fluorescent material. In FEM, a negative potential is applied to a field emitter tip under vacuum and the electrons emitted by the sample travel to the anode in vacuum. Pressures below 1×10^{-9} torr are required for FEM operation in order to reduce sample damage by sputtering [215, 219]. Most modern FEM instruments incorporate the use of microchannel plates (MCPs) to amplify the signal before reaching a fluorescent screen [216]. FEM provides a magnification factor of $10^5 - 10^6$. While FEM imaging can easily be done without MCPs, obtaining FIM images without MCPs can be challenging. Typically, this can be done by using light imaging gases such as H_2 or He and tip voltages in the order of 10 kV [216, 220], preferrably at cryogenic temperatures. When operating without microchannel plates, liquid hydrogen is typically used.

5.4 Field desorption

Field desorption occurs when surface atoms begin to evaporate as ions under an applied electric field. Two theoretical models have been developed to describe field desorption: the image-hump model [221] and the charge-exchange model [222]. The charge-exchange model treats field desorption as a transition between the atomic state (A+M), where A is the adsorbate and M is the metal to the ionic state ($A^{n+} + M^{n-}$). Under no applied field, the ionic state (subscript i) will have a higher energy (U_i) than the atomic state (U_a) by $\sum_i I_i - n\phi$. Under an applied field, U_a is slightly affected while U_i decreases significantly. For strong enough fields, $U_a = U_i$ at x_{crit}. For distances larger than x_{crit}, the ionic state will have lower energy, an atom can make an electronic transition to this state, and then be accelerated away from the surface [216]. The potential energy diagrams for this process are shown in insets a) and b) of Figure 5.4. Meanwhile, the image-hump model treats field evaporation as a thermal process where a metal ion of charge n+ has to overcome a barrier known as the Schottky saddle, where the barrier is a superposition of the applied field potential ($U_{field} = -neEx$) and the image potential ($U_{im} = -(ne)^2/4x$). In this case, the critical distance is given as x_s. The energy barrier is given by Equation 5.7, where Q_n is the barrier under an applied potential field, n is the charge of the ion, Q_0 is the barrier under no applied field, Λ is the heat of evaporation, and I_i is the ionization potential for the ith ionization step.

$$Q_n(E) = Q_0 - (ne)^{3/2}E^{1/2} = \Lambda + \sum_i I_i - n\phi \tag{5.7}$$

Under no applied field, the energy of the ionic state is given as $Q_0 - U_{im}$ and it is not defined for intermediate distances. When a field is applied, the barrier for the ionic state becomes distorted and reduced. A depiction of both potential energy diagrams is shown in insets c) and d) of Figure 5.4.

Field desoprtion can be used for detecting reaction products and reaction intermediates. In addition to adsorbates, surface lattice atoms can desorb under high fields. In this case, the phenomenon is known as field evaporation. Despite the difference in name, both field desoprtion and evaporation are described by the physical models explained previously [223]. Field evaporation

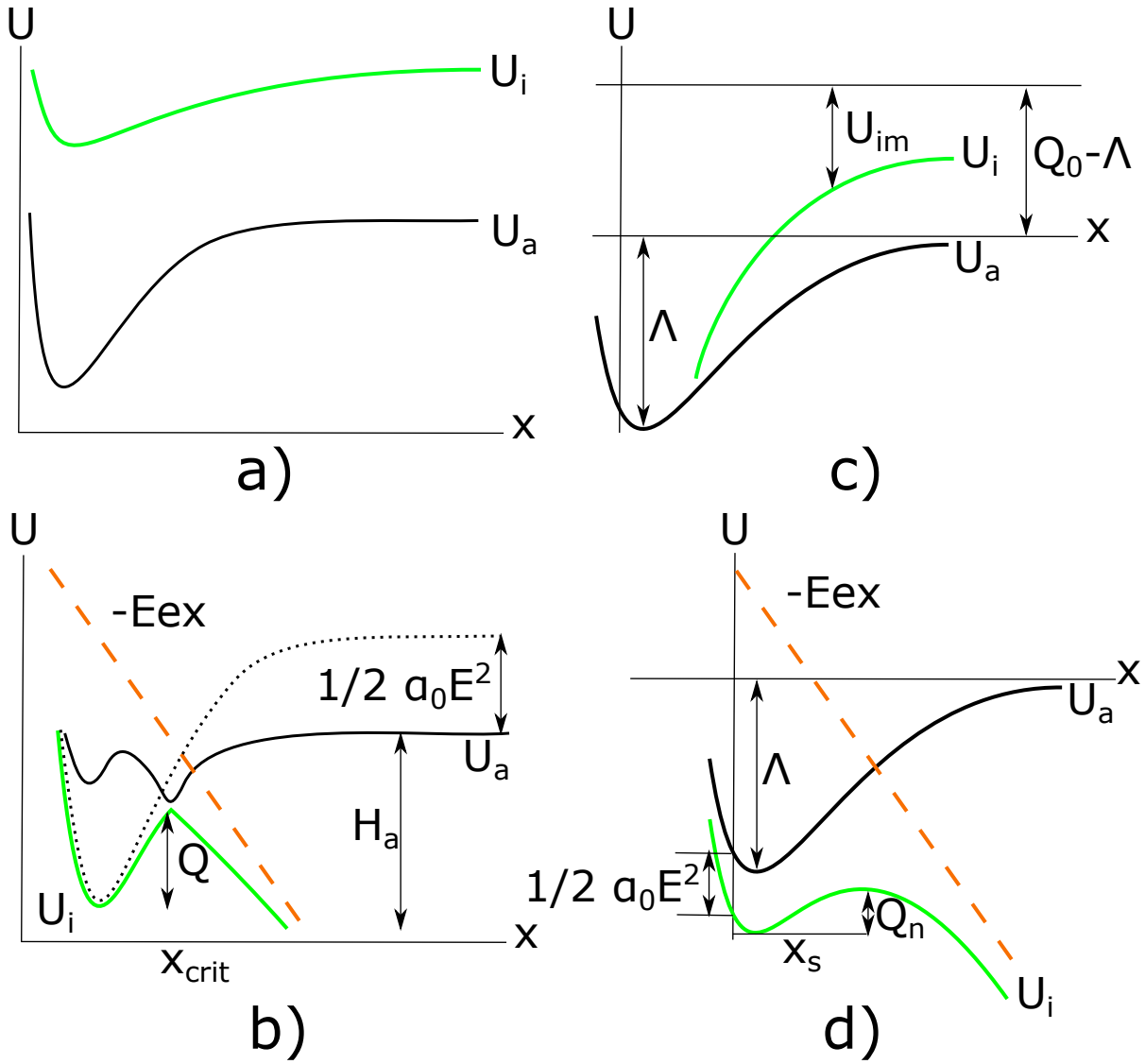

Figure 5.4: Energy diagrams for field desorption. Inset a) and b) depict the energy diagrams for the charge-exchange model, while insets c) and d) show the energy diagram for the image-hump model. Inset a) shows the curves under no field, while inset b) shows the effect of an applied field. In inset b), H_a is the heat of adsorption and Q is the activation energy for field desorption. The x-axis of both plots represents the distance from the surface, while the y-axis represents electron energy. Inset c) shows the curves under no applied field and inset d) shows the curves under an applied field. In all cases α_0 is the polarizability. Adapted from [222] and [216].

can be used for several applications such as cleaning field emitters. When a voltage is applied, the electric field will be higher on rough edges and protusions than on the smooth parts of the emitter surface, and the rougher parts will be field evaporated. This process can also be performed at low temperature to remove contaminants [216].

5.4.1 Li Field Desorption Microscope and Li Adsorption

An alternative to the use of an imaging gas involves field desorption of adsorbed Li in the tip as an imaging medium. In this case, Li is adsorbed at the shank of the tip and then diffuses to the apex of the tip. The resolution of the image is affected by the amount of Li layers adsorbed on the tip [224]. An image can be obtained due to differences in the energetics of field desorption based on the crystal planes on the surface and how adsorbates interact with the tip [225].

5.5 Ion spectrometry

One of the most important applications of field desorption involves studying surface reactions by applying fields to desorb any adsorbed species via ion spectrometry. In this section, two common methods of spectrometry and the instrumentation needed will be described: time-of-flight mass spectrometry (TOF-MS) and single ion detection via electromagnetic fields.

5.5.1 Time-of-flight mass spectrometry

Time-of-flight experiments involve the application of energy pulses seeking to impart all adsorbates in the surface with constant momentum. The ions then travel towards a detector. Pulses can be applied through the use of lasers (for heating the sample and desorbing reaction products) or via a counterelectrode (also known as pulse field desorption or PFD) in close proximity to the tip. The mass-to-charge ratio can be determined by Equation 5.8 [218].

$$\frac{m}{z} = 2eV_{tip}\left(\frac{t}{L}\right)^2 \tag{5.8}$$

where m/z is the mass-to-charge ratio, e is the charge of an electron, V_{tip} is the potential at which the ion formed, t is the time-of-flight, and L is the flight path length [226]. On PFD experiments, a series of pulses is used with a time delay between pulses. The time delay allows the reaction to occur and the reaction products can then be analyzed. Pulse widths on the order of 100 ns are used for desorption, while time delays between 1 μs and 1 s are used to cause desorption [227]. An increased flight path is preferred since it will increase the time gap between ions, allowing for improved resolution. This can be achieved by the use of an adjustable length drift tube with the detector being located at the end of the tube. The adjustable length drift tube allows to adjust the resolution by modifying the time-of-flight of ions as shown in Equation 5.8.

5.5.2 Single ion detection via electromagnetic fields

In addition to field pulses, an alternative desorption method involves steady changes in the desorption field. These changes can be achieved by applying a voltage ramp to a counterelectrode, analogous to temperature programmed desorption. In addition, single ion detection can be achieved through the application of perpendicular electric and magnetic fields using a Wien filter [228]. The fields are selected such that particles of a certain mass travel through the detector without deflection, while particles with other masses get deflected. A particle of mass m and energy eV_0, where e is the ion charge, will travel through the filter without deflection when the electrical and magnetic forces are equal. As shown in Equation 5.9, E_{Wien} is the magnitude of the applied electric field on the filter electrodes, B is the applied magnetic field on the filter, and v_x is the velocity of the ion along the x-axis, given in Equation 5.8 as $v = L/t$ [212, 213].

$$eE_{Wien} = ev_xB \tag{5.9}$$

Solving for v_x in Equation 5.8, substituting into Equation 5.9, and solving for B yields

$$B = E_{Wien}\sqrt{\frac{m}{2zeV_{tip}}} \tag{5.10}$$

A Wien filter is shown in Figure 5.5. The length of the filter is given as L_f and the length of the drift tube is given as L_d.

The total force on an ion travelling along the x-axis can be defined as shown in Equation 5.11 and its acceleration is given by Equation 5.12.

$$F_y = ze(E_{Wien} - vB) \tag{5.11}$$

$$a = \frac{ze(E_{Wien} - vB)}{m} \tag{5.12}$$

the velocity and positions of the ion can be given by Equations 5.13 and 5.14, where v is the velocity component at the y-axis, v_0 is the initial velocity on the y-axis, y_0 is the initial position in the y-axis, and y is the position.

$$v = \frac{ze(E_{Wien} - vB)}{m}t + v_0 \tag{5.13}$$

$$y = \frac{ze(E_{Wien} - vB)}{2m}t^2 + v_0 t + y_0 \tag{5.14}$$

The position and velocity of the ion at the end of the Wien filter can be determined by taking v_0 and y_0 to be zero and introducing $t = L_f/v_x$ where v_x is the x-component of the velocity. This yields

$$v(L_f) = \frac{ze(E_{Wien} - vB)L_f}{mv_x} \tag{5.15}$$

$$y(L_f) = \frac{ze(E_{Wien} - vB)}{2m}\left(\frac{L_f}{v_x}\right)^2 \tag{5.16}$$

The velocity and position in the y-axis at the end of the drift tube can be given by setting E and B to zero in Equation 5.14 and substituting $v(L_f) = v_0$ and $y(L_f) = y_0$. The travel time will be $t = L_d/v_x$ and v_x can be determined by Equation 5.8.

$$y(L) = v(L_f)t + y(L_f) = \frac{ze(E_{Wien} - vB)}{mv_x^2}\left(\frac{L_f^2}{2} + L_f L_d\right) \tag{5.17}$$

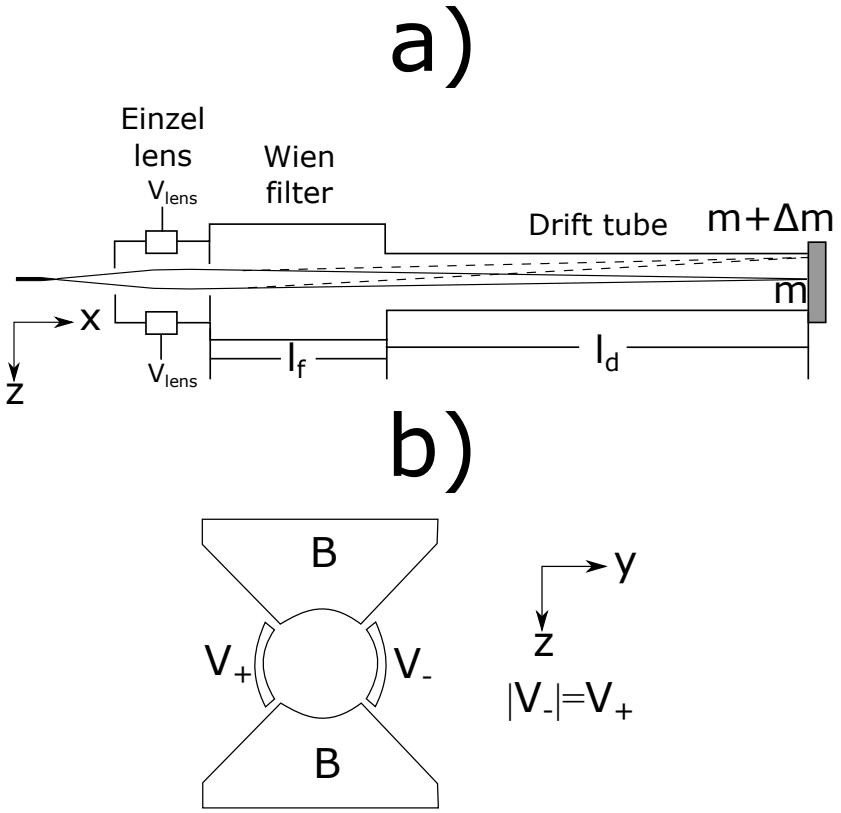

Figure 5.5: Schematic of a Wien filter. Inset a) depicts the operation mechanism of a Wien filter. Ions are accelerated from the tip towards an einzel lens for focusing. The ion beam then travels towards the filter, where ions of mass m (trajectory shown as a solid line) travel to the detector (shown as a grey rectangle) without deflection, while ions of mass $m+\delta m$ are deflected (trajectory shown as a dashed line). Inset b) shows a cross-sectional diagram of the Wien filter used in this work. A magnetic field B is applied along the z-axis, while an electric field is applied along the y-axis. In addition to ion selection, the curved electrodes and magnetic poles provide additional focusing [228]. Adapted from Pinkerton [213].

For an ion with kinetic energy equal to the tip potential, v_x can be substituted by Equation 5.8 to yield

$$y(L) = \frac{1}{2V_0}\Big(E_{Wien} - \sqrt{\frac{2zeV_{tip}}{m}}B)\Big(\frac{L_f^2}{2} + L_f L_d\Big) \tag{5.18}$$

5.6 Application of field ionization and desorption to study chemical reactions

Field ionization experiments are useful for providing thermodynamic and kinetic information about catalytic systems [229]. In this section, the application of field ionization will be described using water ionization on platinum field emitters.

5.6.1 Water ionization

The behavior of water in metals under electric fields has been studied due to its relevance in electrochemical systems, its polar nature, and the multiple forces involved. The electric fields in electrochemical interfaces have a high enough mangitude (on the order of several V/Å) that they can induce changes in the adsorption energy and orientation, distort molecules, induce ionization, and significantly affect interfacial chemistry. Among metals, platinum has attracted significant interest due to its ability to assist spontaneous formation of hydronium ions because of its high electron affinity. This process is depicted Equation 5.19, where m is the number of molecules present in a solvation cluster $H^+(H_2O)_m$ [230].

$$(H_2O)_{m,ads} + H_{ads} \longrightarrow H^+(H_2O)_{m,ads} + e^- \tag{5.19}$$

Ramped field desorption (RFD) experiments have shown that the field required to start ionization is linearly proportional to the thickness of the adsorbed water layer with 2 regimes: a low thickness regime and a large thickness regime with a larger slope. FIM experiments showed that thin layer ionization was uniform and randomly distributed, while thick layers showed evenly spaced ionization hotspots. A graphical representation of these phenomena is shown in Figure 5.6. In addition, the onset field of ionization is linearly dependent on temperature in agreement with a

charge-exchange model. Such observations can be attributed to dielectric screening and the ionization interface. The electric field distribution in both scenarios presents 2 maxima at the water-tip and water-vacuum interfaces. In thin layers, the global maximum occurs at the water-vacuum interface and ionization occurs at this interface. Meanwhile, ionization in thick layers occurs at the water-tip interface [231]. In a thin layer, the potential is uniform within the water layer and decreases exponentially in vaccum. For thick layers, the potential profile drops rapidly near the tip surface, becomes constant in an intermediate region where water can screen the field, and finally drops exponentially beyond the water-vacuum interface [232].

Mass-selected RFD experiments have shown that solvation clusters of m up to 7 have been observed at low fields with decreasing size as the electric field is increased. The onset of ionization for the m-1 cluster occurred at the emission peak for the m size cluster due to kinetic limitations in the emission of larger clusters caused by solvation effects. Temperature cycling experiments further showed that the emission process is thermally deactivated due to the observed Arrhenius dependence of the ion signal [234]. Figure 5.7 shows mass-selected RFD spectra for different water cluster sizes, as well as temperature cycling spectra. The temperature cycling spectra show a steady ion signal, followed by a decay as temperature increases. The decay in ion signal does not show an Arrehnius dependence, indicating that the process is thermally deactivated. In addition, there is a continuity in the decay of the ion signal from one cluster to another as temperature increases. FIM experiments at different electric fields revealed the presence of long-lived, self-sustained emission hotspots at lower desoprtion fields and uniform emission at high fields, supporting a hump formation mechanism. Dissociative ionization occurs at the water-vacuum interface when proper solvation can screen the proton charge. After dissociation occurs, the hydroxyl group migrates towards the tip and discharges, while the proton remains until the field is high enough for emission. As the ion cluster pulls away from the interface, it pulls water molecules towards the charge and a water hump forms as the ion is emitted. Any remaining water molecules are left in a state that leads to further emission events [235].

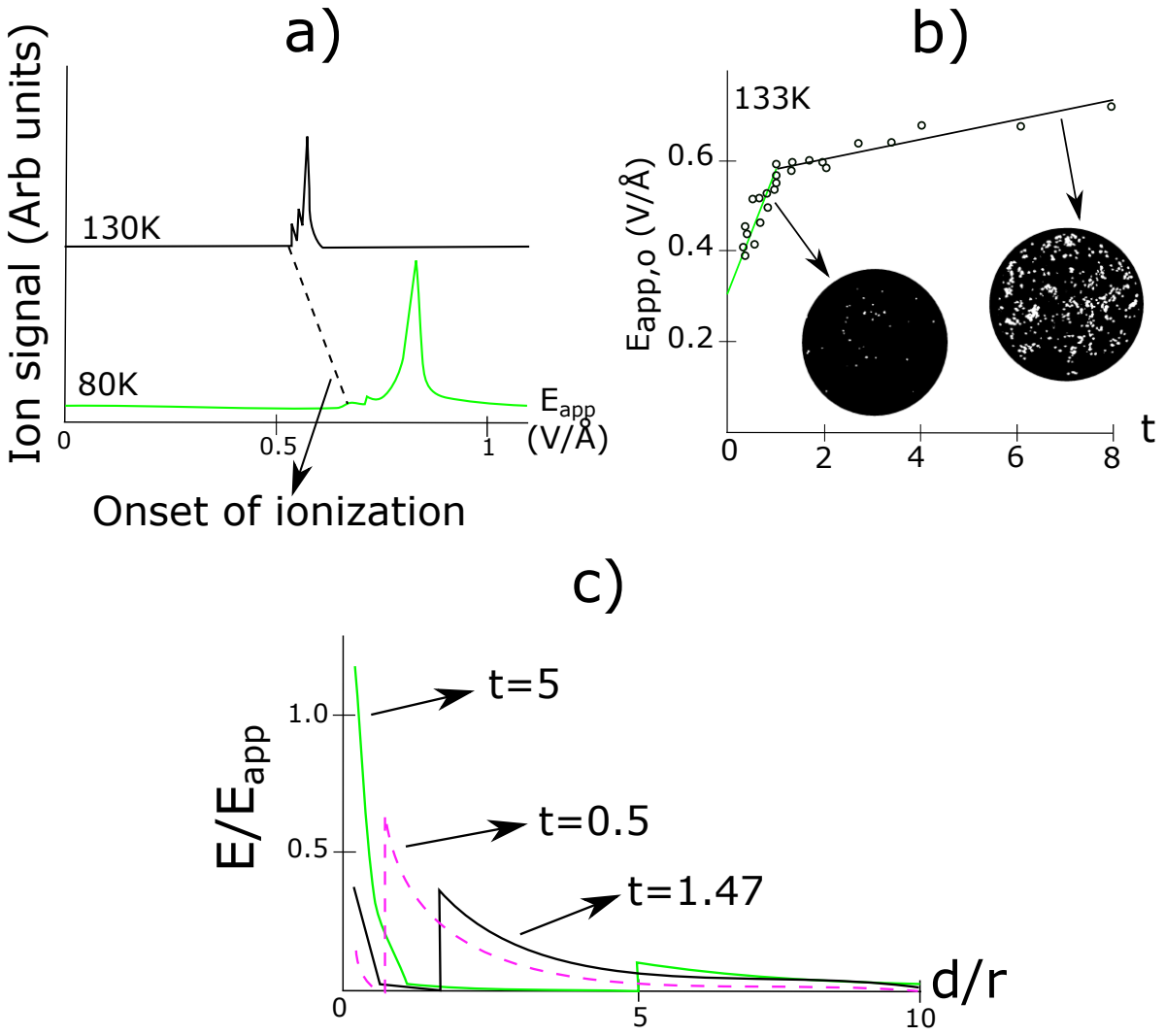

Figure 5.6: RFD experimental results for water ionization in thin and thick ice layers. Inset a) shows a typical RFD spectra for thin water layers, with an arrow indicating the onset of ionization (adapted from [231]). Inset b) shows the onset of ionization field dependence as a function of layer thickness, with arrows pointing to sample FIM images for thin and thick films, respectively (adapted from [233]). Inset c) shows the electric field distributions for water layers of different thickness. In all cases, the layer thickness $t = t_w/r$, where t_w is the thickness of the water layer in Å and r is the tip radius (adapted from [232]).

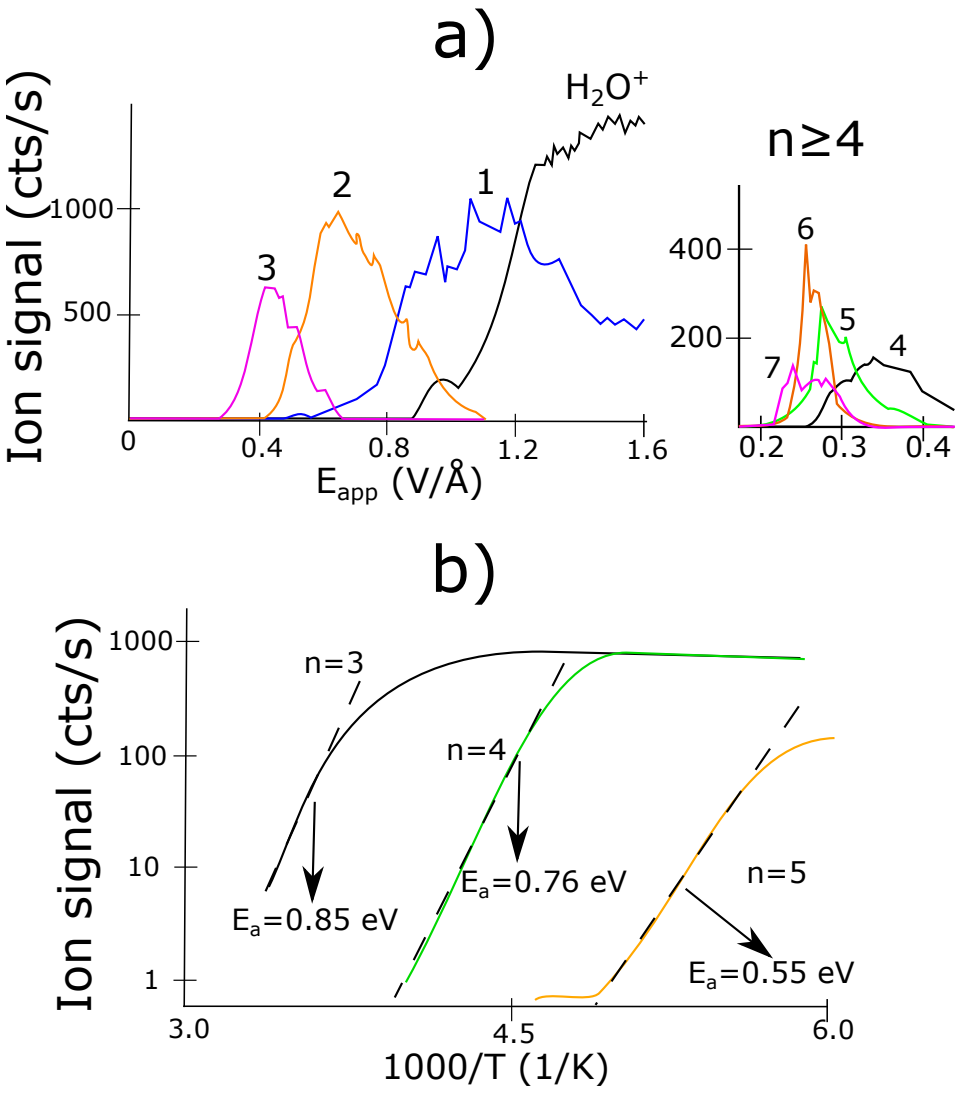

Figure 5.7: Mass-selected field desorption experiments on ice layers. Inset a) shows a set of mass-selected RFD spectra, with the cluster size indicated as the number above the peak emission for each spectrum. Inset b) shows temperature cycling experiments for different cluster sizes. Adapted from [234].

5.6.2 Water-methanol ionization

Water is rarely present in isolation in relevant electrochemical systems and it is important to understand how it affects electrochemical reactions. For example, methanol-water coadsorption is relevant due to interest in methanol fuel cells. A typical water-methanol PFD spectrum is shown in inset a) Figure 5.8. PFD experiments show the presence of a time delay in the emission of clusters with mass grater than 55 amu (peaks larger than $H^+(H_2O)_3$). Such experiments also showed a complex effect on adlayer composition. $H^+(H_2O)_n$ emission increased monotonically for n>2 as a function of increasing H_2O, while $H^+(H_2O)$ exhibited an emission maximum. Meanwhile, $H^+(CH_3OH)_m$ emission decreased monotonically as the H_2O fraction increased. Such dependences are shown in inset b) of Figure 5.8. Other fragments observed in the experiments include CH_3^+, H_2CO^+, H_3CO^+, O_2^+, $H_3O_2^+$ (attributed to methanol dissocation), and CH_3OH^+. These observations were attributed to a two-step mechanism involving cluster growth followed by emission. The presence or absence of certain peaks is dependent to the relative rates of each step and their dependence on electric field. For example, cluster growth is favored at low fields while direct emission is preferred at high fields [236].

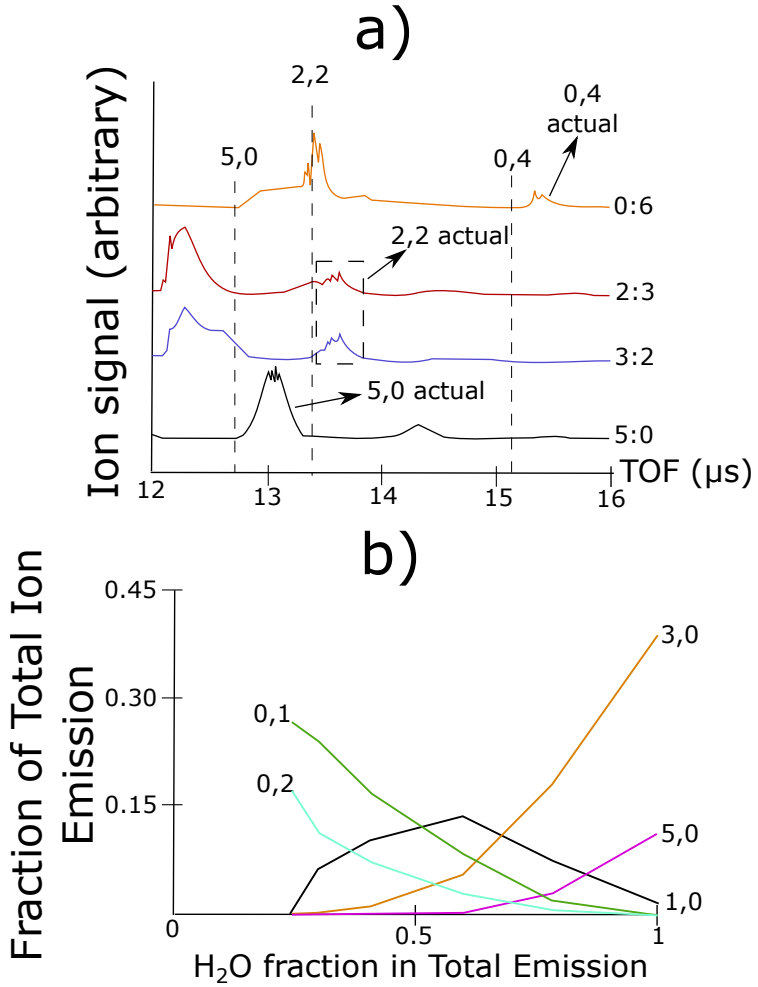

Figure 5.8: PFD spectra for water-methanol adlayers. In both figures, the notation [i,j] represents the number of water (i) or methanol molecules (j) in a given cluster. Meanwhile, the notation k:l indicates the partial pressure of each species ($\times 10^{-6}$ torr), where k is the partial pressure of water and l is the partial pressure of methanol. Inset a) shows a sample PFD spectrum for a water-methanol adlayer. Any phenomenon that occurs after the application of the field is depicted as a hump, while emission of ions formed before pulse application is observed as a sharp peak. The expected time of filght (TOF) for a given cluster is shown as a dashed line and the actual time of arrival is shown with an arrow pointing at a given peak. Inset b) shows the water and methanol cluster distributions as a function of water content in the adlayer. Adapted from [236].

Chapter 6

EXPERIMENTAL METHODS

6.1 Introduction

The original goal of my research involved characterizing Li-O_2 battery reactions using field ionization techniques with a field ionization microscope (FIM). Construction of the FIM used in this project was completed in 1999. However, the instrument was not in use since 2006 and significant upgrades were required. Testing was performed to ensure proper function. However, due to funding constraints, the project was terminated in June 2018, before full function of the instrument was achieved. This chapter describes general experimental procedures for operating the FIM, as well as results for the tests that were completed. In addition, a section describes improvements that need to be done to the instrument to ensure proper functioning. For more details on operation procedures and electronic schematics, refer to Appendices A and B.

6.2 Experimental setup and protocols

All experiments were performed in a UHV system equipped with an imaging detector, a Wien filter, and a TOF spectrometer. A schematic of the system is shown in Figure 6.1 and a detailed description of the instrument is provided in Section 6.2.2. The chamber was pumped down by a turbo-molecular pump and a titanium sublimation pump, allowing to reach a base presure of 10^{-10} torr.

6.2.1 Sample making

Platinum tips were prepared following the beaker method of electropolishing outlined by Scovell [218] and Tsong [216]. In this method, the tip was dipped in an electrolyte solution and a positive bias is applied between the tip and a counter electrode. The electrolyte solution consisted of 4:1

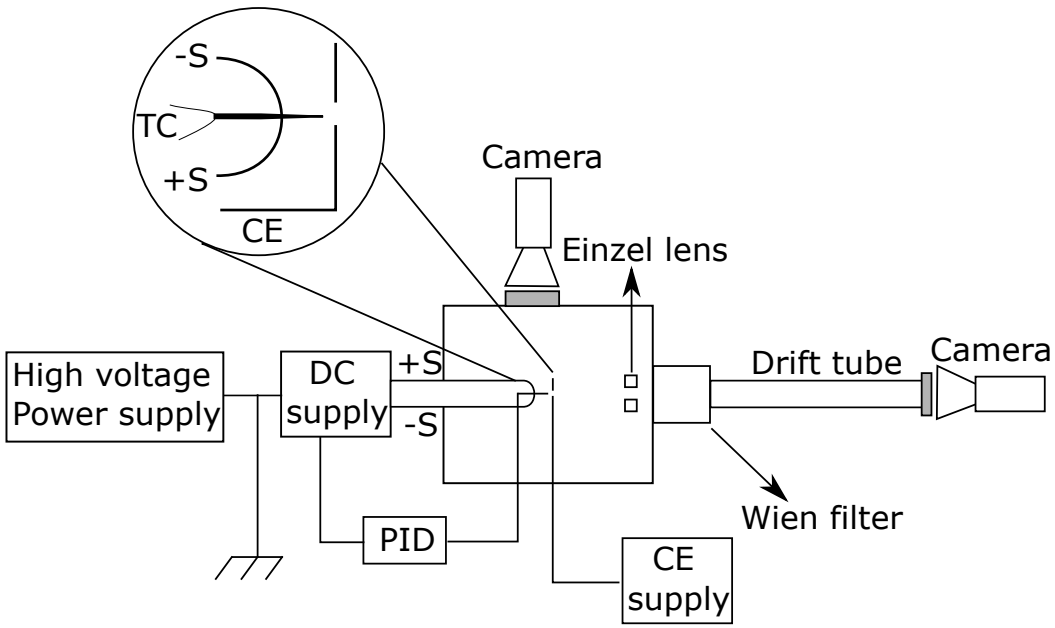

Figure 6.1: Schematic of the UHV chamber. The sample is heated by applying a current through the heating loop connected to terminals +S and -S. Meanwhile, temperature is monitored using thermocouple TC. The system allows two operation modes: a spectrometry mode and a microscopy mode. In spectrometry mode, the tip is directed towards the drift tube. In microscopy mode, the tip is directed towards the other detector (represented as a gray rectangle).

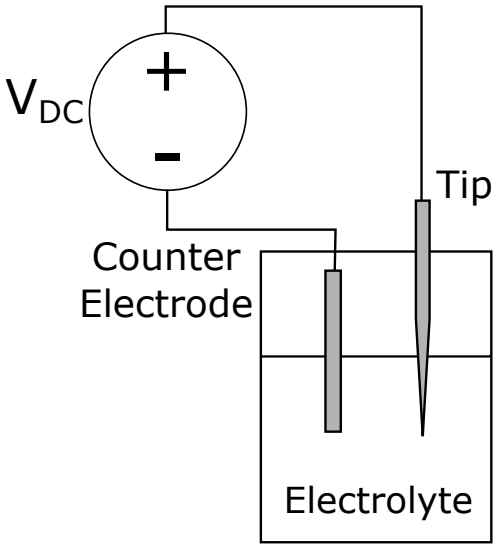

Figure 6.2: Schematic of the beaker method of electropolishing. Tip etching occurs at a voltage V_{DC}, as described in Section 6.2.1.

by weight molten $NaNO_3$:NaCl electrolyte heated to a temperature of 500 °C. Electrochemical etching was performed by applying a positive potential of approximately 2 V DC for up to 30 s. A schematic of the method is shown in Figure 6.2. Further tip refinement can be achieved by applying voltage pulses, decreasing the voltage, or increasing the immersion time. Tips with longer tapers are desired due to reduced blunting. All tips were made using 0.127 mm platinum wire. After etching, the tips were characterized using both optical and scanning electron microscopy (SEM) to determine tip sharpness.

An SEM image of a tip is shown in Figure 6.3. Tips with radii on the order of 50 nm can be achieved using the beaker method. However, care must be taken to avoid curling tips during etching or characterization.

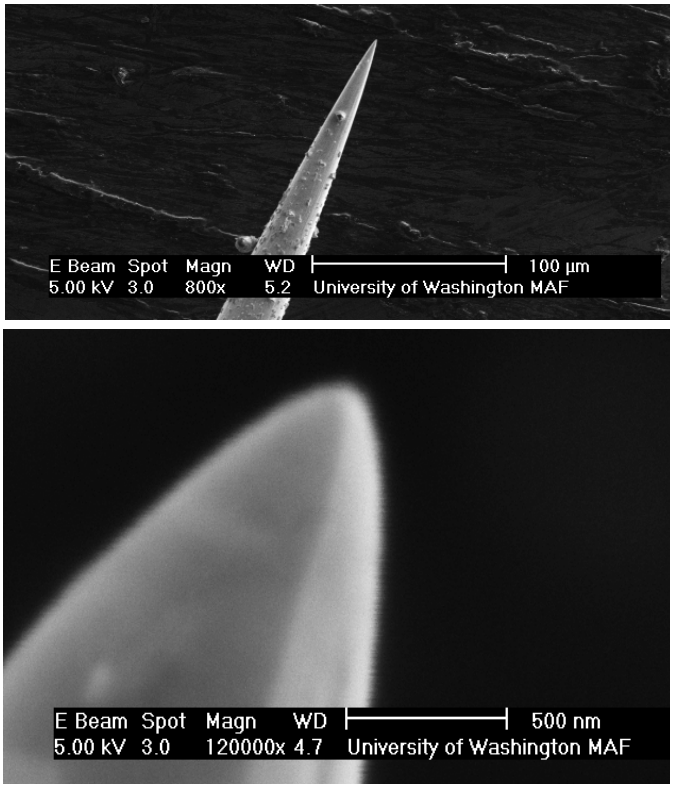

Figure 6.3: SEM image of a field emitter tip. Tip etching occurs at a voltage V_{DC}, as described in Section 6.2.1.

6.2.2 UHV chamber

The sample and imaging detectors were contained in the UHV chamber. Before introducing the sample into the chamber, the tip was spot welded to a 0.25 mm diameter platinum wire heating loop. A 0.08 mm chromel-alumel thermocouple wire was spot welded into the non-polished end of the sample to allow for temperature measurements. The sample was mounted in a holder containing a counter electrode plate and a cooling tube. The holder allowed for rotation of the sample to face the imaging detector or the TOF spectrometer, as shown in Figure 6.1.

The sample temperature was controlled by resistively heating the sample using a power supply (Agilent 6265) floated to the tip potential. The power supply was contained inside of an isolation box and controlled remotely through the use of a voltage-to-frequency isolation card system. The isolation box has 4 isolation channels used to control both the power supply voltage and curent, temperature acquisition, and emission current acquisition. Each channel consists of 2 cards: a voltage-to frequency card and a frequency-to voltage card connected via fiber optic cables. A DC voltage signal is introduced in the voltage-to-frequency channel and converted to a frequency by a voltage-to-frequency converter (Analog Instruments, AD652BQ). The converters take a voltage signal ranging from 0 to 10 V and convert it to a pulse train triggered between 0 Hz and a clock frequency (2 MHz), set by a clock circuit. The resulting pulse train is transmitted to the frequency-to-voltage card via a fiber optic cable. At the frequency-to-voltage card, a voltage-to-frequency converter (AD652BQ) is used to convert the pulse train to a voltage. The isolation channel design requires a card referenced to the tip potential and a card referenced to ground. In the power supply voltage and current control channels, the frequency-to-voltage card is floated to the tip potential. Meanwhile, the voltage-to-frequency cards are floated to the tip potential in the temperature and emission current channels. For more details on the construction of the box, refer to reference [213]. A detailed description of the isolation box and schematics are provided in Appendix A.

6.2.3 Imaging

Imaging was performed under two operation modes: FEM and FIM. Prior to imaging, the tip was cleaned by flashing to 500 K, followed by field evaporation of a small amount of Pt to remove any strongly bound adsorbates, as well as ensuring that the surface is atomically clean and regular. Changes in the work function upon adsorption were determined using the FEM operation mode with the procedure outlined in Section 5.1.1 in the Appendix. The imaging detector was placed 4 cm away from the tip. Ions or electrons emitted from the tip were projected onto chevron microchannel plates (Galileo) and then directed into phosphor screens. The image was then recorded using a CCD camera, an H.264 encoder (BlackMagic Design), and a computer. Electronic detection of emission from the tip was possible with the use of a capacitively coupled pre-amplifier (Advanced Research COMBO-100) and rate meter (Ortec 449) .

6.3 Results

6.3.1 Tip imaging

As described previously, the tip was imaged using both FEM and FIM. In FEM, the tip is directed towards the detector and a negative voltage is applied until an image appears on the detector. A FEM image of a sample is shown in Figure 6.4.

In addition to FEM, FIM was performed at liquid nitrogen temperatures using Ne as an imaging gas. A sample FIM image is shown in Figure 6.5. The micrograph shown in inset b) was taken using a lower voltage in both the MCP and phosphor screen detectors and therefore, it does not show the same contrast as that shown in inset a). The FIM micrograph shows the presence of terraces, indicated by arrows in the figure. After flashing the tip, several adsorbates were removed, as it can be seen by the decrease in emission hotspots. In addition to that, adsorbate surface diffusion was observed, as shown in inset c) of Figure 6.5. The frame labelled "before" shows an adsorbate indicated with a blue arrow that hops to a contiguous site, as seen in a frame taken 2 s after.

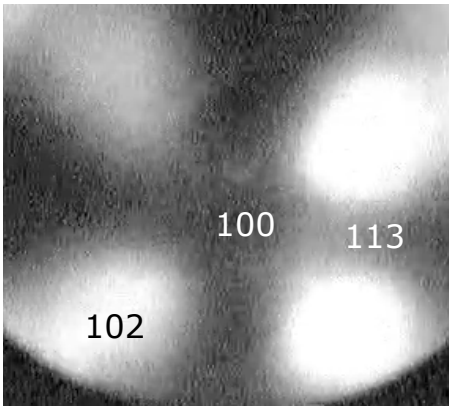

Figure 6.4: FEM image of a Pt field emitter. The crystal facets are labelled in the image.

6.4 Field desorption

Field desorption experiments are performed in both pulsed and continuous field desorption modes. Before the experiments, the reagents of interest are dosed under zero field conditions, where the tip and the counter electrode are held at the same potential. The ion beam is then directed to a single electrostatic lens (einzel lens) for focusing [237], with the lens set to a potential of 0.73 V_{tip} [213]. The end of the drift tube is equipped with a BVS-1 MCP assembly with a phosphor screen (Colutron Research). Due to the small magnitude of the electron signal, a capacitively coupled preamplifier-discriminator (Advanced Research COMBO-100 with MF-100PS power supply) is used. Deetection is done using a rate meter (Ortec 449) for continuous ion detection or a picosecond time analyzer (Ortec 9308) for pulsing experiments. Three modes of ion detection are possible: general rate of emission, time-of-flight, or signal integration.

6.4.0.1 Continuous field desorption

Continuous field desorption experiments can be performed using a ramped field desorption (RFD) procedure. In RFD, the counter electrode voltage is changed at a constant rate (typically 10 V/s) starting at the tip potential until its value reaches zero. In this case, the pre-amplifier signal is

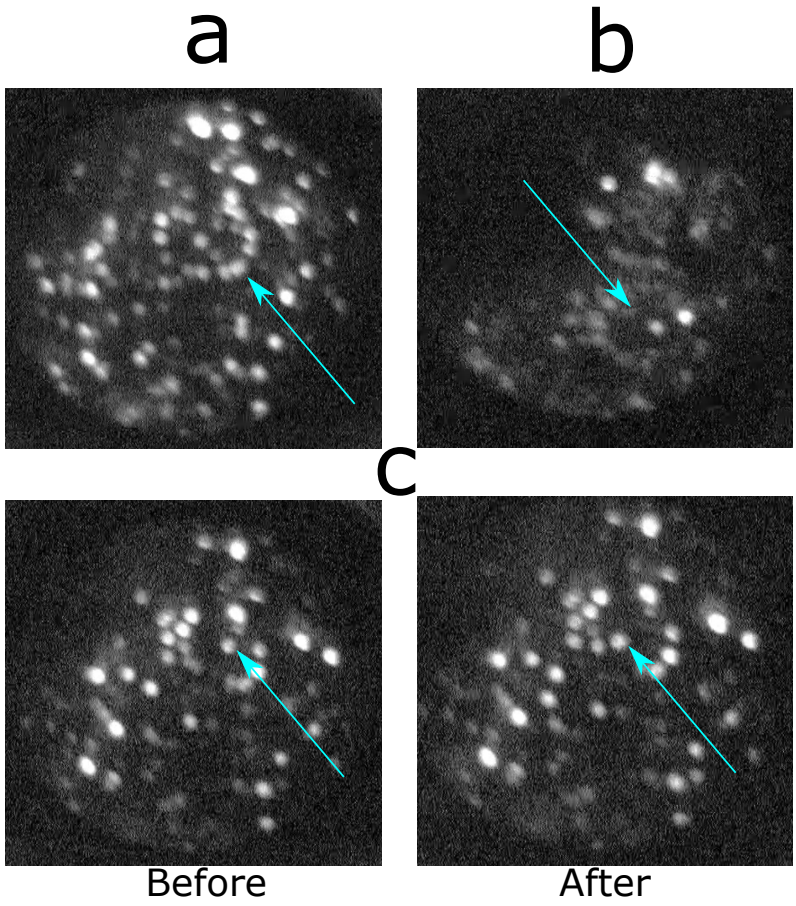

Figure 6.5: FIM image of a Pt field emitter taken using Ne (2×10^{-4} torr) as the imaging gas. Inset a) shows a FIM micrograph of a tip prior to flashing at 500 K, while inset b) shows a micrograph after flashing. The atoms or features of interest are indicated by light blue arrows.

recorded using two rate meters. One rate meter is set to capture the full spectrum, while the other will be set to a smaller range in order to determine the onset of ionization. A schematic of a RFD experiment is shown in Figure 6.6.

Mass-selected RFD experiments are performed using a home-made Wien filter. The electric field is set by applying a symmetric voltage across both electrodes with $|V_-| = V_+$, where V_- is the voltage on the negative electrode and V_+ is the voltage on the positive electrode, as shown in Figure 5.5. The magnetic field is provided using an electromagnet placed between two metal plates. The electric field, B, in Gauss, was calculated using Equation 6.1, where i is the coil current in Amperes [213].

$$B = 1414\ i \tag{6.1}$$

Wien filter voltage can be determined using Equation 6.2, where V_0 is the applied potential across the Wien filter electrodes and d is the separation between the electrodes in the filter (12.89 mm).

$$V_0 = 0.141\ i\ d\ \sqrt{\frac{2eV_{tip}}{m_0}} \tag{6.2}$$

The separation between the clossest masses in a spectrum can be determined using Equation 6.3, where m is the closest mass to the mass of interest m_0.

$$\Delta x = 0.1414\ i\ \sqrt{\frac{e}{2V_0}}\left[\frac{L_f^2}{2} + L_f L_d\right]\left(\sqrt{\frac{1}{m_0}} - \sqrt{\frac{1}{m}}\right) \tag{6.3}$$

The filter used in the FIM has a L_f value of 101.6 mm and L_d of 600 mm. For such values, Equation 6.3 becomes

$$\Delta x = 2046.68\frac{i}{\sqrt{V_0}}\left(\sqrt{\frac{1}{m_0}} - \sqrt{\frac{1}{m}}\right) \tag{6.4}$$

Note that Δx and V_0 in Equation 6.4 are in mm and kV, respectively. The magnet settings are chosen by adjusting the magnet current that yields the smallest E_0 that provides a Δx value of at least 9 mm, which corresponds to the detector radius.

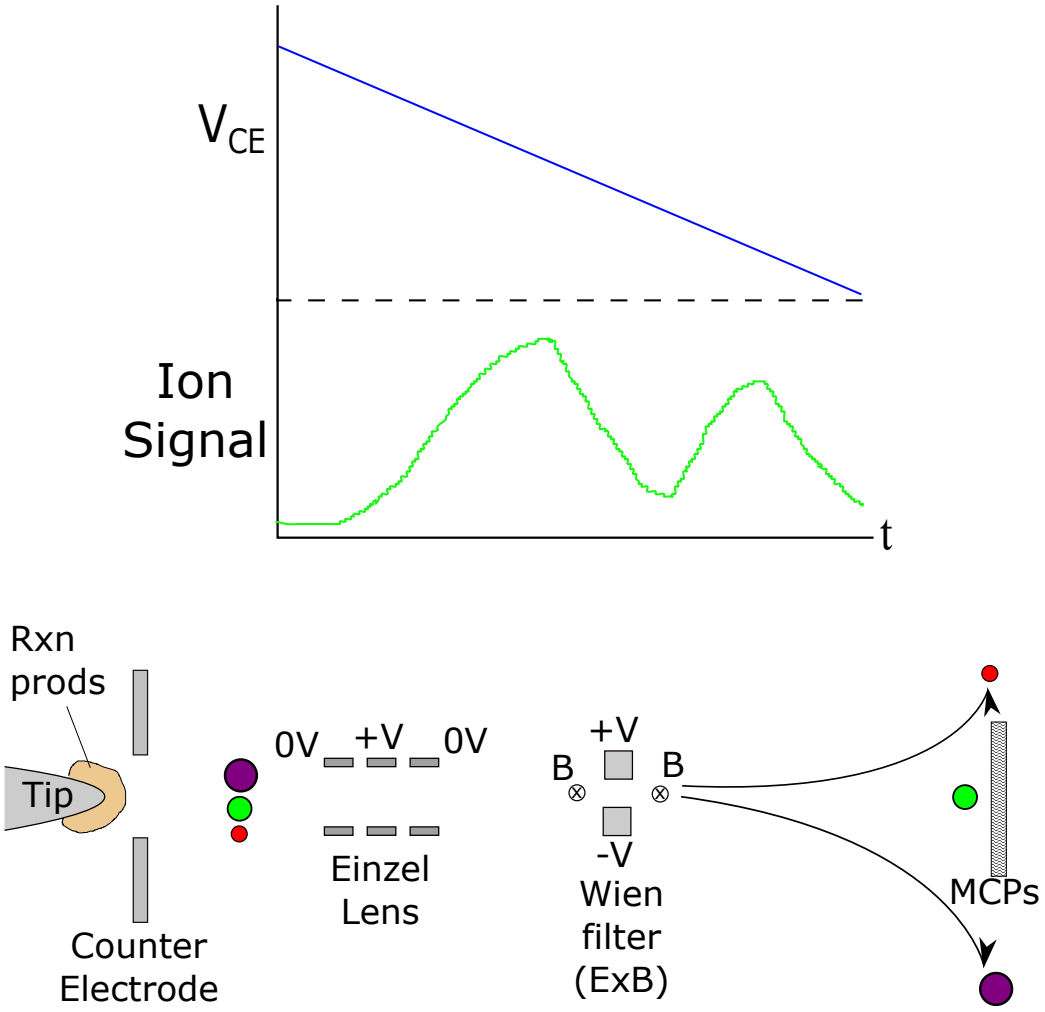

Figure 6.6: Schematic of a RFD experiment. The bottom inset depicts desorption from the tip, ion beam focusing using an Einzel lens with the corresponding field lines shown as curves connecting the electrodes, and mass-selection via a Wien filter to achieve detection of the green, medium-sized circles. The plot shows both the counterelectrode potential (upper inset) and the corresponding ion signal (lower inset) for the green ions.

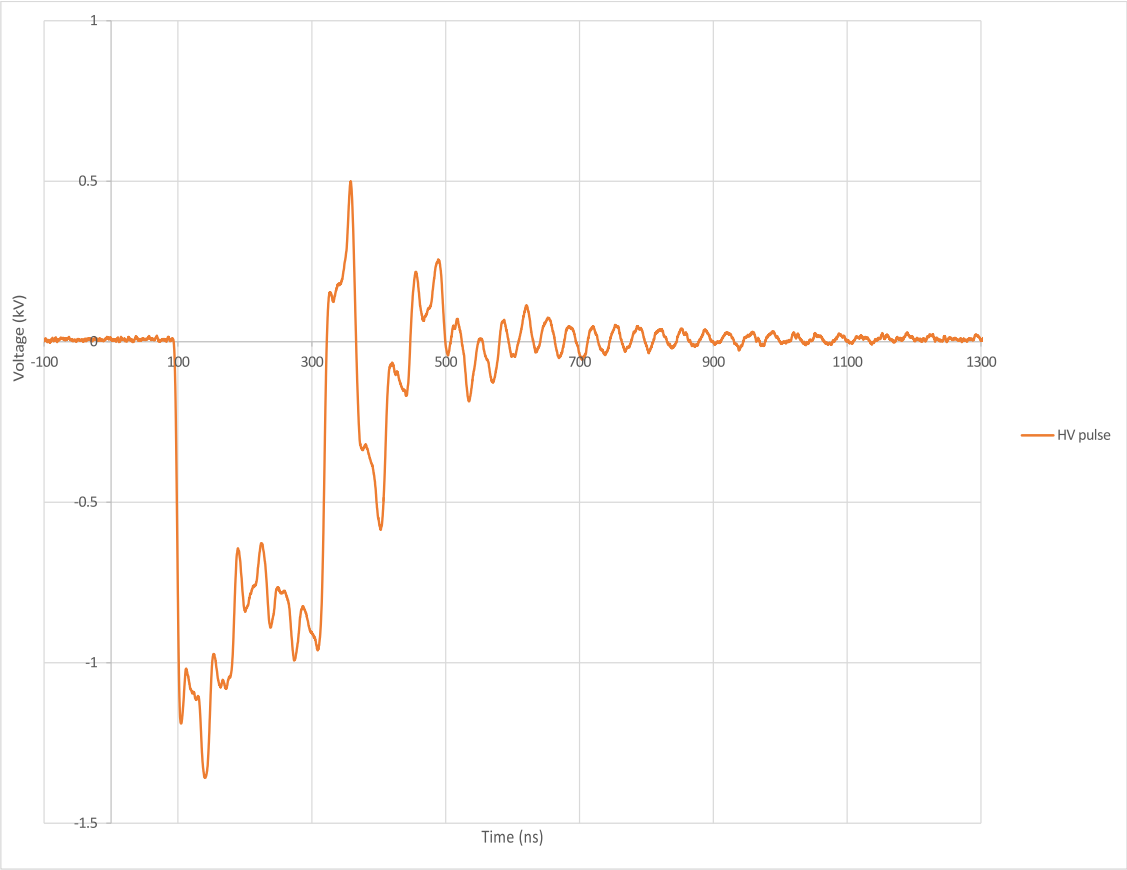

Figure 6.7: Sample high voltage pulse measured at the end of the counterelectrode plate. The applied pulse has a magintude of -900 V.

6.4.0.2 Pulsed field desorption

PFD experiments are performed by applying voltage pulses at the counter electrode. Following adsorption, a base field is applied such that no ion signal is produced with such a base field. In experiments with a positive tip potential, this implies that $V_{tip}>V_{CE}$. A train of square pulses is then applied to the counterelectrode plate. Pulses of up to 6000 V with repetition frequencies ranging between 10 Hz and 10 kHz can be applied using commercially available pulse generators. A sample pulse is shown in Figure 6.7.

Experiments can be performed both using a positive and a negative tip voltage, where negative pulses are used in the positive tip potential experiments and positive pulses are used in the negative tip potential experiments. A schematic of a PFD experiment is shown in Figure 6.8.

Due to the low signal intensity, data acquisition is performed in time bins for a certain period of time per pulse in one pass. Data is collected and added in each bin for multiple passes, typically ranging between 1000 and 10000 passes. Kinetic information can be obtained by varying the pulse repetition frequency, experiment temperature and applied base field. A schematic of this procedure is shown in Figure 6.9. PFD experiments are performed as a function of reaction time t_r, temperature, and applied field F_{rxn}. Relative rates of formation can be obtained by plotting the ion signal for each species as a function of reaction time. Activation energies can be obtained using an Arrhenius plot of the ion signal. Finally, changes in the dipole moment and polarizability can be obtained by plotting activation energy vs reaction field [238]. The activation energy has the form shown in Equation 6.5, where Q(E) is the field-dependent activation energy, $V(x_c)$ is the potential energy at the critical distance, H_a is the field-free activation barrier, P is the dipole moment, and α is the polarizability. The Δ term for both P and α indicates a difference between the initial and final states, as shown in Figure 5.3.

$$Q(E) = V(x_c) + H_a - (\Delta P)E - \frac{1}{2}(\Delta\alpha)E^2 \tag{6.5}$$

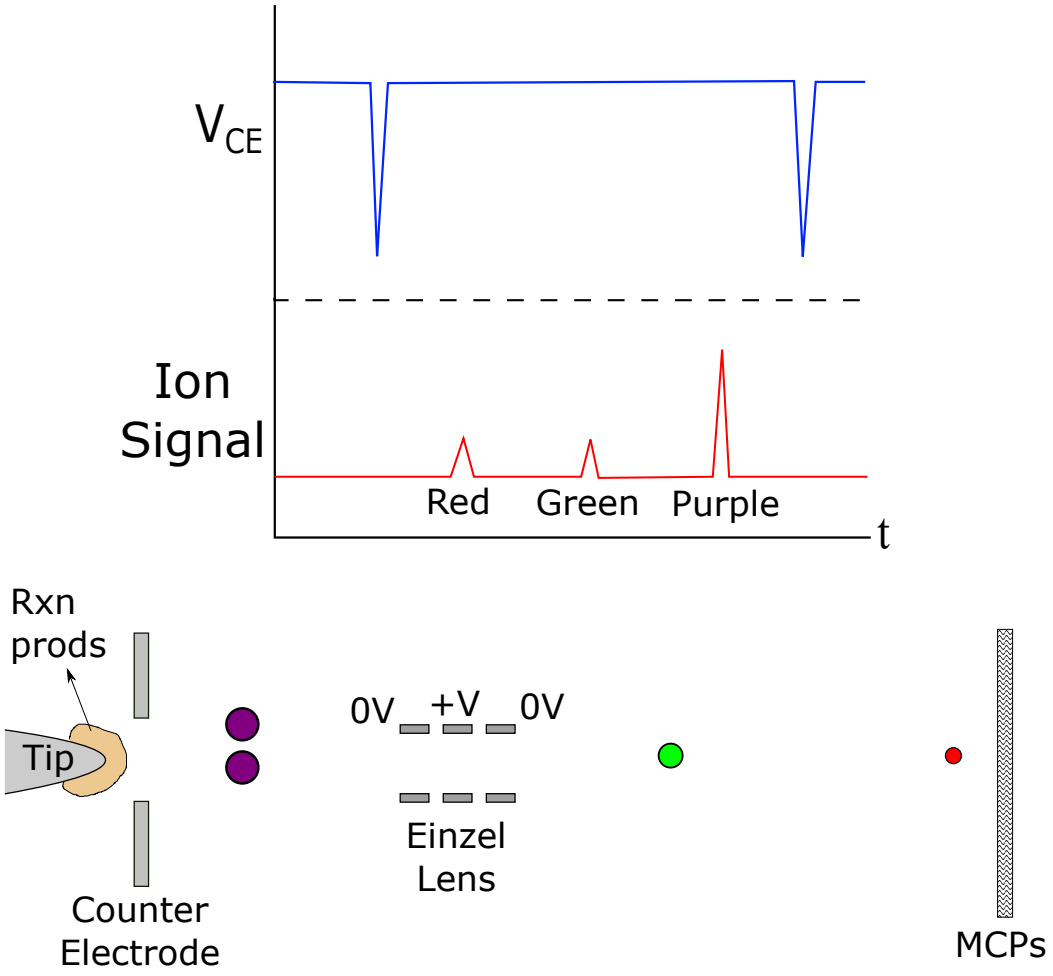

Figure 6.8: Schematic of a PFD experiment. The bottom inset shows ions of different masses emitted from the tip travelling towards the detector, shown as red, green, and purple circles. The Einzel lens is depicted as a set of gray rectangles. The plot shows both the counterelectrode potential (upper inset) and the ion signal (lower inset) as a function of time. The ion signal plot shows labels indicating the peaks corresponding to each ion (red, green, or purple, respectively).

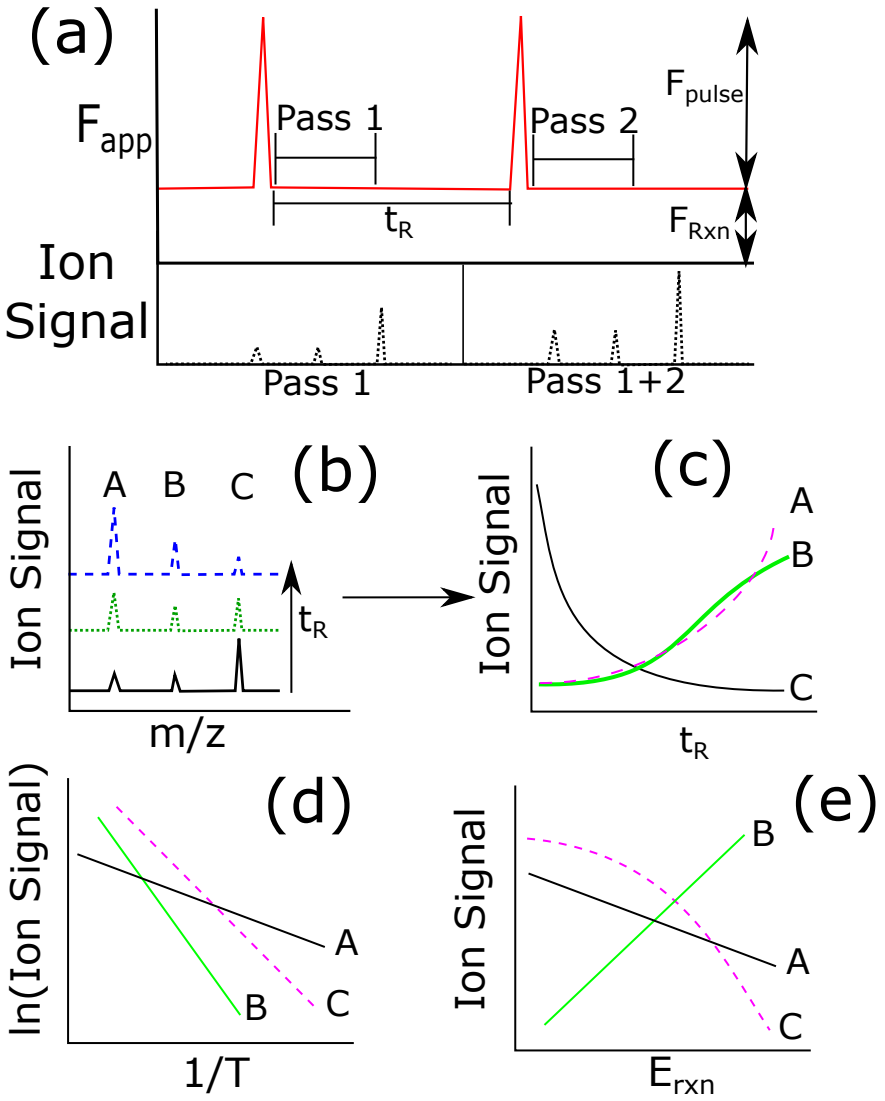

Figure 6.9: PFD data analysis. Inset a) shows the procedure for data acquisition, with the applied field pulses shown in red and the experimental observations shown as black points. Meanwhile, inset b) shows the procedure for obtaining kinetic information such as activation energies and the relative rates of formation of species.

Chapter 7

FIELD IONIZATION USAGE FOR ALKALI METAL-O_2 CHARACTERIZATION

Despite its limited use and availability, field ionization techniques can provide useful information regarding discharge and charge mechanisms in alkali metal-O_2 batteries. Such information is necessary to develop better strategies for electrode designs that could improve battery performance. This chapter proposes experimental frameworks that can be used to characterize alkali metal-O_2 chemistry using field ionization techniques. First, general experimental procedures are described. This is followed by description of 4 case studies: solvent characterization, alkali metal-O_2 reaction chemistry characterization, side reaction characterization, and catalyst exploration. The information described in this section is an extension of the work presented at the 233rd Electrochemical Society Conference [239].

7.1 Experimental Considerations

This section describes experimental considerations that must be taken when characterizing alkali metal-O_2 chemistry using field emitter. The discussion is divided in 2 components: one focusing on deposit formation chemistry characterization and the other focusing on morphology characterization.

7.1.1 Deposit formation chemistry

PFD experiments are performed at a negative field for discharge and a positive field for charge. Due to the small magnitude of fields required for field emission, care must be taken to avoid electron emission in the sample. This can be done by performing desorption at fields below the electron emission field. Meanwhile, for positive base field experiments, the largest reaction field used will

be onset of desorption field, as determined by RFD experiments. In order to ensure that no product accumulation occurs during the experiment, the maximum magnitude for the pulsed field has to be chosen such that all reaction products are removed. Positive desorption fields should be used since they allow for exploration of a wider reaction window.

7.1.2 Morphology characterization

Using the information obtained from the PFD experiments, FIM and FEM experiments can be performed to characterize deposit morphology, conductivity, and mapping the regions where deposit growth occurs. Prior to applying the desorption fields, deposits should be formed at the base field that yields the highest ion signal for a given species, as obtained by PFD experiments. This is done to simulate deposit growth at experimentally relevant conditions. After deposit growth, the field is stepped to the desorption field used in PFD experiments, followed by video acquisition. Due to time variations in emission, video acquisition is recommended. Typically, 10 s are used. The resulting video is then processed using frame-averaging to obtain a micrograph.

7.2 Solvent characterization

As described previously, the discharge mechanism in alkali metal-O_2 batteries is electrolyte dependent [193] due to solvation effects [67]. Two main pathways have been proposed: a surface pathway with strongly bound intermediates and a solution pathway where O_2^- is solvated upon reduction and LiO_2 can nucleate and disproportionate from the solution phase [67]. In addition, some solvents can react with the anode [42, 44].

A graphical depiction of experiments that address these issues is shown in Fig. 7.1. Anode stability can be assessed by adsorption of a lithium layer on the tip, followed by solvent dosing. As shown in the upper section of Fig. 7.1, PFD experiments can be performed to determine the reaction intermediates and end products. For example, if acetonitrile were used as a solvent, products such as CH_3^+ and CN^+ would be observed [40]. In addition, mass-selected RFD can be used to determine the nature of Li solvation, as well as the activation energy for the formation of solvation

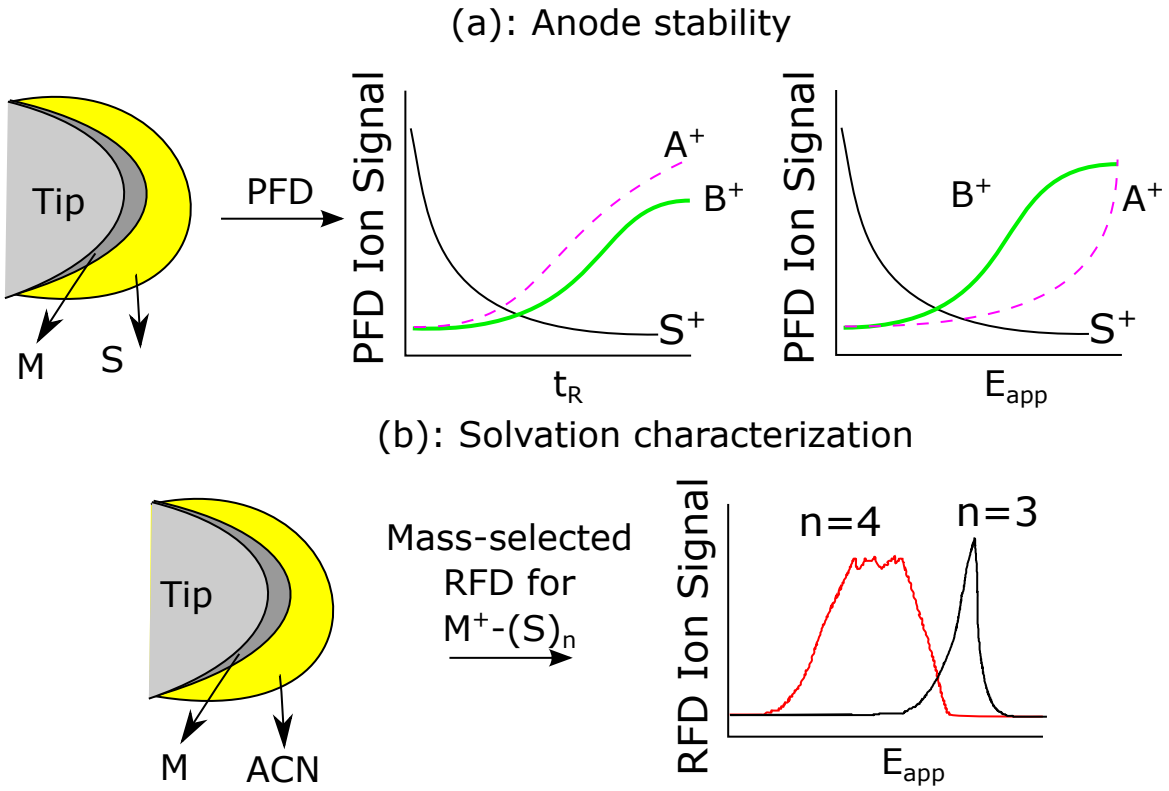

Figure 7.1: Solvent characterization experiments. The upper portion shows an electrolyte stability experiment. The bottom portion shows a solvation shell size experiment. M is the metal (Li, Na, K), S is the solvent, and A^+ and B^+ are reaction products form by the reaction of S with M.

shells and their size. A depiction of such an experiment is shown in the lower portion of Fig. 7.1. Imaging experiments can further reveal the relative activity of the different crystal facets of the tip, with more active regions appearing as brighter spots.

7.3 Characterization of alkali metal-O_2 Chemistry

The current understanding of alkali metal-O_2 battery chemistry has been limited to cycling experiments performed in electrochemical cells, followed by product characterization via optical and

mass spectroscopy techniques. Unfortunately, the complexity of electrochemical cells and the presence of side reactions complicate gaining insight of the fundamental nature of such reactions. Most of the fundamental understanding of alkali metal-O_2 chemistry has involved the use of computational tecnhiques [62, 140, 141, 143, 147, 149, 155]. There have been few experimental studies have provided insight regarding the nature of the deposits [63, 99, 194, 240, 241] and morphology [67, 94, 242, 243]. Despite this, there is limited knowledge about how variables such as electric field affect the ORR kinetics. Figure 7.2 shows a schematic of how field ionization experiments can be used to obtain information of alkali metal-O_2 chemistry. The upper portion shows a sample imaging experiment. Bright regions will be covered with either low work function deposits or thin deposits where electrons can tunnel to or from the tip. Meanwhile, the bottom inset shows a sample spectrometry experiment. A deposit can be grown in the tip and desorbed upon application of desorption pulses. Any species present in the tip are detected and the effects of reaction time, applied field, and temperature on the composition of the deposit can be assessed.

7.3.1 Deposit formation chemistry

PFD experiments can be performed using the procedure outlined in Section 7.1.1 using a carbon-lithium substrate. The carbon substrate can be grown by decomposition of ethylene at the tip, while lithium can be directly dosed using a commercially available getter. After dosing, oxygen and the solvent of interest can be dosed continuously at a total pressure below 1×10^{-6} torr to decrease the risk of microchannel plate failure due to discharge arcs [244].The flux of each species can be determined using Equation 7.1, where J_i is the incident flux of species i to the tip, P_i is the dosing pressure, N_i is the surface density of a monolayer of i, m is the molecule mass, k is Boltzmann's constant and T is the dosing temperature. Experiments can be performed at different temperatures, electric fields, and depth of discharge. Depth of discharge experiments involve dosing the metal of interest and O_2 on the substrate. Complementary to previous kinetic studies [194], a field ionization study can be used to assess how the nature of the surface affects the discharge/charge kinetics.

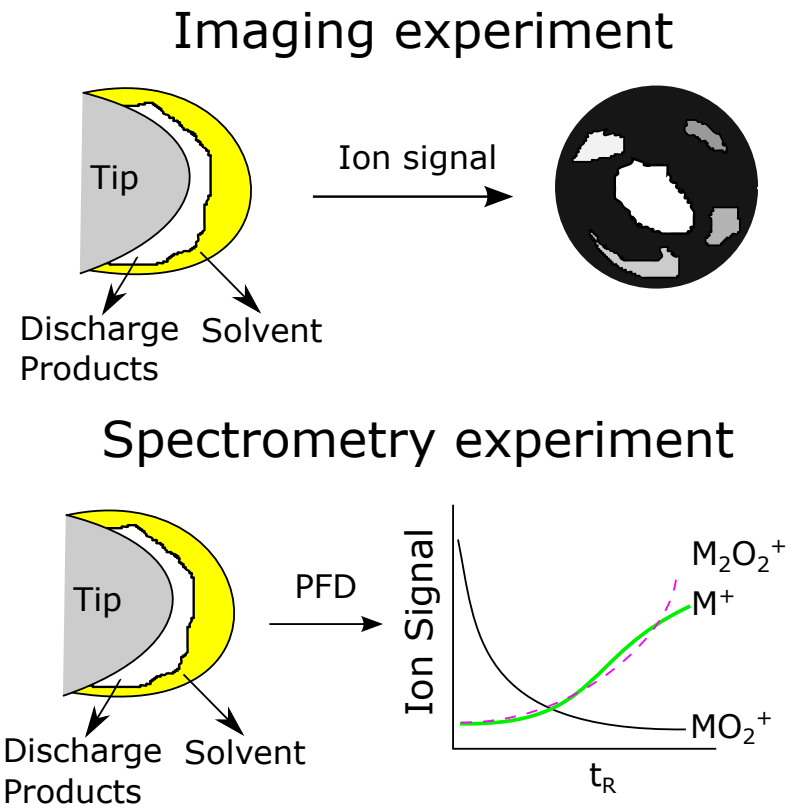

Figure 7.2: Field ionization experimental protocol. The upper portion shows a sample imaging experiment. The bottom portion shows a spectrometry experiment.

$$J_i = \frac{P_i}{N_i \sqrt{2\pi mkT}} \tag{7.1}$$

Direct assesment of field effects can be achieved rather than using voltage as the state variable. Even though electric field is directly related to potential, both variables having different effects on the system. While electric potential affects thermodynamics, electric field affects kinetics [245]. The rate of an electrochemical reaction can be given by the Butler-Volmer expression, as shown in Equation 7.2, where j is the current density, β is the symmetry factor, n is the number of electrons transferred in the rate determining step, F is Faraday's constant, η is the overpotential, R is the gas constant, T is the temperature, and j_0 is the exchange current density, given by Equation 7.3, with c_R and c_O being the anodic and cathodic reactants and k_a and k_c the anodic and cathodic rate constants, respectively [246].

$$j = j_0 \left\{ \exp\left[\frac{(1-\beta)nF\eta}{RT}\right] - \exp\left[\frac{-\beta nF\eta}{RT}\right] \right\} \tag{7.2}$$

$$j_0 = nF \left[k_a^{\beta} c_R^{\beta}\right] \left[k_c^{(1-\beta)} c_O^{(1-\beta)}\right] \tag{7.3}$$

The anodic and cathodic rate constants have a rate dependence given by Equation 7.4, where $\nu_i(E)$ is the field-dependent pre-exponential factor, E is the applied electric field, and $Q_i(E)$ is the field-dependent activation energy [230]. Inspection of Equations 7.2-7.4 shows that the electric potential primarily affects the exchange current density due to the exponential dependence on the kinetic rate constant in Equation 7.2. Meanwhile, the electric field affects the rate constant k_i through both the pre-exponential factor and the exponential terms shown in Equation 7.4.

$$k_i(E) = \nu_i(E) \exp\left(\frac{-Q_i(E)}{RT}\right) \tag{7.4}$$

7.3.2 Morphology characterization

Morphological characterization can be achieved using FIM and FEM. FEM can provide topographical information by providing information about deposit work function, with low work function deposits appearing brighter than high work function deposits. In addition, FIM can provide information about the thickness. Thicker deposits will show up as dark spots in the screen, while thinner deposits will show as brighter spots due to field distributions across the deposits. This information can be used to assess morphological changes as a function of variables such as growth field, temperature, and oxygen partial pressure.

7.4 Effect of contaminants

Contaminants such as CO_2 and H_2O have been observed to increase the discharge capacity of alkali metal-O_2 batteries at the expense of increasing charging overpotentials and decreasing cyclability [106]. For example, the presence of CO_2 leads to the formation of Li_2CO_3 via reactions with either O_2^- in solution or Li_2O_2 in Li-O_2 batteries [111]. Meanwhile, previous work has shown that the addition of water affects deposit morphology and favors a solution-mediated path, even in solvents with low DN. In addition, the presence of water can lead to parasitic reactions and the formation of LiOH [67]. This section describes how field ionization techniques can be used to assess the effects of CO_2 and H_2O in alkali metal-O_2 chemistry using PFD.

7.4.1 Characterization of reaction chemistry

In addition to exploring the effects of reaction time, temperature, and reaction field, PFD experiments can also assess the effect of O_2/CO_2 ratios and water content. In a similar manner to the alkali metal-O_2 experiments, a carbon-lithium susbtrate should be used. For depth of discharge experiments, deposit formation occurs by exposing the tip to the base field and dosing conditions for some time prior to pulsing at different gas environments. PFD experiments can be used to assess reaction intermediates such as $LiCO_4$ as a function of O_2/CO_2 ratio and field. In order to characterize deposit reactions with water, a MO_2 substrate can be used rather than carbon-lithium.

By changing the reaction time and applied field, semi-quantitative information of water reactions can be obtained such as reaction intermediates and relative rates of formation.

7.4.1.1 Morphology characterization

FEM experiments can be used to determine the work function change on the tip, as well as the nature of discharge products. It is expected that the work function will be lower compared to a case where only O_2 is used. In addition, FIM experiments can reveal if Li_2CO_3 growth is preferred at certain crystal planes. Li_2CO_3 deposits are expected to form as thin films on the carbon-coated tips. The regions where Li_2CO_3 forms are expected to be observed as bright spots in FEM. Meanwhile, the brightness will change in FIM experiments as a function of time. In the first frames, the deposits will be bright and the brightness will decrease as more Li_2CO_3 desorbs.

7.5 Catalyst exploration

A significant amount of research has been dedicated to characterizing oxygen reduction catalysts for potential applications in alkali metal-O_2 batteries. An overview of several experiments for catalyst exploration is shown in Fig. 7.3. Despite the usefulness of some catalysts in reducing the charging overpotentials, it has been found that some materials catalyze electrolyte side reactions [68]. Field ionization methods can be used to explore electrolyte degradation reactions on metal catalysts, as shown at panel (a) of Fig. 7.3.

In addition to electrolyte degradation characterization, experiments can be performed to study the charge transfer reactions on such catalysts. In such experiments, a M_xO_2 deposit can be made by dosing Li and oxygen onto the tip, followed by the solvent of interest. Panels (a) and (b) show M_xO_2 and the solvent of interest dosed onto 2 different metals, A and B, with A being more catalytically active than B. Information about the reaction pathway, intermediates, and activation energies can be obtained with PFD, as shown in panel (c). In addition, imaging experiments can reveal active regions of the tip during charge, as shown in panel (d). Highly active areas will show as bright regions due to a higher rate of ionization, while inactive areas will appear dark. In a

hypothetical experiment, the figure shows how a sample of metal A would have a highly active region at the center of the image with less active spots in the 4 quadrants. Meanwhile, a sample of metal B only exhibits moderate activity at the quadrants.

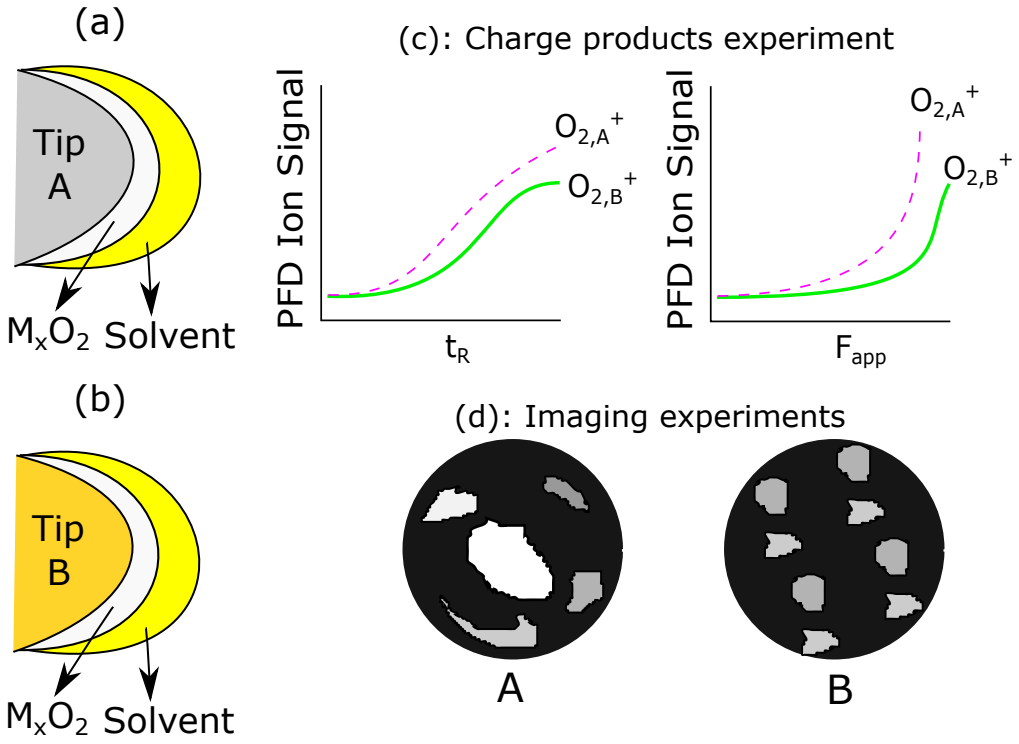

Figure 7.3: Catalyst exploration experiments. Panels (a) and (b) show experimental procedures for tips made of different metals, where A is more catalytically active than B. Panel (c) shows the hypothetical O_2^+ ion signal for both materials as a function of t_R and F_{app}, while panel (d) shows a depiction of an imaging experiment.

Chapter 8

CONCLUSIONS AND RECOMMENDATIONS

The purpose of this work was to provide an extensive review of the limitations of alkali metal-O_2 battery chemistry and new framework for future research based on well-defined surface states and kineticially relevent state. Despite this, the implementation of some of the ideas described previously may prove challenging. However, their benefits can potentially outweigh the challenges and might help towards the commercialization and large-scale deployment of alkali metal-O_2 batteries.

8.1 Field ionization

The original aim of the work described in this dissertation was to characterize Li-O_2 battery chemsitry using field emitters. However, due to limitations with the instrument, it was not possible to carry out the proposed experiments. In order to carry out work with the FIM described previously, several upgrades are needed. First, a new isolation box needs to be built. The original isolation box was built in 1996 and was not used for a decade. In addition, the documentation was not kept up to date, and there were several issues such as AC noise in DC channels that proved challenging to remove. Such issues are described in further detail in Appendix A. Finally, the picosecond time analyzer (PTA) used for acquiring PFD data needs to be upgraded. Despite the PTA still working properly, the unit has not been supported for at least a decade and therefore, a replacement is needed.

The ability of field ionization techniques to examine reactions in a fundamental way makes it an ideal tool to characterize alkali metal-O_2 batteries. However, the uniqueness of the technique and the lack of available field ionization microscopes (to the author's knowledge there are 2 or 3 operational microscopes in the world) provides significant experimental challenges. Despite this, there

is value in using the technique. The protocols described in Chapter 7 provide a starting point for chemistry characterization. In addition, recent work has proposed the evolution of singlet oxygen as the main cause for parasitic reactions [247]. One difference between singlet and triplet oxygen is the smaller polarizability of singlet oxygen [248]. Due to the polarizability dependence of the activation energy in field-dependent reactions, it might be possible to detect such species. Other uses of field ionization include characterization of new electrolyte solvents or cathode materials.

8.2 Well-defined surface and kinetically relevant states

A concept proposed in previous chapters involved the development of well-defined surface and kinetically relevant states for better understanding of alkali metal-O_2 chemistry. Well-defined surface states are those with well-defined Li_2O_2 coverages, morphology, and cathode surface conditions that can be used to characterize reactions occuring in alkali metal-O_2 reactions in a controlled environment. The use of potentiostatic discharge rather than galvanostatic discharge was recommended as it allows for isolation of specific reactions. In addition, several applications were focused on the characterization of deposit evolution: initial nucleation and growth, spatio-temporal evolution of the chemical identity and crystallinity of discharge products, and stage-by-stage characterization. An extension of this concept involves the usage of kinetically relevent states defined according to features from discharge/charge curves such as inflection points, plateaus, or regions of constant slope.

The use of both KRS and WDSS for characterization must be coupled with *in operando* techniques in order to obtain information about deposit composition, morphology, spacial distribution, and active regions of the cathode. The information obtained from both WDSS and KRS can potentially provide a framework for battery design. For example, the information obtained in initial nucleation and growth experiments using WDSS and scanning probe techniques could be used for developing improved cathode materials by providing informastion about effect of parameters such as M_xO_2-substrate binding energy on deposit growth. In addition, a KRS experiment coupled with traditional characterization techniques could be used to assess the effects of cathode microstructure and nucleation sites on cell death and morphology, allowing for the development of improved cath-

ode designs. Finally, isotope alternation experiments coupled with *in operando* techniques such as ambient pressure XPS and X-ray tomography can provide more accurate information about the products oxidized at each stage of the charging process, as well as pin-pointing where they are formed.

BIBLIOGRAPHY

[1] G. W. Huber, S. Iborra, and A. Corma. Synthesis of Transportation Fuels from Biomass: Chemistry, Catalysts, and Engineering. *Chemical Reviews*, 106:4044–4098, 2006.

[2] US Energy Information Administration. Monthly Energy Review, July 2018.

[3] Z. Yang, J. Zhang, M. C. W. Kintner-Mayer, X. Lu, D. Choi, J. P. Lemmon, and J. Liu. Electrochemical Energy Storage for Green Grid. *Chemical Reviews*, 111:3577–3613, 2011.

[4] J. Twidell and T. Weir. *Renewable Energy Resources*. Taylor & Francis, New York, second edition, 2006.

[5] J. B. Goodenough and K. Park. The Li-Ion Rechargeable Battery: A Perspective. *J. Am. Chem. Soc*, 135:1167–1176, 2013.

[6] Z. Zhan, W. Kobsiriphat, J. R. Wilson, M. Pillai, H. Kim, and S. A. Barnett. Syngas Production By Coelectrolysis of CO_2 and H_2O: The Basis for a Renewable Energy Cycle. *Energy and Fuels*, 23:3089–3096, 2009.

[7] M. Carmo, D. L. Fritz, J. Mergel, and D. Stolten. A comprehensive review on PEM water electrolysis. *International Journal of Hydrogen Energy*, 38:4901–4934, 2013.

[8] V. Etacheri, R. Marom, R. Elazari, G. Salitra, and D. Aurbach. Challenges in the development of advanced Li-ion batteries: a review. *Energy Environ. Sci*, 4:3243–3262, 2011.

[9] J. Lu, J. Park, Y. Sun, F. Wu, and K. Amine. Aprotic and Aqueous Li-O_2. *Chemical Reviews*, 114:5611–5640, 2014.

[10] A. C. Luntz and B. D. McCloskey. Nonaqueous lI-air Batteries: A Status Report. *Chemical Reviews*, 114:11721–11750, 2014.

[11] Y. Liu, L. Wang, L. Cao, C. Shang, Z. Wang, H. Wang, L. He, J. Yang, H. Cheng, J. Li, and Z. Lu. Understanding and suppressing side reactions in Li-air batteries. *Mat. Chem. Front.*, 1:2495–2510, 2017.

[12] X. Ren and Y. Wu. A Low-Overpotential Potassium-Oxygen Battery Based on Potassium Superoxide. *J. Am. Chem. Soc*, 135:2923–2926, 2012.

[13] C. L. Bender, D. Schröder, R. Pinedo, P. Adelhelm, and J. Janek. One- or -Two-Electron Transfer? The Ambiguous Nature of Discharge Products in Sodium-Oxygen Batteries. *Angew. Chem. Int. Ed.*, 55:4640–4649, 2016.

[14] G. Girishkumar, B. McCloskey, A. C. Luntz, S. Swanson, and W. Wilcke. Lithium-Air Battery: Promise and Challenges. *J. Phys. Chem. Lett*, 1:2193–2203, 2010.

[15] J. Christensen, P. Albertus, R. S. Sánchez-Carrera, T. Lohmann, B. Kozinsky, R. Liedtke, J. Ahmed, and A. Kojic. A Critical Review of Li/Air Batteries. *Journal of the Electrochemical Society*, 159(2):R1–R30, 2012.

[16] P. Stevens, G. Toussaint, G. Caillon, P. Viaud, P. Vinatier, C. Cantau, O. Fichet, C. Sarrazin, and M. Mallouki. Development of a lithium air rechargeable battery. *ECS Transactions*, 28(32):1–12, 2010.

[17] T. Zhang, N. Imanishi, S. Hasegawa, A. Hirano, J. Xie, Y. Takeda, O. Yamamoto, and N. Sammes. Li/Polymer Electrolyte/Water Stable Lithium-Conducting Glass Ceramics Composite for Lithium-Air Secondary Batteries with an Aqueous Electrolyte. *Journal of the Electrochemical Society*, 155(12):A965–A969, 2008.

[18] C. O. Laoire, S. Mukerjee, K. M. Abraham, E. J. Plichta, and M. A. Hendrickson. Elucidating the Mechanism of Oxygen Reduction for Lithium-Air Battery Applications. *J. Phys. Chem. C*, 113:20127–20134, 2009.

[19] National Institute of Standards and Technology. Nist-janaf thermochemical tables. Online, 1998.

[20] W. Yu, K. C. Lau, Y. Lei, R. Liu, L. Qin, W. Yang, B. Li, L. A. Curtiss, D. Zhai, and F. Kang. Dendrite-Free Potassium-Oxygen Battery Based on a Liquid Alloy Anode . *ACS Appl. Mater. Interfaces*, 9:31781–31878, 2017.

[21] L. Qu, Y. Liu, J. Baek, and Dai L. Nitrogen-Doped Graphene as Efficient Metal-Free Electrocatalyst for Oxygen Reduction in Fuel Cells. *ACS Nano*, 4(3):1321–1326, 2010.

[22] Z. Wang, D. Xu, J. Xu, L. Zhang, and X. Zhang. Graphene Oxide Gel-Derived, Free-Standing, Hierarchically Porous Carbon for High-Capacity and High-Rate Rechargeable Li-O_2 Batteries. *Adv. Funct. Mater*, 22:3699–3705, 2012.

[23] F. Li, D. Tang, Y. Chen, D. Golberg, H. Kitaura, T. Zhang, A. Yamada, and H. Zhou. Ru/ITO: A Carbon-Free Cathode for Nonaqueous Li-O_2 Battery. *Nano Lett.*, 13:4702–4707, 2013.

[24] Z. Peng, S. A. Freunberger, Y. Chen, and P. G. Bruce. A Reversible and Higher-Rate Li-O_2 Battery. *Science*, 337:563–566, 2012.

[25] M. M. O. Thotyil, S. A. Freunberger, Z. Peng, Y. Chen, Z. Lu, and P. G. Bruce. A stable cathode for the aprotic Li-O_2 battery. *Nat. Mater.*, 12:1050–1056, 2013.

[26] A. Riaz, K. Jung, W. Chang, S. Lee, T. Lim, S. Park, R. Song, S. Yoon, K. Shin, and J. Lee. Carbon-free cobalt oxide cathodes with tunable nanoarchitectures for rechargeable lithium-oxygen batteries. *Chem. Commun.*, 49:5984–5986, 2013.

[27] M. M. O. Thotyil, S. A. Freunberger, Z. Peng, and P. G. Bruce. The Carbon Electrode in Nonaqueous Li-O_2 Cells. *J. Am. Chem. Soc*, 135:494–500, 2013.

[28] M. M. Ottakam Thotiyl, S. A. Freunberger, Z. Peng, and P. G. Bruce. The Carbon Electrode in Nonaqueous Li-O_2 Cells. *J.Am. Chem. Soc.*, 135:494–500, 2013.

[29] Y. Li, Z. Liu, Q. Li, Z. Liu, and Z. Li. Superior energy capacity of graphene nanosheets for a nonaqueous lithium-oxygen battery. *Hydrometallurgy*, 105:9438–9440, 2011.

[30] E. P. Roth, D. P. Doughty, and J. Franklin. DSC investigation of exothermic reactions occurring at elevated temperatures in lithium-ion anodes containing PVDF-based binders. *Journal of Power Sources*, 134:222–234, 2004.

[31] N. Böckenfeld, S. S. Jeong, M. Winter, S. Passerini, and A. Balducci. Natural, cheap and environmentally friendly binder for supercapacitors. *Journal of Power Sources*, 221:14–20, 2013.

[32] C. O. Laoire, S. Mukerjee, K. M. Abraham, E. J. Plichta, and M. A. Hendrickson. Influence of Nonaqueous Solvents on the Electrochemistry of Oxygen in the Rechargeable Lithium-Air Battery. *J. Phys. Chem. C*, 114:9178–9186, 2010.

[33] J. Read. Characterization of the Lithium-Oxygen Organic Electrolyte Battery. *Journal of the Electrochemical Society*, 149(9):A1190–A1195, 2002.

[34] J. Kim, H. D. Lim, H. Gwon, and K. Kang. Sodium-oxygen batteries with alkyl-carbonate and ether based electrolytes. *Phys. Chem. Chem. Phys.*, 15:3623–3629, 2013.

[35] S. A. Freunberger, Y. Chen, N. E. Drewett, L. J. Hardwick, F. Bardé, and P. G. Bruce. The Lithium-Oxygen Battery with Ether-Based Electrolytes. *Angew. Chem. Int. Ed*, 50:8609–8613, 2011.

[36] B. D. McCloskey, R. Scheffler, A. Speidel, G. Girishkumar, and Luntz A. C. On the Mechanism of Nonaqueous Li-O_2 Electrochemistry on C and Its Kinetic Overpotentials: Some Implications for Li-Air Batteries. *J. Phys. Chem. C*, 116:23897–23905, 2012.

[37] N. Zhang and X. Guo. Cell Chemistry of Sodium-Oxygen Batteries with Various Nonaqueous Electrolytes. *J. Phys. Chem. C*, 119:25319–25326, 2015.

[38] Z. Peng, S. A. Freunberger, L. J. Hardwick, Y. Chen, V. Giordani, F. Bardé, P. Novák, D. Graham, J-M. Tarascon, and P. G. Bruce. Oxygen Reactions in a Non-Aqueous Li^+ Electrolyte. *Angew. Chem. Int. Ed*, 50:6351–6355, 2011.

[39] R. Younesi, P. Norby, and T. Vegge. A New Look at the Stability of Dimethyl Sulfoxide and Acetonitrile in Li-O_2 Batteries. *ECS Electorchemistry Letters.*, 3(3):A15–A18, 2014.

[40] M. W. Rupich, L. Pitts, and K. M. Abraham. Characterization of Reactions and Products of the Discharge and Forced Overdischarge of Li/SO_2 Cells. *Journal of the Electrochemical Society*, 129(9):1857–1861, 1982.

[41] M. Balaish, A. Kraytsberg, and Y. Ein-Eli. A critical review on lithium-air battery electrolytes. *Phys. Chem. Chem. Phys.*, 55:2801–2822, 2016.

[42] Y. Yamada, K. Furukawa, K. Sodeyama, K. Kikuchi, M. Yaegashi, Y. Tateyama, and A. Yamada. Unusual Stability of Acetonitrile-Based Superconcentrated Electrolytes for Fast-Charging Lithium-Ion Batteries. *J. Am. Chem. Soc*, 136:5039–5045, 2014.

[43] Y. Yamada and A. Yamada. Review-Superconcentrated Electrolytes for Lithium Batteries. *Journal of the Electrochemical Society*, 162(14):A2406–A2423, 2015.

[44] D. G. Kwabi, T. P. Batcho, C. V. Amanchukwu, N. Ortiz-Vitoriano, P. Hammond, C. V. Thompson, and Y. Shao-Horn. Chemical Instability of Dimethyl Sulfoxide in Lithium-Air Batteries. *J. Phys. Chem. Lett*, 5:2850–2856, 2014.

[45] T. Kuboki, T. Okuyama, T. Ohsaki, and N. Takami. Lithium-air batteries using hydrophobic room temperature ionic liquid electrolyte. *Journal of Power Sources*, 146:766–769, 2005.

[46] S. Meini, S. Solchenbach, M. Piana, and H. A. Gasteiger. The Role of Electrolyte Solvent Stability and Electrolyte Impurities in the Electrooxidation of Li_2O_2 in Li-O_2 Batteries. *Journal of the Electrochemical Society*, 161(9):A1306–A1314, 2014.

[47] S. J. Visco, L. C. De Jonghe, Y. S. Nimon, A. Petrov, and K. Pridatko. Cathodes and reservoirs for aqueous lithium/air battery cells, 2013.

[48] S. J. Visco, L. C. De Jonghe, Y. S. Nimon, A. Petrov, and K. Pridatko. Catholytes for aqueous lithium/air battery cells, 2014.

[49] J. Fu. Superionic conductivity of glass-ceramics in the system Li_2O-Al_2O_3-TiO_2-P_2O_5. *Solid State Ionics*, 96:195–200, 1997.

[50] P. He, Y. Wang, and H. Zhou. A Li-air fuel cell with recycle aqueous electrolyte for improved stability. *Electrochemistry Communications*, 12:1686–1689, 2010.

[51] K. M. Abraham and Z. Jiang. A Polymer Electrolyte-Based Rechargeable Lithium/Oxygen Battery. *Journal of the Electrochemical Society*, 143(1):1–5, 1996.

[52] J. Hassoun, M. Croce, M. Armand, and B. Scrosati. Investigation of the O_2 Electrochemistry in a Polymer Electrolyte Solid-State Cell. *Angew. Chem. Int. Ed.*, 50:2999–3002, 2011.

[53] Y. Liu, Y. Takeda, T. Matsumura, J. Yang, N. Imanishi, A. Hirano, and O. Yamamoto. Novel Composite Anodes Consisting of Lithium Transition-Metal Nitrides and Transition Metal Oxides for Rechargeable Li-Ion Batteries. *J. Phys. Chem. Lett.*, 153(2):A437–A444, 2006.

[54] J. R. Harding, C. V. Amanchukwu, P. T. Hammond, and Y. Shao-Horn. Instability of Poly(ethylene oxide) upon Oxidation in Lithium-Air Batteries. *J. Phys. Chem. C*, 119:6947–6955, 2015.

[55] E. Peled. The Electrochemical Behavior of Alkali and Alkaline Earth Metals in Nonaqueous Battery Systems-The Solid Electrolyte Interphase Model. *Journal of the Electrochemical Society*, 196:6835–6840, 1979.

[56] X. Cheng, R. Zhang, C. Zhao, F. Wei, J. Zhang, and Q. Zhang. A Review of Solid Electrolyte Interphases on Lithium Metal Anode. *Adv. Sci.*, 3:1500213, 2012.

[57] A. Schechter, D. Aurbach, and H. Cohen. X-ray Photoelectron Spectroscopy Study of Surface Films Formed on Li Electrodes Freshly Prepared in Alkyl Carbonate Solutions. *Langmuir*, 15:3334–3342, 1999.

[58] S. Xiong, K. Xie, Y. Diao, and X. Hong. Characterization of the solid electrolyte interphase on lithium anode for preventing the shuttle mechanism in lithium-sulfur batteries. *J. Power Sources*, 246:840–845, 2014.

[59] S. Ganapathy, B. D. Adams, G. Stenou, M. S. Anastasaki, K. Goubitz, X. Miao, L. F. Nazar, and M. Wagemaker. Nature of Li_2O_2 Oxidation in a Li-O2 Battery Revealed by Operando X-ray Diffraction. *J. Am. Chem. Soc*, 136:16335–16344, 2014.

[60] P. Adelhelm, P. Hartmann, C. L. Bender, M. Busche, C. Eufinger, and J. Janek. From lithium to sodium: cell chemistry of room temperature sodium-air and sodium-sulfur batteries . *Beilstein J. Nanotechnol.*, 6:1016–1055, 2015.

[61] B. D. McCloskey, D. S. Bethune, R. M. Shelby, T. Mori, R. Scheffler, A. Speidel, M. Sherwood, and Luntz A. C. Limitations in Rechargeability of Li-O_2 Batteries and Possible Origins. *J. Phys. Chem. Lett.*, 3:3045–3047, 2012.

[62] J. S. Hummelshøj, A. C. Luntz, and J. K. Nørskov. Theoretical evidence for low kinetic overpotentials in Li-O_2 electrochemistry. *J. Chem. Phys*, 138:034703, 2013.

[63] V. Viswanathan, J. K. Nørskov, A. Speidel, R. Scheffler, S. Gowda, and A. C. Luntz. Li-O_2 Kinetic Overpotentials: Tafel Plots from Experiment and First-Principles Theory. *J. Phys. Chem. Lett.*, 4:556–560, 2013.

[64] C. O. Laoire, S. Mukerjee, K. M. Abraham, E. J. Plichta, and M. A. Hendrickson. Elucidating the Mechanism of Oxygen Reduction for Lithium-Air Battery Applications. *J. Phys. Chem. C*, 113:20127–20134, 2009.

[65] K. M Abraham. Electrolyte-Directed Reactions of the Oxygen Electrode in Lithium-Air Batteries. *Journal of the Electrochemical Society*, 162(2):A3021–A3031, 2015.

[66] V. Gutmann. Empirical Parameters for Donor and Acceptor Properties of Solvents. *Electrochimica Acta*, 21:661–670, 1976.

[67] N. B. Aetukuri, B. D. McCloskey, J. M. García, L. E. Krupp, V. Viswanathan, and A. C. Luntz. Solvating additives drive solution-mediated electrochemistry and enhance toroid growth in non-aqueous Li-O_2 batteries. *Nature Chemistry*, 7:50–55, 2015.

[68] B. D. McCloskey, R. Scheffler, A. Speidel, D. S. Bethune, R. M. Shelby, and Luntz A. C. On the Efficacy of Electrocatalysts in Li-O_2 Batteries. *J. Am. Chem. Soc.*, 133:18038–18041, 2011.

[69] B. D. McCloskey, J. M. Garcia, and A. C. Luntz. Chemical and Electrochemical Differences in Nonaqueous Li-O_2 and Na-O_2 Batteries. *J. Phys. Chem. Lett.*, 5(7):1230–1235, 2014.

[70] W. Liu, Q. Sun, Y. Yang, J. Y. Xie, and Z. W. Fu. An enhanced electrochemical performance of a sodium-air battery with graphene nanosheets as air electrode catalysts. *Chem. Commun.*, 49:1951–1953, 2013.

[71] C. O. Laoire, S. Mukerjee, E. J. Plichta, M. A. Hendrickson, and K. M. Abraham. Rechargeable Lithium/TEGDME-$LiPF_6$/O_2 Battery. *Journal of the Electrochemical Society*, 158(3):A302–A308, 2011.

[72] N. Zhao, C. Li, and X. Guo. Long-life Na-O_2 batteries with high energy efficiency enabled by electrochemically splitting NaO_2 at a low overpotential. *Phys. Chem. Chem. Phys.*, 16:15646–15652, 2014.

[73] Y. Hu, X. Han, Q. Zhao, J. Du, F. Cheng, and J. Chen. Porous perovskite calcium-manganese oxide microspheres as an efficient catalyst for rechargeable sodium-oxygen batteries. *J. Mater. Chem. A*, 3:3320–3324, 2015.

[74] H. Lim, B. Lee, Y. Bae, H. Park, Y. Ko, H. Kim, J. Kim, and K. Kang. Reaction chemistry in rechargeable Li-O_2 batteries. *Chem. Soc. Rev.*, 46:2873–2888, 2017.

[75] D. M. Seo, O. Borodin, D. Balogh, M. O'Connell, Q. Ly, S. D. Han, S. Passerini, and W. A. Henderson. Electrolyte Solvation and Ionic Association III. Acetonitrile-Lithium Salt Mixtures-Transport Properties. *Journal of the Electrochemical Society*, 160(8):A1061–A1070, 2013.

[76] D. M. Seo, O. Borodin, S. D. Han, Q. Ly, P. D. Boyle, and W. A. Henderson. Electrolyte Solvation and Ionic Association I. Acetonitrile-Lithium Salt Mixtures: Intermediate and Highly Associated Salts. *Journal of the Electrochemical Society*, 159(5):A553–A1565, 2012.

[77] W. A. Henderson. Glyme-Lithium Salt Phase Behavior. *J. Phys. Chem. B*, 110:13177–13183, 2006.

[78] E. Pasgreta, R. Puchta, A. Zahl, and R. van Eldik. Ligand-Exchange Processes on Solvated Lithium Cations: Acetonitrile and Hydrogen Cyanide. *Eur. J. Inorg. Chem.*, 13:1815–1822, 2007.

[79] E. Pasgreta, R. Puchta, M. Galle, N. van Eikema Hommes, A. Zahl, and R. van Eldik. Ligand-Exchange Processes on Solvated Lithium Cations: DMSO and Water/DMSO Mixtures. *ChemPhysChem*, 8:1315–1320, 2007.

[80] Y. Che, M. Tsushima, F. Matsumoto, T. Okajima, K. Tokuda, and T. Ohsaka. Water-Induced Disproportionation of Superoxide Ion in Aprotic Solvents. *J. Phys. Chem.*, 100:20134–20137, 1996.

[81] R. R. Mitchell, B. M. Gallant, C. V. Thomson, and Y. Shao-Horn. All-carbon-nanofiber electrodes for high-energy rechargeable Li-O_2 batteries. *Energy Environ Sci*, 4:2952–2958, 2011.

[82] C. M. Burke, V. Pande, A. Khetan, V. Viswanathan, and B. D. McCloskey. Enhanced electrochemical intermediate solvation through electrolyte anion selection to increase nonaqueous Li-O_2 battery capacity. *Proc. Natl. Ac. Sci.*, 112(30):9293–9298, 2015.

[83] P. Tan, W. Shyy, T. S. Zhao, Z. H. Wei, and L. An. Discharge product morphology versus operating temperature in nonaqueous lithium-air batteries. *Journal of Power Sources*, 278:133–140, 2015.

[84] N. Ortiz-Vitoriano, T. P. Batcho, D. G. Kwabi, B. Han, N. Pour, K. P. C. Yao, C. V. Thompson, and Y. Shao-Horn. Rate-Dependent Nucleation and Growth of NaO_2 in Na-O_2 Batteries . *J. Phys. Chem. Lett.*, 135:2636–2643, 2013.

[85] Z. Liang, Q. Zou, Y. Wang, and Y. C. Lu. Recent Progress in Applying In Situ/Operando Characterization Techniques to Probe the Solid/Liquid/Gas Interfaces of Li-O_2 Batteries. *Small Methods*, 1:1700150, 2017.

[86] P. P. R. M. L. Harks, F. M. Mulder, and P. H. L. Notten. In situ methods for Li-ion battery research: A review of recent developments. *Journal of Power Sources*, 288:92–105, 2015.

[87] D. Schröder, C. L. Bender, T. Arit, M. Osenberg, A. Hilger, S. Risse, M. Ballauf, I. Manke, and J. Janek. In operando x-ray tomography for next-generation batteries: a systematic approach to monitor reaction product distribution and transport processes. *J. Phys D: Appl. Phys.*, 49:404001, 2016.

[88] E. Maire and P. J. Withers. Quantitative X-ray tomography. *Int. Mater. Rev.*, 59(1):1–43, 2014.

[89] D. Schröder, C. L. Bender, M. Osenberg, A. Hilger, I. Manke, and J. Janek. Visualizing current-dependent morphology and distribution of discharge products in sodium–oxygen battery cathodes . *Scientific Reports*, 6:24288, 2016.

[90] Y. Li, H. Yadegari, X. Li, M. N. Banis, R. Li, and X. Sun. Superior catalytic activity of nitrogen-doped graphene cathodes for high energy capacity sodium-air batteries. *Chem. Commun.*, 49:11731–11733, 2013.

[91] R. R. Mitchell, B. M. Gallant, Y. Shao-Horn, and C. V. Thomson. Mechanisms of Morphological Evolution of Li_2O_2 Particles during Electrochemical Growth. *J. Phys. Chem. Lett*, 4:1060–1064, 2013.

[92] J. Lee, R. Black, G. Popov, E. Pomerantseva, F. Nan, G. A. Botton, and L. F. Nazar. The role of vacancies and defects in $Na_{0.44}MnO_2$ nanowire catalysts for lithium-oxygen batteries. *Energy Environ Sci*, 5:9558–9565, 2012.

[93] C. Xia, M. Waletzko, L. Chen, K. Peppler, P. J. Klar, and J. Janek. Evolution of Li_2O_2 Growth and Its Effect on Kinetics of Li-O_2 Batteries. *ACS Appl. Mater. Interfaces*, 6:12083–12092, 2014.

[94] B. D. Adams, C. Radtke, R. Black, M.L. Trudeau, K. Zaghib, and L. F. Nazar. Current density dependence of peroxide formation in the Li-O_2 battery and its effect on charge. *Energy Environ. Sci.*, 6:1772–1778, 2013.

[95] B. Horstmann, B. Gallant, R. Mitchell, W. G. Bessler, Y. Shao-Horn, and M. Z. Bazant. Rate-Dependent Morphology of Li_2O_2 Growth in Li-O_2 Batteries. *J. Phys. Chem. Lett.*, 4:4217–4222, 2013.

[96] F. S. Gittleson, K. P. C. Yao, D. G. Kwabi, S. Y. Sayed, W. H. Ryu, Y. Shao-Horn, and A. D. Taylor. Raman Spectroscopy in Lithium-Oxygen Battery Systems. *ChemElectroChem*, 1:1446–1457, 2010.

[97] R. L. McCreery. *Raman Spectroscopy for Chemical Analysis*. Wiley-Interscience, New York, 2000.

[98] F. S. Gittleson, W. H. Ryu, and A. D. Taylor. Operando Observation of the Gold-Electrolyte Interface in Li-O_2 Batteries. *ACS Appl. Mater. Interfaces*, 6:19017–19025, 2014.

[99] L. Johnson, C. Li, Z. Liu, Y. Chen, S. A. Freunberger, P. C. Ashok, B. B. Praveen, K. Dholakia, J. M. Tarascon, and P. G. Bruce. The role of LiO_2 solubility in O_2 reduction in aprotic solvents and its consequences for Li-O_2 batteries. *Nature Chemistry*, 6:1091–1099, 2014.

[100] P. Hartmann, C. L. Bender, M. Vračar, A. K. Dürr, A. Gaursuch, J. Janek, and P. Adelhelm. A rechargeable room-temperature sodium superoxide (NaO_2) battery. *Nat. Mater.*, 12:228–232, 2013.

[101] S. Y. Kang, Y. Mo, S. P. Ong, and G. Ceder. Nanoscale Stabilization of Sodium Oxides: Implications for Na-O_2 Batteries. *Nano Lett.*, 14:1016–1020, 2014.

[102] J. E. Nichols and B. D. McCloskey. The Sudden Death Phenomena in Nonaqueous Na-O_2 Batteries. *J. Phys. Chem. C*, 121:85–96, 2017.

[103] J. E. Nichols, K. B. Knudsen, and B. D. McCloskey. Oxygen Pressure Influences Spatial NaO_2 Deposition and the Sudden Death Mechanism in Na-O_2 Batteries. *J. Phys. Chem. C*, 122:13462–13472, 2018.

[104] M. E. Orazem and B. Tribollet. *Electrochemical Impedance Spectroscopy*. Wiley, New York, 2008.

[105] K. B. Knudsen, J. E. Nichols, T. Vegge, B. D. Luntz, A. C. McCloskey, and J. Hjelm. An Electrochemical Impedance Spectroscopy Study of the Capacity Limitations in Na-O_2 Cells. *J. Phys. Chem. C*, 120:10799–10805, 2016.

[106] S. R. Gowda, A. Brunet, G. M. Wallraff, and B. D. McCloskey. Implications of CO_2 Contamination in Rechargeable Nonaqueous Li-O_2 Batteries. *J. Phys. Chem. Lett.*, 4:1613–1629, 2013.

[107] K. Takechi, T. Shiga, and T. Asaoka. A Li-O_2/CO_2 battery. *Chem. Comm.*, 47:3463–3465, 2011.

[108] W. J. Albery, D. Clark, H. J. J. Drummond, A. J. M. Coombs, W. K. Young, and C. E. W. Han. Pulsed titration sensors Part 1: A breath-by-breath CO_2 sensor. *J. Electroanal. Chem.*, 340:99–110, 1992.

[109] J. L. Roberts, T. S. Calderwood, and D. T. Sawyer. Nucleophilic Oxygenation of Carbon Dioxide by Superoxide Ion in Aprotic Media To Form the $C_2O_{62}{}^-$ Species. *J. Am. Chem. Soc.*, 106:4667–4670, 1984.

[110] H. Lim, H. Lim, K. Park, D. Seo, H. Gwon, J. Hong, W. A. Goddard III, H. Kim, and K. Kang. Towards a Lithium-"Air" Battery: The Effect of CO_2 on the Chemistry of a Lithium-Oxygen Cell. *J. Am. Chem. Soc.*, 135:9733–9742, 2013.

[111] W. Yin, A. Grimaud, F. Lepoivre, C. Yang, and J. M. Tarascon. Chemical vs electrochemical formation of Li_2CO_3 as a discharge product in li-O_2/CO_2 batteries by controlling the superoxide intermediate. *J. Phys. Chem. Lett.*, 8:214–222, 2017.

[112] X. Ren, K. C. Lau, M. Yu, X. Bi, E. Kreidler, L. A. Curtiss, and Y. Wu. Understanding Side Reactions in K-O_2 Batteries for Improved Cycle Life. *ACS Appl. Mater. Interfaces*, 6:19299–19307, 2014.

[113] M . Olivares-Marin, A. Sorrentino, R. C. Lee, E. Pereiro, N. L. Wu, and D. Tonti. Spatial Distributions of Discharged Products of Lithium-Oxygen Batteries Revealed by Synchrotron X-ray Transmission Microscopy. *Nano Lett.*, 15:6932–6938, 2015.

[114] S. Meini, M. Piana, N. Tsiouvaras, A. Garsuch, and H. A. Gasteiger. The Effect of Water on the Discharge Capacity of a Non-Catalyzed Carbon Cathode for Li-O_2 Batteries . *Electrochemical and Solid-State Letters*, 15(4):A45–A48, 2012.

[115] K. U. Schwenke, M. Metzger, T. Restle, M. Piana, and H. A. Gasteiger. The Influence of Water and Protons on Li_2O_2 Crystal Growth in Aprotic Li-O_2 Cells. *Journal of the Electrochemical Society*, 162(4):A573–A584, 2015.

[116] Z. Guo, X. Dong, S. Yuan, Y. Wang, and Y. Xia. Humidity effect on electrochemical performance of Li-O_2 batteries. *Journal of Power Sources*, 264:1–7, 2014.

[117] M. H. Cho, J. Trottier, C. Gagnon, P. Hovington, D. Clément, A. Vijh, C. S. Kim, A. Guerfi, R. Black, L. Nazar, and K. Zaghib. The effects of moisture contamination in the Li-O_2 battery. *Journal of Power Sources*, 268:565–574, 2014.

[118] D. T. Sawyer and J. S. Valentine. How Super is Superoxide? *Acc. Chem. Res.*, 14:393–400, 1981.

[119] D. T. Sawyer, G. Chiericato Jr, C. T. Angells, E. J. Nanni Jr, and T. Tsuchiya. Effects of Media and Electrode Materials on the Electrochemical Reduction of Dioxygen. *Anal. Chem.*, 54:1720–1724, 1982.

[120] C. P. Andrieux, P. Hapiot, and J. M. Savéant. Mechanism of Superoxide Ion Disproportionation in Aprotic Solvents. *J. Am. Chem. Soc.*, 109:3768–3775, 1987.

[121] P. S. Singh. *The Electrochemical Reduction of Superoxide in Acetonitrile: A Concerted Proton-Coupled Electron Transfer (PCET) Reaction.* . Phd, University of Arizona, 2005.

[122] Y. G. Zhu, Q. Liu, Y. Rong, H. Chen, J. Yang, C. Jia, L. Yu, A. Karton, Y. Ren, X. Xu, S. Adams, and Q. Wang. Proton enhanced dynamic battery chemistry for aprotic lithium–oxygen batteries. *Nature Comm.*, 8:14308, 2017.

[123] A. E. Torres and P. B. Balbuena. Exploring the LiOH Formation Reaction Mechanism in Lithium-Air Batteries. *Chem. Mater.*, 30:708–717, 2018.

[124] J. Staszak-Jirkovský, R. Subbaraman, D. Strmcnik, K. L. Harrison, C. E. Diesendruck, R. Assary, O. Frank, L. Kobr, G. K. H. Wiberg, B. Genorio, J. G. Connell, P. P. Lopes, V. R. Stamenkovic, L. Curtiss, J. S. Moore, K. R. Zavadil, and N. M. Markovic. Water as a Promoter and Catalyst for Dioxygen Electrochemistry in Aqueous and Organic Media . *ACS Catal.*, 5:6600–6607, 2015.

[125] E. Nasybulin, W. Xu, M. H. Engelhard, Z. Nie, S. D. Burton, L. Cosimbescu, M. E. Gross, and J. G. Zhang. Effects of Electrolyte Salts on the Performance of Li-O_2 Batteries. *J. Phys. Chem. C*, 117:2635–2645, 2013.

[126] D. Chalasani and B. L. Lucht. Reactivity of Electrolytes for Lithium-Oxygen Batteries with Li_2O_2. *ECS Electrochemistry Letters*, 1(2):A38–A42, 2015.

[127] V. S. Bryantsev, V. Giordani, W. Walker, M. Blanco, S. Zecevic, K. Sazaki, J. Uddin, D. Addison, and G. V. Chase. Predicting Solvent Stability in Aprotic Electrolyte Li-Air Batteries: Nucleophilic Substitution by the Superoxide Anion Radical ($O_2^{\bullet -}$). *J. Phys. Chem. A*, 115:12399–12409, 2011.

[128] N. Kumar, M. D. Radin, B. C. Wood, T. Ogitsu, and D. J. Siegel. Surface-Mediated Solvent Decomposition in Li-Air Batteries: Impact of Peroxide and Superoxide Surface Terminations. *J. Phys. Chem. C*, 119:9050–9060, 2015.

[129] R. S. Assary, K. C. Lau, K. Amine, Y. K. Sun, and L. A. Curtiss. Interactions of Dimethoxy Ethane with Li_2O_2 Clusters and Likely Decomposition Mechanisms for Li-O_2 Batteries. *J. Phys. Chem. C*, 117:8041–8049, 2013.

[130] L. J. Rendek, G. S. Chottiner, and D. A. Scherson. Reactivity of Lithium toward Propylene Carbonate: Infrared Reflection Absorption Spectroscopy Studies in Ultrahigh Vacuum. *Langmuir*, 17:849–851, 2001.

[131] L. J. Rendek, G. S. Chottiner, and D. A. Scherson. The Reactivity of Linear Alkyl Carbonates toward Metallic Lithium: X-Ray Photoelectron Spectroscopy Studies in Ultrahigh Vacuum. *Journal of the Electrochemical Society*, 149(10):E408–E412, 2002.

[132] S. A. Freunberger, Y. Chen, Z. Peng, J. M. Griffin, L. J. Hardwick, F. Bardé, P. Novák, and P. G. Bruce. Reactions in the Rechargeable Lithium-O_2 Battery with Alkyl Carbonate Electrolytes. *J. Am. Chem. Soc.*, 133:8040–8047, 2011.

[133] J. M. Garcia, H. W. Horn, and J. E. Rice. Dominant Decomposition Pathways for Ethereal Solvents in Li-O_2 Batteries. *J. Phys. Chem. Lett*, 6:1795–1799, 2015.

[134] S. Das, J. Højberg, K. B. Knudsen, R. Younesi, P. Johansson, P. Norby, and T. Vegge. Instability of Ionic Liquid-Based Electrolytes in Li-O_2 Batteries. *J. Phys. Chem. C.*, 119:18084–18090, 2015.

[135] M. Piana, J. Wandt, S. Meini, I. Buchberger, N. Tsiouvaras, and H. A. Gasteiger. Stability of a Pyrrolidinium-Based Ionic Liquid in Li-O_2 Cells. *Journal of the Electrochemical Society*, 161(14):A1992–A2001, 2014.

[136] N. Xiao, R. T. Rooney, A. A. Gewirth, and Y. Wu. The Long-Term Stability of KO_2 in K-O_2 Batteries. *Angew. Chem.*, 130:1241–1245, 2018.

[137] S. S. Zhang and J. Read. Partially fluorinated solvent as a co-solvent for the non-aqueous electrolyte of Li/air battery. *Journal of Power Sources*, 196:2867–2870, 2011.

[138] P. J. Hore. *Nuclear Magnetic Resonance: Second Edition*. Oxford University Press, Oxford, UK, 2015.

[139] T. Liu, M. Leskes, W. Yu, A. J. Moore, L. Zhou, P. M. Bayley, G. Kim, and C. P. Grey. Cycling Li-O_2 batteries via LiOH formation and decomposition. *Science*, 350:530–534, 2015.

[140] V. Viswanathan, K. S. Thygesen, J. S. Hummelshøj, J. K. Nørskov, G. Girishkumar, B. D. McCloskey, and A. C. Luntz. Electrical conductivity in Li_2O_2 and its role in determining capacity limitations in non-aqueous $Li-O_2$ batteries. *J. Chem. Phys.*, 135:214704, 2011.

[141] F. Tian, M. D. Radin, and D. J. Siegel. Enchanced Charge Transport in Amorphous Li_2O_2. *Chem. Mater.*, 26:2952–2959, 2014.

[142] Y. Yang and D. J. Siegel. Intrinsic Conductivity in Sodium-Air Battery Discharge Phases: Sodium Superoxide vs Sodium Peroxide. *Chem. Mater.*, 27:3852–3860, 2015.

[143] M. D Radin and D. J. Siegel. Charge transport in lithium peroxide: relevance for rechargeable metal-air batteries. *Energy Environ. Sci.*, 6:2370–2378, 2013.

[144] R. B. Araujo, S. Chakraborty, and R. Ahuja. Unveiling the charge migration mechanism in Na_2O_2: implications for sodium-air batteries. *Phys. Chem. Chem. Phys.*, 17:8203–8209, 2015.

[145] B. Lee, D. H. Seo, H. D. Lim, I. Park, K. Y. Park, J. Kim, and K. Kang. First-Principles Study of the Reaction Mechanism in Sodium-Oxygen Batteries. *Chem. Mater*, 24:1048–1055, 2015.

[146] O. Gerbig, R. Merkle, and J. Maier. Electron and Ion Transport in Li_2O_2. *Adv. Funct. Mater*, 25:3129–3133, 2013.

[147] J. B. Varley, V. Viswanathan, J. K. Nørskov, and A. C. Luntz. Lithium and oxygen vacancies and their role in Li_2O_2 charge transport in Li-O_2 batteries. *Energy Environ. Sci.*, 7:720–727, 2014.

[148] B. Lee, J. Kim, G. Yoon, H. D. Lim, I. S. Choi, and K. Kang. Theoretical Evidence for Low Charging Overpotentials of Superoxide Discharge Products in Metal-Oxygen Batteries. *Chem. Mater*, 27:8406–8413, 2015.

[149] M. D Radin, J. F. Rodriguez, F. Tian, and D. J. Siegel. Lithium Peroxide Surfaces are Metallic, While Lithium Oxide Surfaces Are Not. *J. Am. Chem. Soc.*, 134:1093–1103, 2012.

[150] O. Gerbig, R. Merkle, and J. Maier. Electrical Transport and Oxygen Exchange in the Superoxides of Potassium, Rubidium, and Cesium. *Adv. Funct. Mater*, 25:2552–2563, 2015.

[151] O. Arcelus, C. Li, T. Rojo, and J. Carrasco. Electronic Structure of Sodium Superoxide Bulk, (100) Surface, and Clusters using Hybrid Density Functional: Relevance for Na-O_2 Batteries. *J. Phys. Chem. Lett.*, 6:2027–2031, 2015.

[152] H. G. Smith, R. M. Nicklow, L. J. Raubenheimer, and M. K. Wilkinson. Study of the Electrochemical Reduction of Dioxygen in Acetonitrile in the Presence of Weak Acids. *J. App. Phys.*, 3(37):1047–1049, 1966.

[153] Y. Zhang, Q. Cui, X. Zhang, W. C. McKee, Y. Xu, S. Ling, H. Li, G. Zhong, Y. Yang, and Z. Peng. Amorphous Li_2O_2: Chemical Synthesis and Electrochemical Properties. *Angew. Chem. Int. Ed.*, 55:10717–10721, 2016.

[154] B. M. Gallant, D. G. Kwabi, R. R. Mitchell, J. Zhou, C. V. Thompson, and Y. Shao-Horn. Influence of Li_2O_2 morphology on oxygen reduction and evolution kinetics in Li-O_2 batteries. *Energy Environ. Sci.*, 6:2518–2528, 2013.

[155] J. S. Hummelshøj, J. Blomqvist, S. Datta, T. Vegge, J. Rossmeisl, K. S. Thygessen, A. C. Luntz, K. W. Jacobsen, and J. K. Nørskov. Elementary oxygen electrode reactions in the aprotic Li-air battery. *J. Chem. Phys*, 132:071101, 2010.

[156] A. Khetan, A. Luntz, and V. Viswanathan. Trade-Offs in Capacity and Rechargeability in Nonaqueous Li-O_2 Batteries: Solution-Driven Growth versus Nucleophilic Stability. *J. Phys. Chem. Lett*, 6:1254–1259, 2015.

[157] D. M. Itkis, D. A. Semenenko, E. Y. Kataev, A. I. Belova, V. S. Neudachina, A. P. Sirotina, M. Hävecker, D. Teschner, A. Knop-Gericke, P. Dudin, A. Barinov, E. A. Goodilin, Y. Shao-Horn, and L. V. Yashina. Reactivity of Carbon in Lithium-Oxygen Battery Positive Electrodes. *Nano Lett.*, 13:4697–4701, 2013.

[158] Y. Xu and W. A. Shelton. Oxygen Reduction by Lithium on Model Carbon and Oxidized Carbon Structures. *Journal of the Electrochemical Society*, 158(10):A1177–A1184, 2011.

[159] R. Black, S. H. Oh, J. Lee, T. Yim, B. Adams, and L. F. Nazar. Screening for Superoxide Reactivity in Li-O_2 Batteries: Effect on Li_2O_2/LiOH Crystallization. *J. Am. Chem. Soc.*, 134:2902–2905, 2012.

[160] J. M. Garcia-Lastra, J. S. G. Myrdal, R. Christensen, K. S. Thygesen, and T. Vegge. DFT+U Study of Polaronic Conduction in Li_2O_2 and Li_2CO_3: Implications for Li-Air Batteries. *J. Phys. Chem. C*, 117:5568–5577, 2013.

[161] Y. S. Mekonnen, K. B. Knudsen, J. S. G. Mýrdal, R. Younesi, J. Højberg, J. Hjelm, P. Norby, and T. Vegge. Communication: The influence of CO_2 poisoning on overvoltages and discharge capacity in non-aqueous Li-Air batteries. *J. Chem. Phys*, 140:121101, 2010.

[162] H. Baltruschat. Differential Electrochemical Mass Spectrometry. *J. Am. Soc. Mass Spectrom.*, 15:1693–1706, 2004.

[163] S. J. Ashton. *Design, Construction and Research Application of a Differential Electrochemical Mass Spectrometer (DEMS)*. Phd, University of Copenhagen, 2012.

[164] B. D. McCloskey, D. S. Bethune, R. M. Shelby, G. Girishkumar, and Luntz A. C. Solvents' Critical Role in Nonaqueous Lithium-Oxygen Battery Electrochemistry . *J. Phys. Chem. Lett.*, 2:1161–1166, 2011.

[165] D. Oh, K. Virwani, L. Tadesse, M. Jurich, N. Aetukuri, L. E. Thompson, H. C. Kim, and D. S. Bethune. Effect of Transition Metal Oxide Cathodes on the Oxygen Evolution Reaction in Li-O_2 Batteries. *J. Phys. Chem. C*, 121:1404–1411, 2017.

[166] B. D. McCloskey, A. Spiedel, R. Scheffler, D. C. Miller, V. Viswanathan, J. S. Hummelshøj, J. K. Norskøv, and Luntz A. C. Twin Problems of Interfacial Carbonate Formation in Nonaqueous Li-O_2 Batteries. *J. Phys. Chem. Lett.*, 3:3045–3047, 2012.

[167] W. Weppner and R. A. Huggins. Electrochemical Methods for Determining Kinetic Properties of Solids. *Ann. Rev. Mater. Sci.*, 22:269–311, 2012.

[168] S. Xu, Y. Lu, H. D. Wang, H. Abruña, and L. A. Archer. A rechargeable Na-CO_2/O_2 battery enabled by stable nanoparticle hybrid electrolytes. *J. Mater. Chem. A*, 2:17723, 2014.

[169] S. Y. Sayed, K. P. C. Yao, D. G. Kwabi, T. P. Batcho, C. V. Amanchukwu, S. Feng, C. V. Thompson, and Y. Shao-Horn. Revealing instability and irreversibility in nonaqueous sodium-O_2 battery chemistry. *Chem. Commun.*, 52:9691, 2016.

[170] J. Zhu, X. Ren, J. Liu, W. Zhang, and Z. Wen. Unraveling the Catalytic Mechanism of Co_3O_4 for the Oxygen Evolution Reaction in a Li-O_2 Battery. *ACS Catal.*, 8:73–81, 2015.

[171] L. Lu, X. Han, J. Li, J. Hua, and M. Ouyang. A review on the key issues for lithium-ion battery management in electric vehicles. *Journal of Power Sources*, 226:272–288, 2013.

[172] Y. C. Lu and Y. Shao-Horn. Probing the Reaction Kinetics of the Charge Reactions of Nonaqueous Li-O_2 Batteries. *J. Phys. Chem. Lett.*, 4:93–99, 2013.

[173] Y. C. Lu, E. J. Crumlin, G. M. Veith, J. M. Harding, E. Mutoro, L. Baggetto, N. J. Dudney, Z. Liu, and Y. Shao-Horn. In Situ Ambient Pressure X-ray Photoelectron Spectroscopy Studies of Lithium-Oxygen Redox Reactions. *Nature Scientific Reports*, 2:715, 2012.

[174] J. L. Shui, J. S. Okasinski, C. Chen, J. D. Almer, and D. J. Liu. In Operando Spatiotemporal Study of Li_2O_2 Grain Growth and its Distribution Inside Operating Li-O_2 Batteries . *Chem. Sus. Chem*, 7:543–548, 2014.

[175] Z. Li, S. Ganapthy, Y. Xu, J. R. Heringa, Q. Zhu, W. Chen, and M. Wagemaker. Understanding the Electrochemical Formation and Decomposition of Li_2O_2 and LiOH with Operando X-ray Diffraction . *Chem. Mater.*, 29:1577–1586, 2017.

[176] S. Ganapathy, J. R. Heringa, M. S. Anastasaki, B. D. Adams, M. van Hulzen, S. Basak, Z. Li, J. P. Wright, L. F. Nazar, N. H. van Dijk, and M. Wagemaker. Operando Nanobeam Diffraction to Follow the Decomposition of Individual Li_2O_2 Grains in a Nonaqueous Li-O_2 Battery . *J. Phys. Chem. Lett.*, 7:3388–3394, 2016.

[177] Y. Lu, H. A. Gasteiger, and Y. Shao-Horn. Catalytic Activity Trends of Oxygen Reduction Reaction for Nonaqueous Li-Air Batteries. *J. Am. Chem. Soc.*, 133:19048–19051, 2011.

[178] G. K. P. Dathar, W. A. Shelton, and Y. Xu. Trends in the Catalytic Activity of Transition Metals for the Oxygen Reduction Reaction by Lithium. *J. Phys. Chem. Lett*, 3:891–895, 2012.

[179] Y. Lu, Z. Xu, H. A. Gasteiger, K. Hamad-Schifferli, and Y. Shao-Horn. Platinum-Gold Nanoparticles: A Highly Active Bifunctional Electrocatalyst for Rechargeable Lithium-Air Batteries. *J. Am. Chem. Soc.*, 132:12170–12171, 2010.

[180] A. Débart, J. Bao, G. Armstrong, and P. G. Bruce. An O_2 cathode for rechargeable lithium batteries: The effect of a catalyst. *Journal of Power Sources*, 174:1177–1182, 2007.

[181] H. W. Park, D. U. Lee, M. G. Park, R. Ahmed, M. H. Seo, L. F. Nazar, and Z. Chen. Perovskite-Nitrogen-Doped Carbon Nanotube Composite as Bifunctional Catalysts for Rechargeable Lithium-Air Batteries. *ChemSusChem*, 8:1058–1065, 2015.

[182] A. Débart, A. J. Patterson, J. Bao, and P. G. Bruce. Alpha-MnO_2 Nanowires: A Catalyst for the O_2 Electrode in Rechargeable Lithium Batteries. *Angew. Chem. Int. Ed.*, 47:4521–4524, 2008.

[183] Z. Li, S. Ganapathy, Y. Xu, Q. Zhu, W. Chen, I. Kochetov, C. George, L. F. Nazar, and M. Wagemaker. Fe_2O_3 Nanoparticle Seed Catalysts Enhance Cyclability on Deep (Dis)charge in Aprotic Li-O_2 Batteries. *Adv. Energy. Mater.*, 8:1703513, 2018.

[184] W. Kwak, K. C. Lau, C. Shin, K. Amine, L. A. Curtiss, and Y. Sun. A Mo_2C/Carbon Nanotube Composite Cathode for Lithium-Oxygen Batteries with High Energy Efficiency and Long Cycle Life. *ACS Nano*, 9(4):4129–4137, 2015.

[185] V. Pande and V. Viswanathan. Criteria and Considerations for the Selection of Redox Mediators in Nonaqueous Li-O_2 Batteries . *ACS Energy Lett.*, 2:60–63, 2013.

[186] X. Gao, Y. Chen, L. Johnson, and P. G. Bruce. Promoting solution phase discharge in Li-O_2 batteries containing weakly solvating electrolyte solutions. *Nature Materials*, 15:882–888, 2016.

[187] Y. Chen, S. A. Freunberger, Z. Peng, O. Fontaine, and P. G. Bruce. Charging a Li-O_2 battery using a redox mediator. *Nature Chemistry*, 5:489–494, 2013.

[188] B. J. Bergner, A. Schürmann, K. Peppler, A. Garusch, and J. Janek. TEMPO: A Mobile Catalyst for Rechargeable Li-O_2 Batteries. *J. Am. Chem. Soc.*, 55:15054–15064, 2016.

[189] D. Kundu, R. Black, B. Adams, and L. F. Nazar. A Highly Active Low Voltage Redox Mediator for Enhanced Rechargeability of Lithium-Oxygen Batteries. *ACS Cent. Sci.*, 119:510–515, 2015.

[190] H. Lim, H. Song, J. Kim, H. Gwon, Y. Bae, K. Y. Park, J. Hong, H. Kim, T. Kim, Y. H. Kim, X. Lepró, R. Ovalle-Robles, R. H. Baughman, and K. Kang. Superior Rechargeability and Efficiency of Lithium-Oxygen Batteries: Hierarchical Air Electrode Architecture Combined with a Soluble Catalyst. *Angew. Chem.*, 126:4007–4012, 2014.

[191] I. Landa-Medrano, M. Olivares-Marin, B. Bergner, R. Pinedo, A. Sorrentino, E. Pereiro, I. Ruiz de Larramendi, J. Janek, T. Amine, K.and Rojo, and D. Tonti. Potassium Salts as Electrolyte Additives in Lithium-Oxygen Batteries. *J. Phys. Chem. C*, 121:3822–3829, 2017.

[192] S. Matsuda, Y. Kubo, K. Uosaki, and S. Nakanishi. Potassium Ions Promote Solution-Route Li_2O_2 Formation in the Positive Electrode Reaction of Li-O_2 Batteries . *J. Phys. Chem. Lett.*, 8:1142–1146, 2017.

[193] C. O. Laoire, S. Mukerjee, K. M. Abraham, E. J. Plichta, and M. A. Hendrickson. Influence of Nonaqueous Solvents on the Electrochemistry of Oxygen in the Rechargeable Lithium-Air Battery. *J. Phys. Chem. C*, 114:9178–9186, 2010.

[194] S. Sankarasubramanian, J. Seo, F. Mizuno, N. Singh, and J. Prakash. Elucidating the Oxygen Reduction Reaction Kinetics and the Origins of the Anomalous Tafel Behavior at the Lithium-Oxygen Cell Cathode. *J. Phys. Chem. C*, 121:4789–4798, 2017.

[195] J. B. Benziger, M. B. Satterfield, W. H. J. Hogarth, J. P. Nehlsen, and I. G. Kevrekidis. The power performance curve for engineering analysis of fuel cells. *Journal of Power Sources*, 155:272–285, 2006.

[196] L Wang, A. Husar, T. Zhou, and H. Liu. A parametric study of PEM fuel cell performances. *International Journal of Hydrogen Energy*, 28:1263–1272, 2003.

[197] J. R. Harding, Y. C. Lu, Y. Tsukada, and Y. Shao-Horn. Evidence of catalyzed oxidation of Li_2O_2 for rechargeable Li-air battery applications. *Phys. Chem. Chem. Phys*, 14:10540–10546, 2012.

[198] R. Wen, M. Hong, and H. R. Byon. In Situ AFM Imaging of Li-O_2 Electrochemical Reaction on Highly Oriented Pyrolytic Graphite with Ether-Based Electrolyte. *J. Am. Chem. Soc.*, 135:10870–10876, 2013.

[199] K. Roy, L. Artiglia, and J. A. van Bokhoven. Ambient Pressure Photoelectron Spectroscopy: Opportunities in Catalysis from Solids to Liquids and Introducing Time Resolution. *ChemCatChem*, 650:130–139, 2016.

[200] M. Sun, X. Li, Z. Tang, X. Wei, and Q. Chen. Constant-rate dissolution of InAs nanowires in radiolytic water observed by *in situ* liquid cell TEM. *Nanoscale*, 10:19733–19741, 2018.

[201] Z. Niu and Y. Li. Removal and Utilization of Capping Agents in Nanocatalysis. *Chem. Mater.*, 26(1):72–83, 2014.

[202] G. Tocci and A. Michaelides. Solvent-Induced Proton Hopping at a Water-Oxide Interface. *J. Phys. Chem. Lett.*, 5:474–480, 2014.

[203] S. Lau and L. A. Archer. Nucleation and Growth of Lithium Peroxide in the Li-O_2 Battery. *Nano Lett.*, 15:5995–6002, 2015.

[204] J. H. van der Merwe. Theoretical Considerations in Growing Uniform Epilayers. *Surface Science*, 1:77–86, 1993.

[205] S. Higuchi and Y. Nakanishi. The growth of Ge on a Te/Si(001) surface: surface catalytic epitaxy. *Surface Science Letters*, 254:L465–L468, 1991.

[206] R. J. Nichols, D. Schröder, and H. Meyer. An *in situ* scanning probe microscopy study of copper electrodeposition on conductive polypyrrole. *Electrochimica Acta*, 40(10):1479–1485, 1995.

[207] A. Clemenćon, A. T. Appapillai, S. Kumar, and Y. Shao-Horn. Atomic force microscopy studies of surface and dimensional changes in Li_xCoO_2 crystals during lithium de-intercalation. *Electrochimica Acta*, 52:4572–4580, 2007.

[208] M. R. Nellist, F. A. L. Laskowski, J. Qiu, H. Hajibabaei, K. Sivula, T. W. Hamann, and S. W. Boettcher. Potential-sensing electrochemical atomic force microscopy for in operando analysis of water-splitting catalysts and interfaces. *Nature Energy*, 3:46–52, 1997.

[209] L. Zhong, R. R. Mitchell, Y. Liu, B. M. Gallant, C. V. Thompson, J. Y. Huang, S. X. Mao, and Y. Shao-Horn. In Situ Transmission Electron Microscopy Observations of Electrochemical Oxidation of Li_2O_2. *Nano Lett.*, 13:2209–2214, 2013.

[210] O. W. Richardson. Nobel Lecture, 1929.

[211] H. J. Kreuzer. Physics and chemistry in high electric fields. *Surface Science*, 246:336–347, 1991.

[212] C. J. Rothfuss. *The Influence of High Electric Fields on Water and Methanol Surface Electrochemistry*. Phd, University of Washington, 2002.

[213] T. D. Pinkerton. *Fundamental Studies of the Effect of Electric Field on Water-Surface Chemistry*. Phd, University of Washington, 1998.

[214] R. H. Fowler and L. Nordheim. Electron Emission in Intense Electric Fields. *Proc. Roy. Soc. A.*, 119(781):173–181, 1928.

[215] E. W. Müller. Elektronenmikroskopische Beobachtungen von Feldkathoden. *Z. Physik*, 9(106):541–550, 1937.

[216] T. T. Tsong. *Atom-Probe Field Ion Microscopy*. Cambridge University Press, Cambridge, first edition, 1990.

[217] E. L. Murphy and R. H. Good Jr. Thermionic Emission, Field Emission, and the Transition Region. *Physical Review*, 102(6):1464–1473, 1956.

[218] D. L. Scovell. *Dielectric Properties and Ionization of Water in High Interfacial Electric Fields*. Phd, University of Washington, 1999.

[219] R. Gomer. *Field Emission and Field Ionization*. Harvard University Press, Cambridge, first edition, 1990.

[220] E. W. Müller. Das Feldionenmikroskop. *Z. Physik*, 1(131):136–142, 1951.

[221] E. W. Müller. Field Desorption. *Physical Review*, 102(3):618–624, 1956.

[222] R. Gomer and L. W. Swanson. Theory of Field Desorption. *Journal of Chemical Physics*, 38(7):1613–1629, 1963.

[223] E. W. Müller and T. T. Tsong. Field ion microscopy, field ionization and field evaporation. *Progress in Surface Science*, 4:1–139, 1974.

[224] V. K. Medvedev, Y. Suchorski, and J. H. Block. Lithium field desorption microscope: a new tool for surface investigations. *Ultramicroscopy*, 53:27–35, 1994.

[225] Y. Suchorski, V. K. Medvedev, J. H. Block, L. C. Wang, and H. J. Kreuzer. Field desorption of lithium. *Physical Review B*, 53(7):4109–4116, 1996.

[226] W. C. Wiley and I. H. McLaren. Time-of-Flight Mass Spectrometer with Improved Resolution. *Rev. Sci. Inst.*, 26(12):1150–1157, 1955.

[227] J. H. Block, H. J. Kreuzer, and L. C. Wang. Electrostatic field effects in surface reactivity: adsorption, dissociation and catalytic reaction of nitric oxide. *Surface Science*, 246:125–134, 1991.

[228] M. Kato and K. Tsuno. Numerical analysis of trajectories and aberrations of a Wien filter including the effect of fringing fields. *Nuclear Instruments and methods in Physics Research*, A298:296–320, 1990.

[229] D. L. Cocke and J. H. Block. Field Ion and Field Desorption Mass Spectrometry of Ionrganic Compounds. *Surface Science*, 70:363–391, 1978.

[230] E. M. Stuve. Ionization of water in interfacial electric fields: An electrochemical view. *Chemical Physics Letters*, 519-520:1–17, 2012.

[231] T. D. Pinkerton, D. L. Scovell, A. L. Johnson, B. Xia, V. Medvedev, and E. M. Stuve. Electric Field Effects in Ionization of Water-Ice Layers on Platinum. *Langmuir*, 15:851–856, 1999.

[232] D. L. Scovell, T. D. Pinkerton, B. A. Finlayson, and E. M. Stuve. The dielectric response of water in high electric fields: equilibrium water thickness and the field distribution. *Chemical Physics Letters*, 294:255–261, 1998.

[233] D. L. Scovell, T. D. Pinkerton, V. K. Medvedev, and E. M. Stuve. Phase transitions in vapor-deposited water under the influence of high surface electric fields. *Surface Science*, 457:365–376, 2000.

[234] C. J. Rothfuss, V. K. Medvedev, and E. M. Stuve. Temperature and field dependence of protonated water cluster emission from field adsorbed water layers on platinum. *Surface Science*, 501:169–181, 2002.

[235] C. J. Rothfuss, V. K. Medvedev, and E. M. Stuve. The influence of the surface electric field on water ionization: a two step dissociative ionization and desorption mechanism for water ion cluster emission from a platinum field emitter tip. *Journal of Electroanalytical Chemistry*, 554-555:133–143, 2002.

[236] C. J. Rothfuss, V. K. Medvedev, and E. M. Stuve. Cluster formation and distributions in field ionization of coadsorbed methanol and water on platinum. *Surface Science*, 10:666–682, 2018.

[237] G. F. Rempfer. Unipotential electrostatic lenses: Paraxial properties and aberration of focal length and focal point. *J. Appl. Phys*, 57(7):2385–2401, 1985.

[238] J. H. Block. Chemical Surface Reactions in the Presence of High Electric Fields. *CRC Critical Reviews in Solid State Sciences*, 6(2):133–157, 1976.

[239] H. Valdes-Espinosa, S. B. Adler, and E. M. Stuve. Characterization of Charge Reactions of Li-O_2 Battery Cathodes Studied with Field Ionization Methods. *ECS Transactions*, 85(13):303–313, 2018.

[240] Y. Zhang, X. Zhang, J. Wang, W. C. McKee, Y. Xu, and Z. Peng. Potential-Dependent Generation of O_2^- and LiO_2 and Their Critical Roles in O_2 Reduction to Li_2O_2 in Aprotic Li-O_2 Batteries. *J. Phys. Chem. C*, 120:3690–3698, 2016.

[241] D. Zhai, K. C. Lau, H. H. Wang, J. Wen, D. J. Miller, L. Lu, F. Kang, B. Li, W. Yang, J. Gao, E. Indacochea, L. A. Curtiss, and K. Amine. Interfacial Effects on Lithium Superoxide Disproportionation in Li-O_2 Batteries. *Nano Lett.*, 15:1041–1046, 2015.

[242] Y. Yang, T. Zhang, X. Wang, L. Chen, N. Wu, W. Liu, H. Lu, L. Xiao, L. Fu, and L. Zhuang. Tuning the Morphology and Crystal Structure of Li_2O_2: A Graphene Model Electrode Study for Li-O_2 Battery. *ACS Appl. Mater. Interfaces*, 8:21350–21357, 2016.

[243] Y. Yang, W. Liu, N. Wu, X. Wang, T. Zhang, L. Chen, R. Zeng, Y. Wang, J. Lu, L. Fu, L. Xiao, and L. Zhuang. Tuning the Morphology of Li_2O_2 by Noble and 3d metals: A Planar Model Electrode Study for Li-O_2 Battery. *ACS Appl. Mater. Interfaces*, 9:19800–19806, 2017.

[244] Hamamatsu Photonics KK. *Microchannel Plate Assembly Manual*. User manual, Hamamatsu Photonics Electron Division, 2006.

[245] E. M. Stuve, A. Krasnopoler, and D. E. Sauer. Relating the in-situ, ex-situ, and non-situ environments in surface electrochemistry. *Surface Science*, 335:177–185, 1995.

[246] J. Newman and K. Thomas-Alyea. *Electrochemical Systems*. Wiley-Interscience, Hoboken, NJ, third edition, 2004.

[247] N. Mahne, B. Schafzahl, C. Leypold, M. Leypold, S. Grumm, A. Leitgeb, G. A. Strohmeier, M. Wilkening, O. Fontaine, D. Kramer, C. Slugovc, S. M. Borisov, and S. A. Freunberger. Singlet oxygen generation as a major cause for parasitic reactions during cycling of aprotic lithium-oxygen batteries. *Nature Energy*, 2:17036, 2017.

[248] T. D. Poulsen, P. R. Ogilby, and K. V. Mikkelsen. Polarizabilities of the First Excited ($a^1\Delta_g$) and Ground ($X^3\Sigma_g^-$) States of Molecular Oxygen. *J. Phys. Chem. A*, 102:8970–8973, 1998.

[249] H. Valdes-Espinosa, S. B. Adler, and E. M. Stuve. Modeling Water Reduction on 10 Mole% Gadolinia-Doped Ceria (GDC10) Porous Electrodes . *ECS Transactions*, 65(2):229–251, 2015.

[250] H. Valdes-Espinosa, S. B. Adler, and E. M. Stuve. Modeling Water Reduction on Doped Ceria Thin Films . *ECS Transactions*, 68(1):3209–3228, 2015.

[251] S. Schiebahn, T. Grube, M. Robinius, V. Tietze, B. Kumar, and D.. Stolten. Power to gas: Technological overview, systems analysis and economic assessment for a case study in Germany. *International Journal of Hydrogen Energy*, 40:4285–4294, 2015.

[252] W. L. Becker, R. J Braun, M. Penev, and M. Melaina. Production of Fischer-Tropsch liquid fuels from high temperature solid oxide co-electrolysis units. *Energy*, 47:99–115, 2012.

[253] S. D. Ebbesen, J. Høgh, K. A. Nielsen, J. U. Nielsen, and M. Mogensen. Durable SOC stacks for production of hydrogen and synthesis gas by high temperature electrolysis. *International Journal of Hydrogen Energy*, 36:7363–7373, 2014.

[254] T. Nakamura, K. Yashiro, A. Kaimai, T. Otake, K. Sato, T. Kawada, and J. Mizusaki. Determination of the Reaction Zone in Gadolinia-Doped Ceria Anode for Solid Oxide Fuel Cell. *Journal of the Electrochemical Society*, 155(12):B1244–B1250, 2008.

[255] O. A. Marina, C. Bagger, S. Primdahl, and M. Mogensen. A solid oxide fuel cell with a gadolinia-doped ceria anode: preparation and performance. *Solid State Ionics*, 123:199–208, 1999.

[256] K. Yashiro, S. Onuma, A. Kaimai, Y. Nigara, T. Kawada, J. Mizusaki, K. Kawamura, T. Horita, and H. Yokokawa. Mass transport properties of $Ce_{0.9}Gd_{0.1}O_{2-\delta}$ at the surface and in the bulk. *Solid State Ionics*, 245:469–476, 2007.

[257] C. Zhang, Y. Yu, M. E. Grass, C. Dejoie, W. Ding, K. Gaskell, N. Jabeen, Y. P. Hong, A. Shavorskiy, H. Bluhm, W. Li, G. S. Jackson, Z. Hussain, Z. Liu, and B. W. Eichhorn. Mechanistic Studies of Water Electrolysis and Hydrogen Electro-Oxidation on High Temperature Ceria-Based Solid Oxide Electrochemical Cells . *J. Am. Chem. Soc.*, 135:11572–11579, 2013.

[258] Z. A. Feng, F. El Gabaly, X. Ye, Z. X. Shen, and W. C. Chueh. Fast vacancy-mediated oxygen ion incorporation across the ceria-gas electrochemical interface. *Nat. Commun.*, 5:4374, 2014.

[259] S. B. Adler. Factors Governing Oxygen Reduction in Solid Oxide Fuel Cell Cathodes. *Chem. Rev.*, 104:4791–4843, 2004.

[260] S. B. Adler, X. Y. Chen, and J. R Wilson. Mechanisms and rate laws for oxygen exchange on mixed-conducting oxide surfaces. *Journal of Catalysis*, 245:91–109, 2007.

[261] J. R. Wilson, D. T. Schwartz, and S. B. Adler. Nonlinear electrochemical impedance spectroscopy for solid oxide fuel cell cathode materials. *Electrochimica Acta*, pages 1389–1402.

[262] R. D. Green, C. C. Liu, and S. B. Adler. Carbon dioxide reduction on gadolinia-doped ceria cathodes. *Solid State Ionics*, 179:647–660, 2008.

[263] S. B. Adler, J. A. Lane, and B. C. H. Steele. Electrode Kinetics of Porous Mixed-Conducting Oxygen Electrodes. *Journal of the Electrochemical Society*, 143(11):3554–3564, 1996.

[264] J. R. Wilson, M. Sase, T. Kawada, and S. B. Adler. Measurement of Oxygen Exchange Kinetics on Thin-Film $La_{0.6}Sr_{0.4}CoO_{3-\delta}$ Using Nonlinear Electrochemical Impedance Spectroscopy. *Journal of the Electrochemical Society*, (5):B81–B86.

[265] Y. Lu, C. Kreller, and S. B. Adler. Measurement and Modeling of the Impedance Characteristics of Porpous $La_{1-x}Sr_xCo_{3-\delta}$ Electrodes. *Journal of the Electrochemical Society*, 156(4):B513–B525, 2009.

[266] L. Navarro, F. Marques, and J. Frade. n-Type Conductivity in Gadolinia-Doped Ceria. *Journal of the Electrochemical Society*, 144(1):267–273, 1997.

Appendix A

ELECTRONIC SCHEMATICS

The isolation box used to float the heating loop power supply was built between 1996 and 1997. At the time when the work in this project started, there were several failures that required extensive repairs. Also, the original schematics were not updated. This appendix includes the most recently upgraded electronic schematics for the isolation box and any repairs that took place. In addition, a list of recommendations are given for future construction of such an instrument.

A.1 List of isolation box repairs and modifications

1. *January 2016:* The voltage suppression diodes failed and were replaced

2. *February 2016:* Op-amps and V/F converters were replaced in the V/F conversion cards

3. *October 2016:* Chemistry Electronics Machine Shop replaced dried electrolytic capacitors

4. *March 2017:* Chemistry Electronics Machine Shop replaced dried electrolytic capacitors

5. *August 2017:* All $\pm$ 5 and 15 V connectors and multiple fiber optic connectors were caulked. Also, capacitors were introduced to the voltage and current control channels to block a 1 V, 60 Hz noise introduced by the isolation transformer.

A.2 Electronic diagrams/schematics

This section includes the most recent iteration (January 2018) of the circuit schematics. Also, a system diagram showing all ground and signal connections is included.

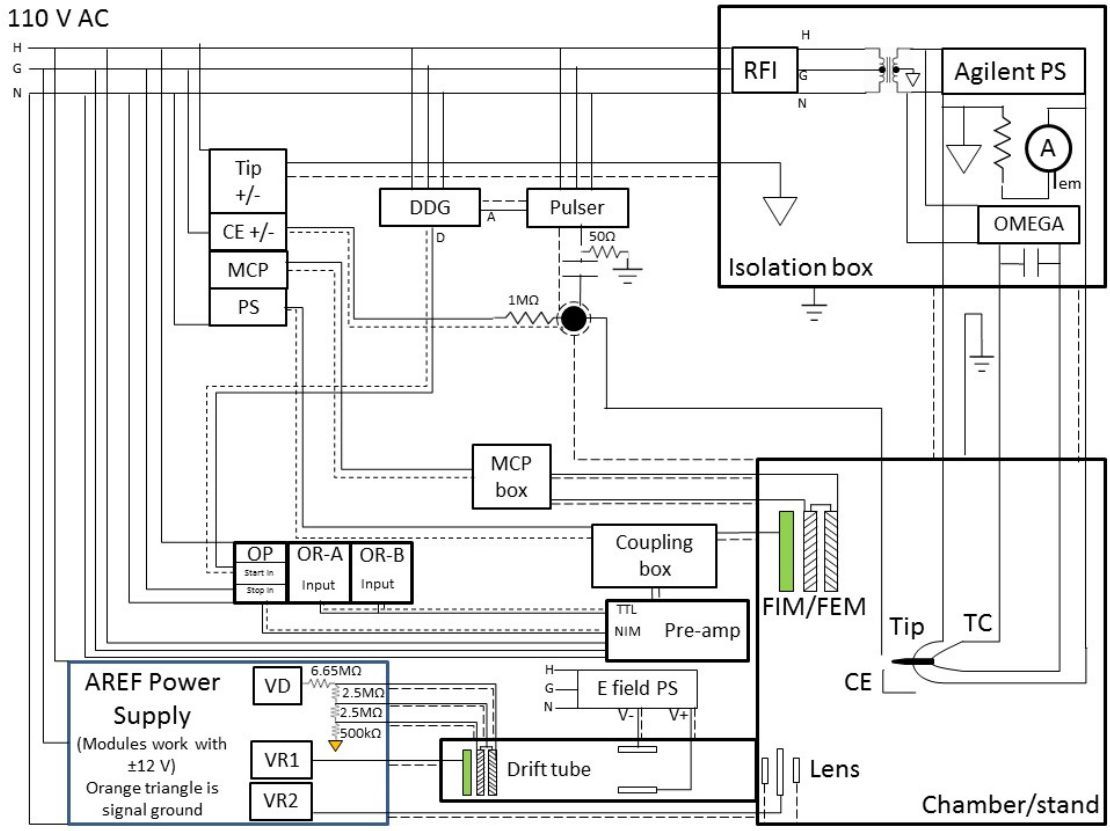

Figure A.1: System diagram. The signal connections are shown as solid lines, while shield connections are shown as dashed lines parallel to the solid lines. Chamber/stand configuration is altered from the actual configuration for clarity of the system diagram. The CE feedthrough is shown as a large, black circle

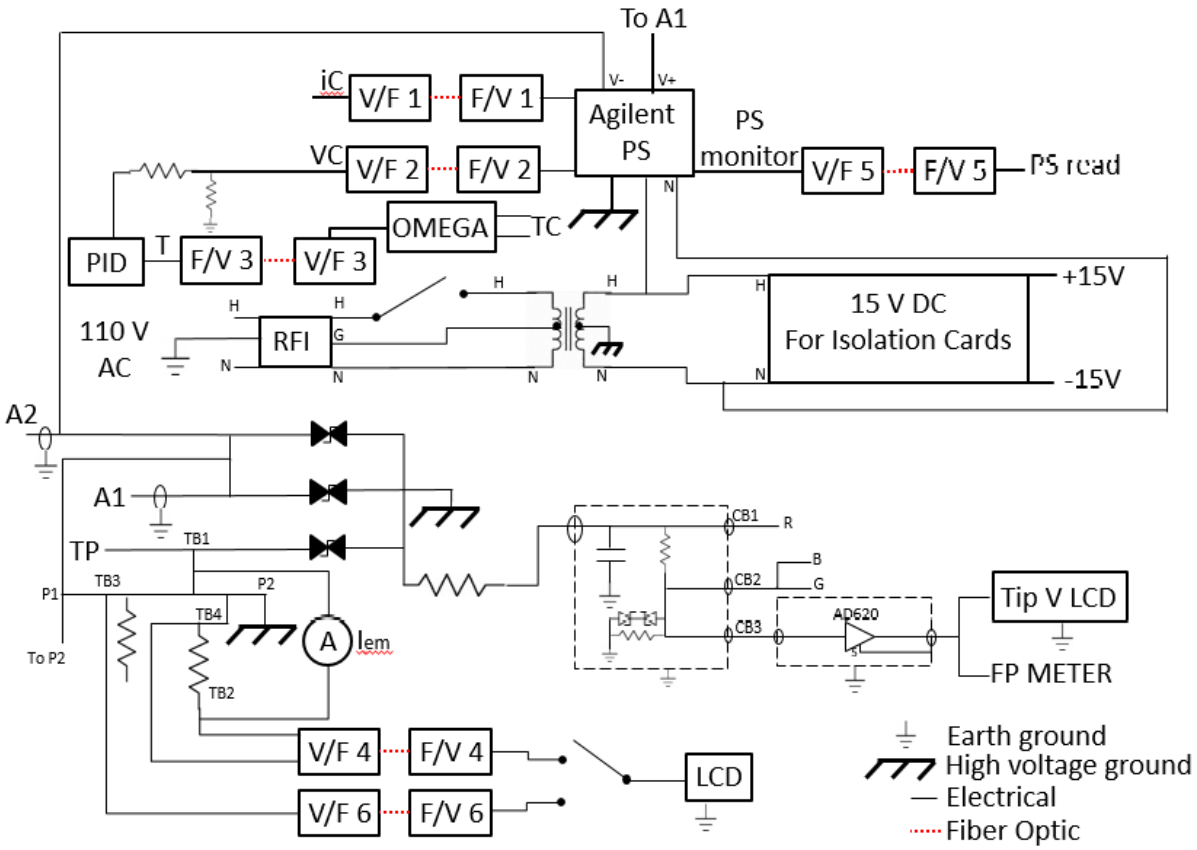

Key

V/F-Voltage-to-frequency	VC-Remote voltage control	PID-Temperature controller
F/V-Frequency-to-voltage	RFI-Radio Frequency Isolation	PS-Power Supply
iC-Remote current control	TP-Tip potential	I_{em}-Emission current

Figure A.2: Isolation box schematic. Electrical connections are shown as solid black lines, while fiber optic connections are shown as red dashed lines.

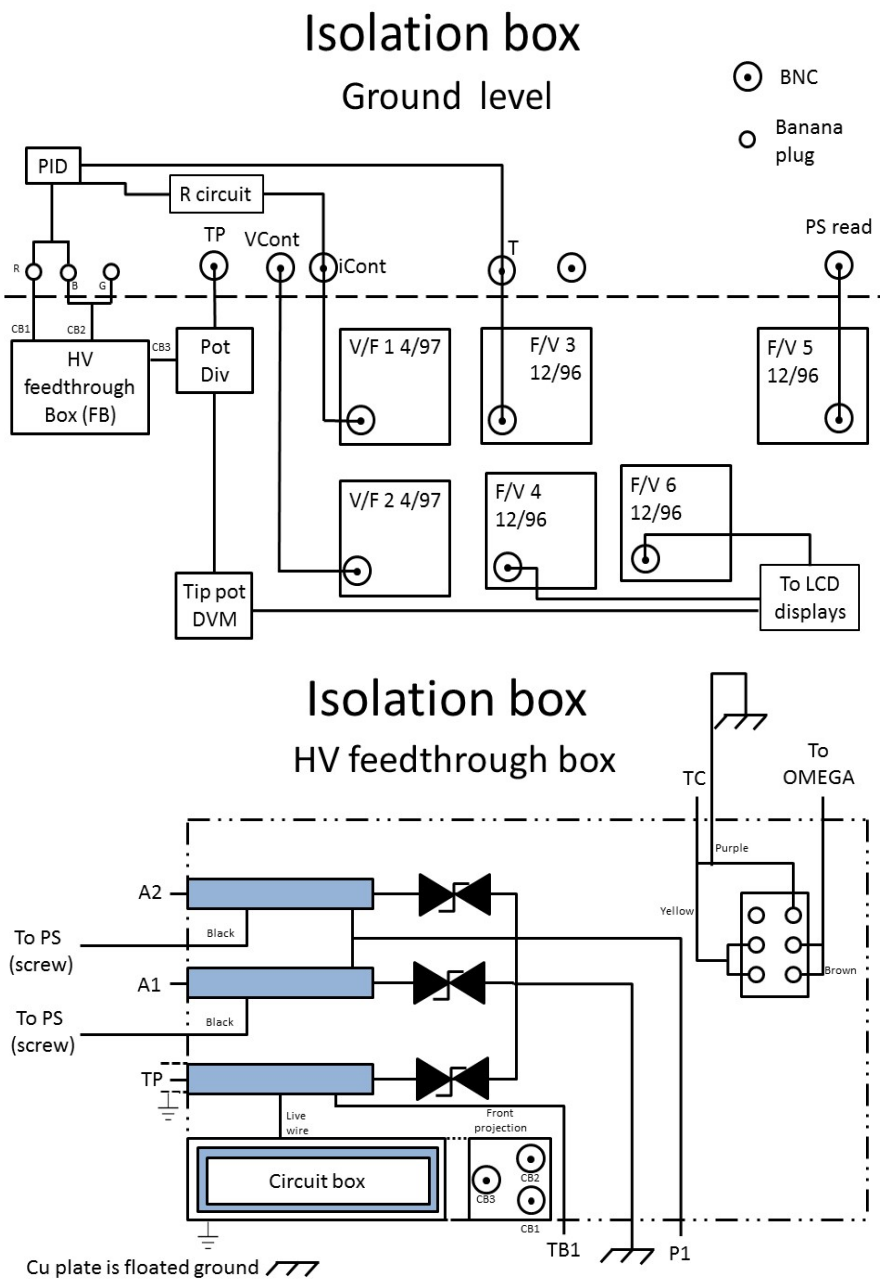

Figure A.3: Isolation box ground level

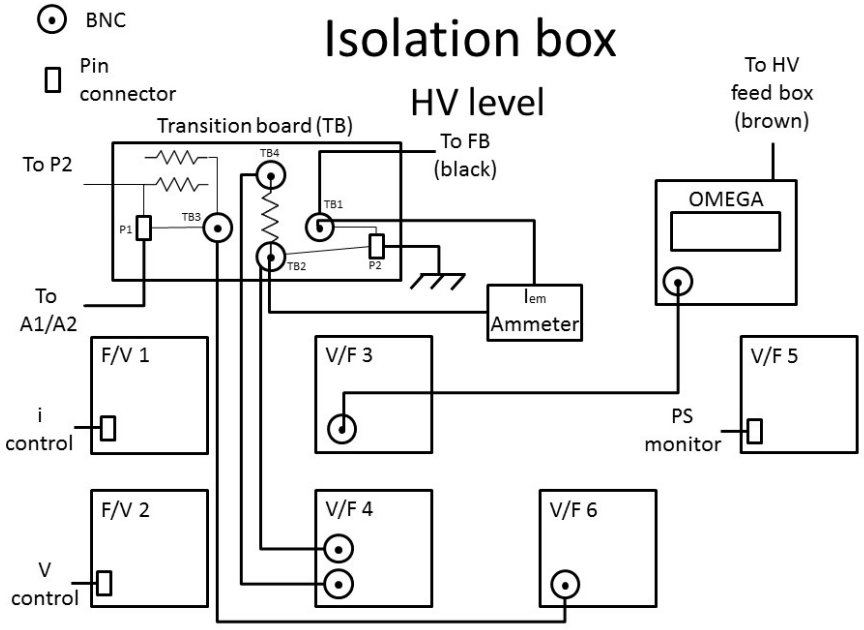

Figure A.4: Isolation box high voltage level

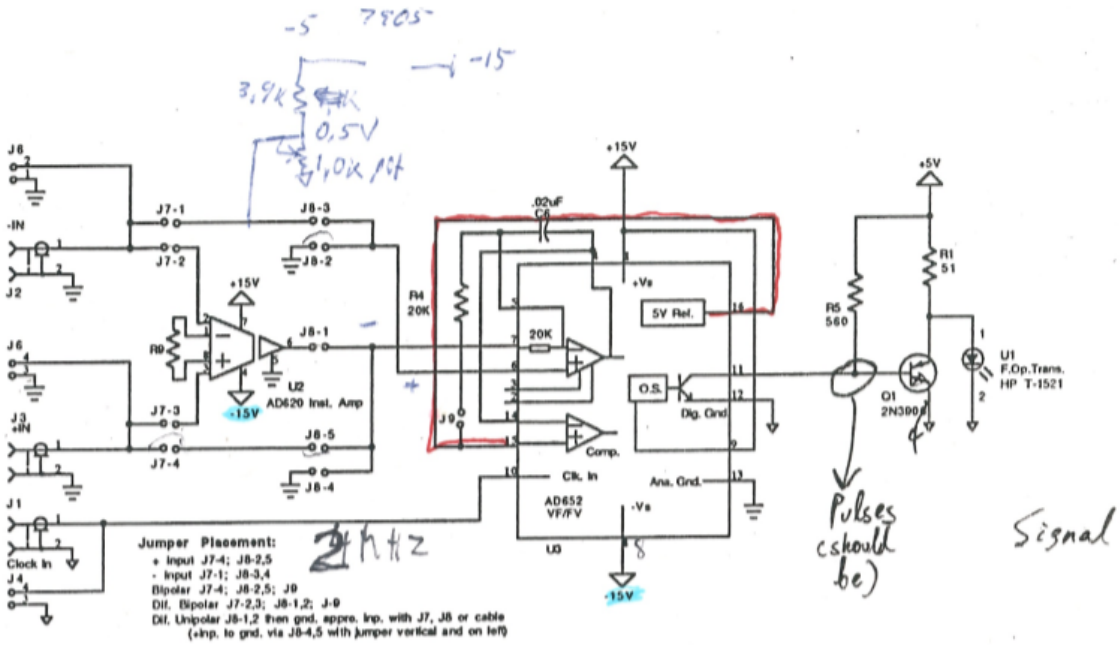

Figure A.5: Voltage-to-frequency card circuit

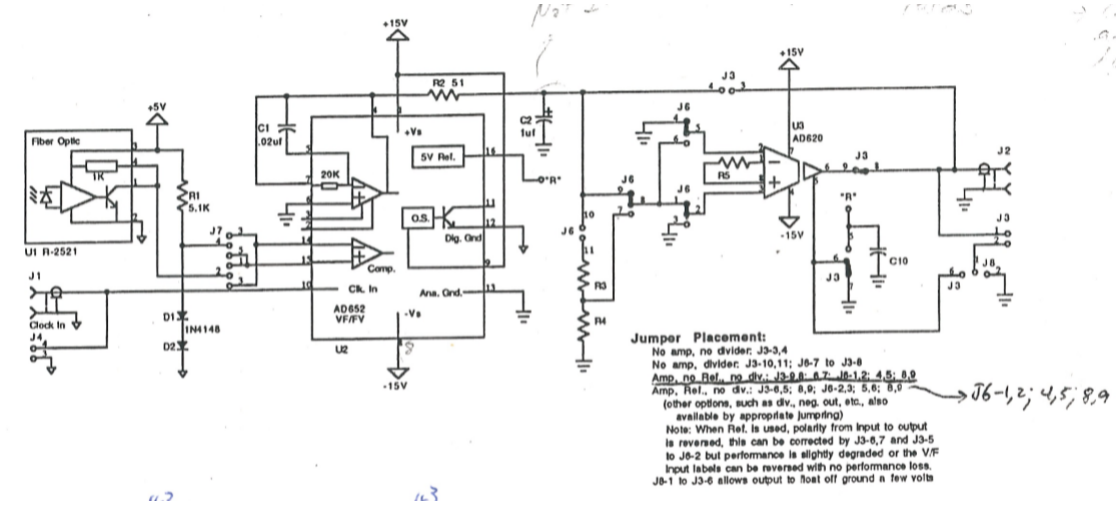

Figure A.6: Frequency-to-voltage card circuit

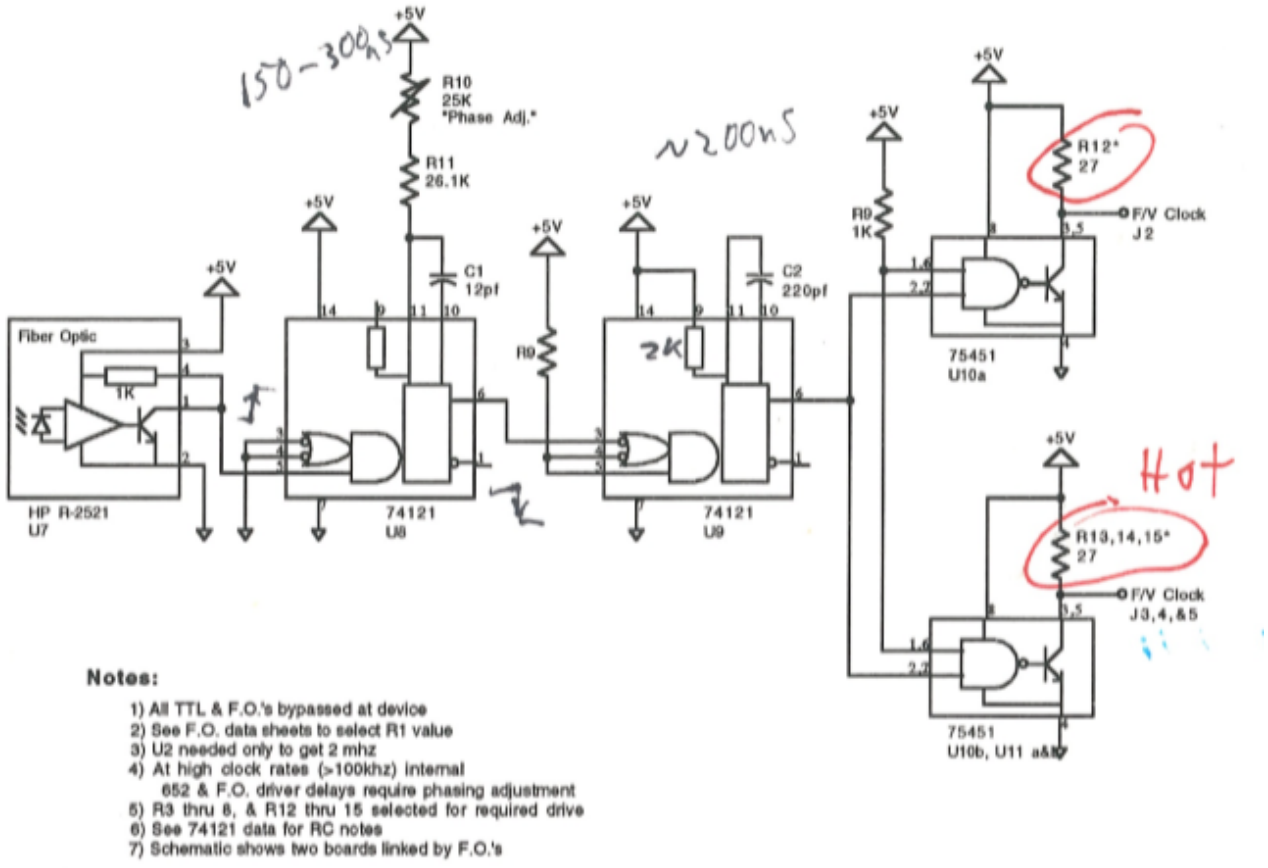

Figure A.7: Clock card circuit

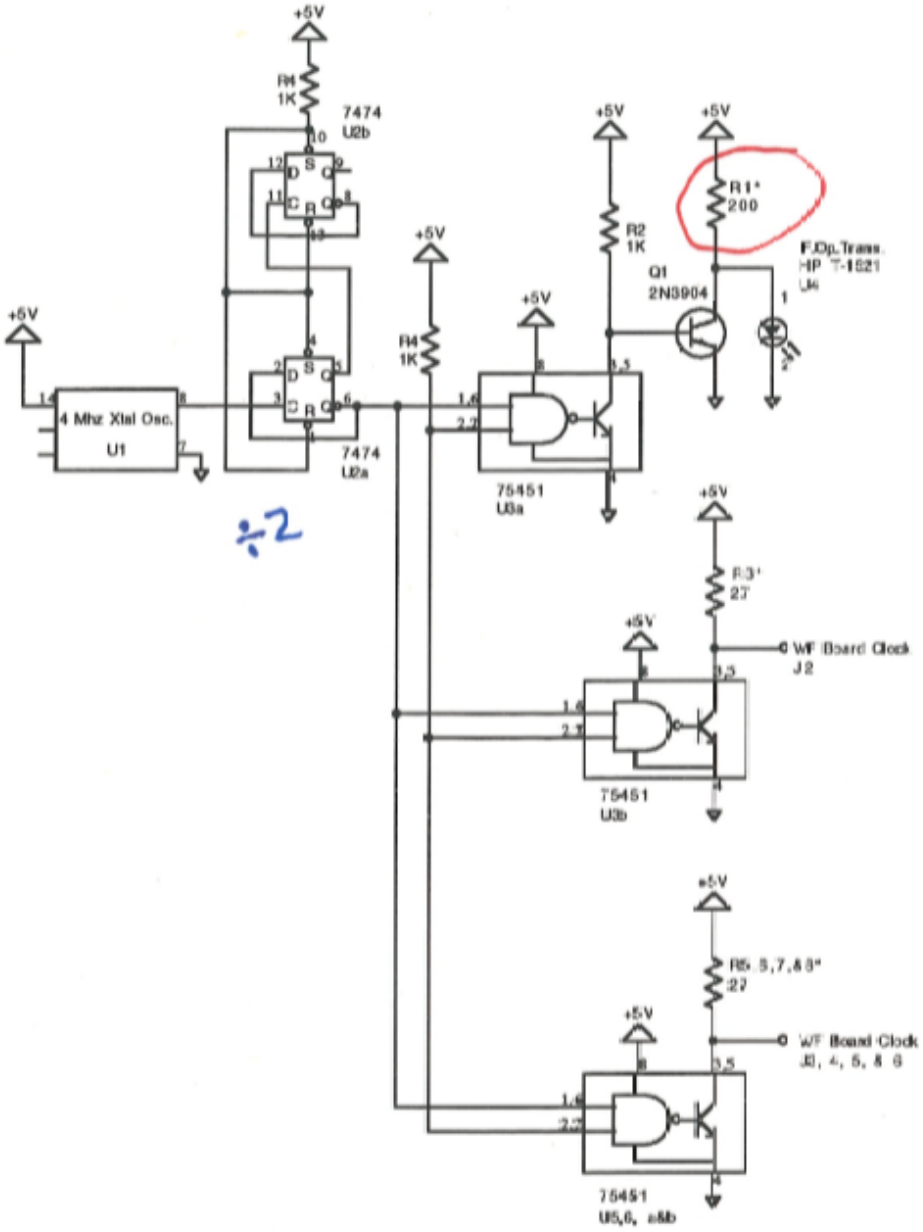

Figure A.8: Clock relay card circuit

A.3 Isolation box design considerations

Throughout this project, several isolation box failures occured due to the age of components or construction shortcuts. This section provides recommendations for construction of a new isolation. The biggest issues with the current box are the use of sliding connectors with no locking mechanism, the size of the box, and unnecessary clutter of connections.

1. Use locking connectors if building a box that needs to be wheeled. This would allow minimizing the possibility of connectors coming off and causing problems.

2. Use a better layout of the isolation cards to avoid wire crossover. Otherwise, try to build all circuits in two IC cards: one for earth ground and another for the floating ground.

3. Include a temperature controller in the box to avoid having to depend on an external controller and to avoid having a thermocouple reader inside of the box. This suggestion is mostly for keeping a cleaner construction and to avoid having extra connections that might add clutter.

Appendix B

EXPERIMENTAL PROCEDURES

B.1 Assembly and dissasembly instructions

B.1.1 Sample holder and transmission line

The sample holder is attached to the cooling finger

Dissasembly

1. Remove all side connections. These include the counterelectrode flange, thermocouple leads, and tip heating leads.

2. Tilt sample holder and place a box high enough to ensure that the liquid nitrogen inlet touches the table.

3. Loosen bolts holding the metal piece with the 4 nipples to the cooling finger. Once the bolts are removed, the metal piece should slide freely.

4. Remove metal piece with nippless.

Assembly

1. Place gasket on the upper end of the metal piece with the 4 nipples. This end is has a red marking on the side. Align flange correctly following red marks. The proper alignment is shown in Figure B.1.

2. Introduce temperature, counterelectrode, and tip heating leads into separate nipples.

3. Place a copper gasket on each nipple and connect the vacuum side leads to the feedthroughs. Make sure that the wires do not touch each other or the chamber. Place bolts at each of the feedthroughs and tighten finger tight.

4. Place bolts to connect the metal piece with feedhtroughs to the cooling finger and tighten finger tight.

B.1.2 Manipulator

1. Remove top mainpulator plate by loosening bolts.

2. Introduce temperature, counterelectrode, and tip heating leads into separate nipples.

3. Place 4 inch flanges and hold in place with bolts. Tighten finger tight. When connecting wires to feedthrough and assembling everything, make sure that the counterelectrode copper wire does not contact the chamber chassis. When doing experiments, such a short manifests when the counterelectrode voltage does not go above 600 V.

4. Place bolts in 6 inch flange and tighten finger tight.

B.1.3 Drift tube and Wien filter detector

1. Remove drift tube.

2. Remove flange connecting assembly to chamber.

3. Loosen screws holding lens to support rods. The screws are shown in inset 3 of Figure B.2.

4. Reassemble tube, starting with lens.

5. Connect big flange to chamber.

6. Add assembly to tube.

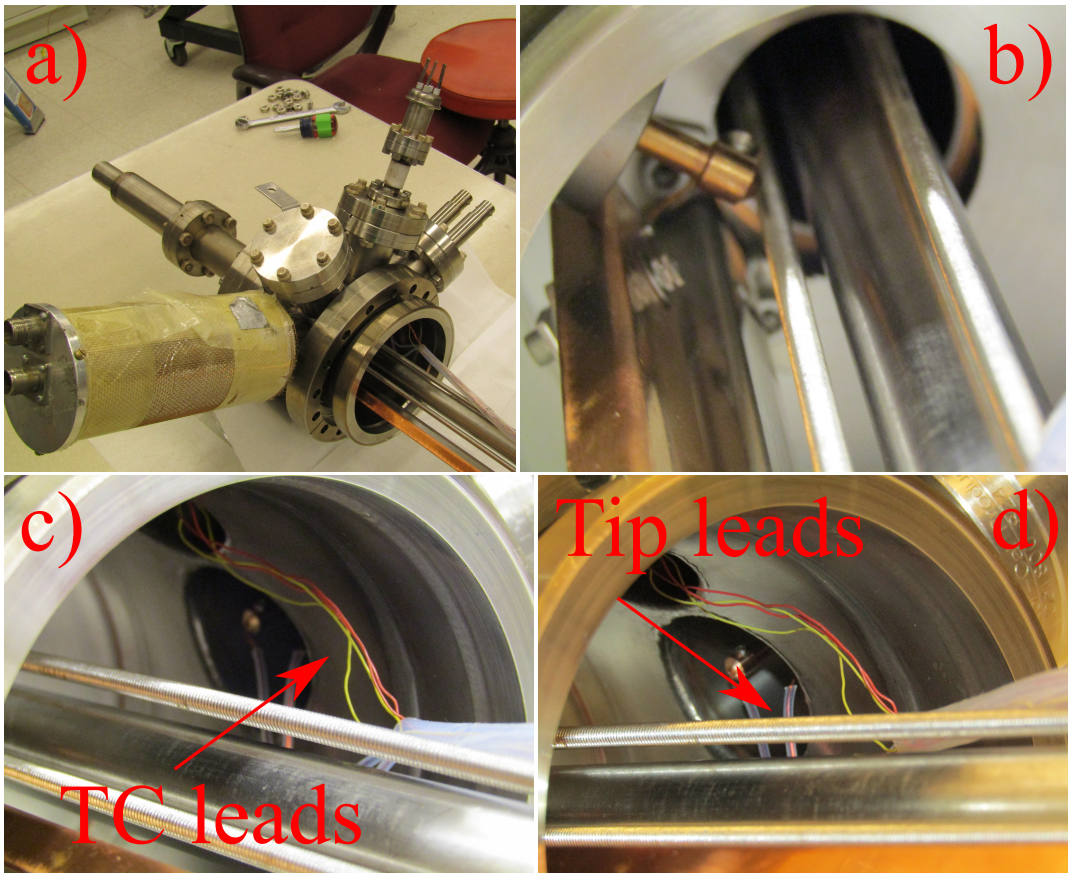

Figure B.1: Sample holder. Inset a) shows the feedthrough alignment, inset b) shows the counterelectrode connections from the inside, inset c) shows the thermocouple connections from the inside, and inset d) shows the tip heating feedthroughs from the inside.

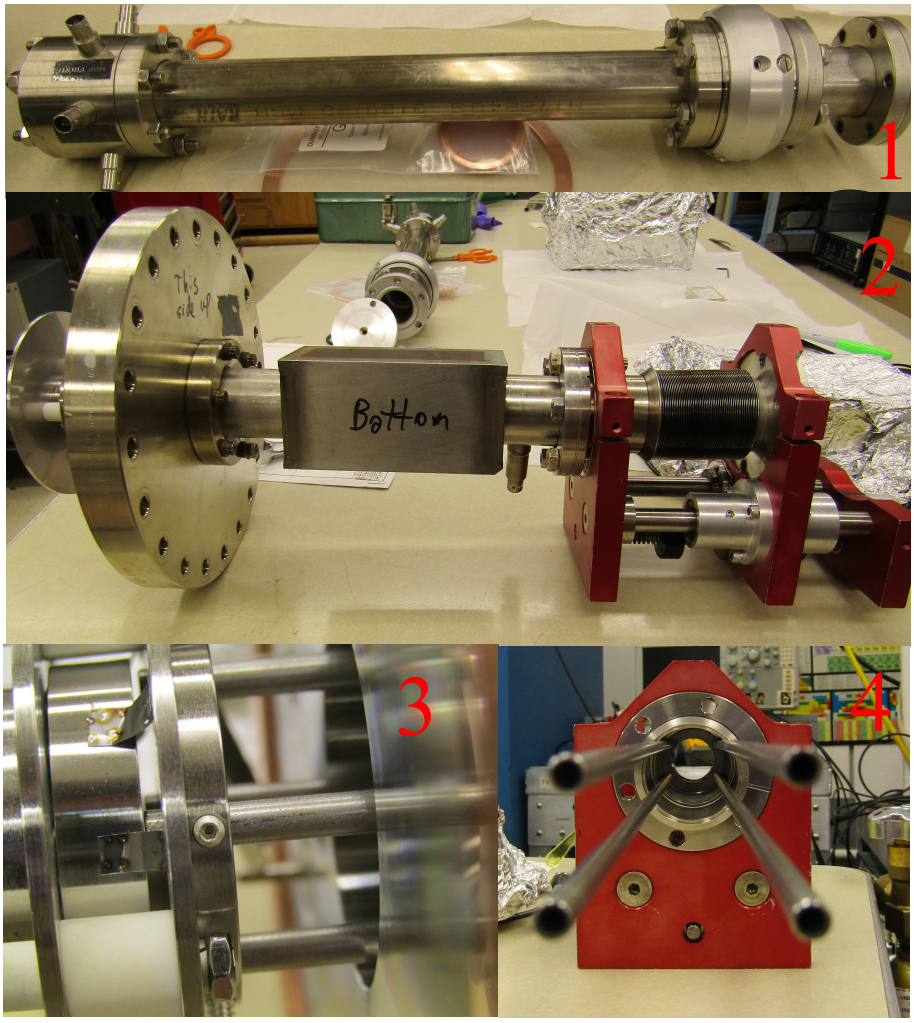

Figure B.2: Drift tube assembly process. The steps for drift tube assembly are labeled in the figure.

B.1.4 Imaging detector

Microchannel plate replacement

1. Remove the shielding plate.

2. Remove the grid.

3. Place assembly on the table as shown in inset 3) of Figure B.3. Otherwise, assembly becomes very complicated.

4. Dissassemble carefully, as the plate contacts are fragile.

5. Remove contact plates by loosening nuts with tweezers. Then, pull out the contact plate and top insulators.

6. Take out plates and replace. Make sure that the electrical contact (thin metal ring) is placed between both plates.

7. Reassemble.

The detector dissasembly process is shown in Figure B.3.

B.2 Experimental procedures

B.2.1 Tip making

Crucible preparation

- Apply a thin coating of high temperature cement to the crucible and let dry for 3 or 4 hours.

- Use thicker wire (AWG 20 or 22) and make support rings. Make two rings: one that goes around the upper part of the crucible and one that goes on the lower part of the crucible. Then coil remaining wire to make heating leads.

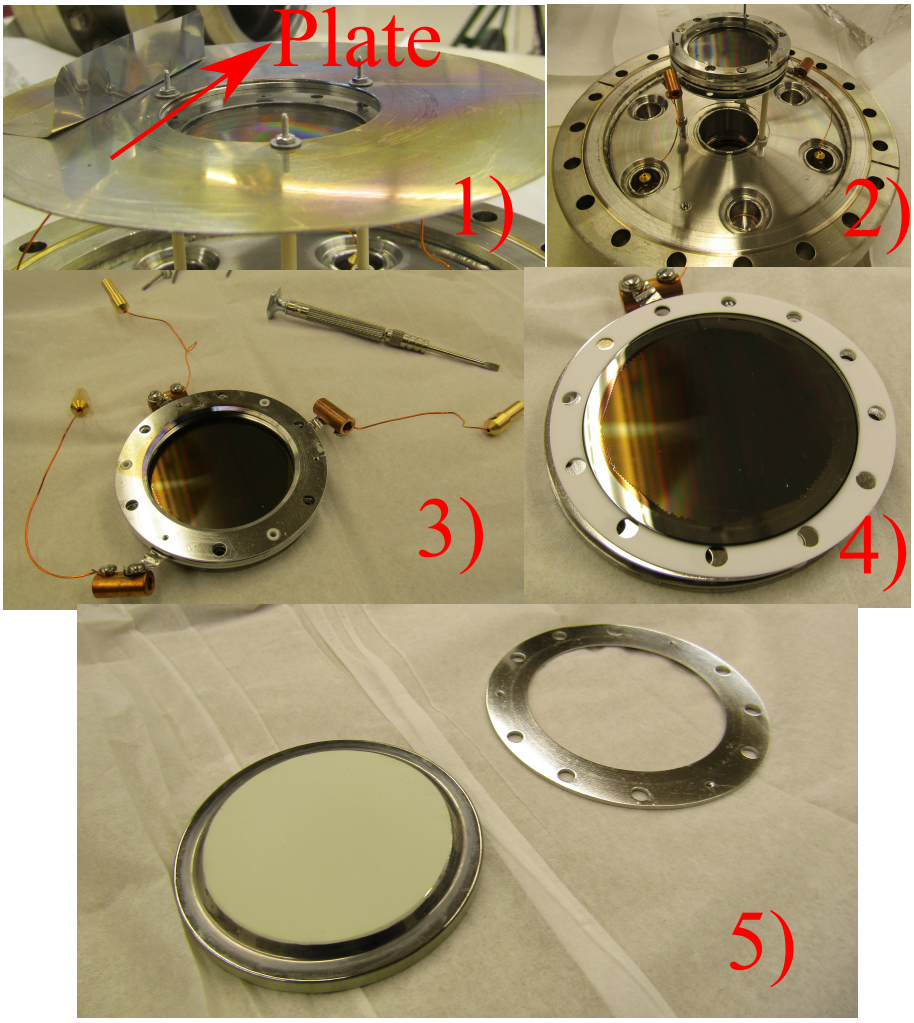

Figure B.3: Microchannel plate dissasembly process. The step numbers are shown in the figure.

- Make the heating element using nichrome. Wrap the nichrome around the heating lead and then wrap wire around the crucible while making sure that the loops do not touch each other. Also, the wire might coil back if not preworked.

- Apply a coating of cement to the coils and dry for 4 hours. Repeat at least twice.

- Once cement is dry, place a thermocouple at the bottom and wrap crucible with aluminum foil. Make sure that both leads do not short.

- **Note:** There is variability in the measured temperature at the bottom of the crucible and the actual salt mixture. Before etching tips, make a calibration curve comparing the actual salt temperature and the temperature measured at the bottom of the crucible.

Tip making

- Place salt mixture inside of crucible.

- Apply AC current to heating coil. Voltages under 35 V AC are typically needed.

- Once salt reaches appropriate temperature, place tip wire on the red lead and some heating loop wire (about 1 cm) on the black lead.

- Introduce black lead to melt and then turn on power supply. Make sure that box in on continuous mode rather than pulse.

- Introduce tip wire to the melt. Make sure that wire does not go all the way in.

- Etch tip for about 20-30 s. Inspect tip under the microscope and use shorter dunks to sharpen as needed.

B.2.2 Sample mounting

Spot welding specifications

- **Heating loop wire:** 0.25 mm diameter platinum wire (1" long). Before welding, curl the wire using a pen.
- **Thermocouple:** 0.08 mm diameter chromel/alumel wire (2" long). Note: Make alumel (red) wire shorter. Also, make sure that the wire is curled to an M shape to allow for easy mounting.
- **Procedure**
  - Hold loop in place using clip electrode (round plate with a black metal clip that holds sample in contact with a copper plate). When spot welding, make use the thicker wire is always on top.
  - Use fine tip electrode and make contact between parts to join
  - Use 4 % power and send pulse by pressing pedal.
  - Place thermocouple junction below tip. Make sure that the red wire is on the left side.
  - Use fine tip electrode and make contact between the parts to weld. Use 1.2% power to create the weld.

Mounting sample in holder

1. Loosen Macor insulation holding CE plate in place and remove plate
2. Loosen thermocouple connector screws with a hex wrench
3. Loosen heating loop holding screws with a hex wrench and remove tip
4. Place heating loop in holding plates and tighten the screws

5. Place thermocouple wire in the connectors and tighten the screws. Chromel goes on the yellow and alumel in red (note: alumel is magnetic). When mounting the tip, it helps to preshape the wires before mounting such that they can get into the feedthroughs without much trouble. Also, it helps to shorten the wires to avoid curling

6. Place the CE plate back in its original position and tighten the Macor insulator back in place. When tight, the plate should not rotate freely. The CE hole should be 1mm away from the tip. The sample holder might seem loose upon touching it, but it should hold by its own when not touching it. Tighten the insulator properly.

B.2.3 Solvent degassing

1. Prepare a clean vial by washing it with the appropriate solvent. Remove solvent by connecting the vial to vacuum pump. A heat gun may be used to speed the evaporation of the cleaning solvent.

2. After pumping away the cleaning solvent, close the valve on the sample vial. The vial should be clean and under vacuum.

3. Prepare a clean pipette or syringe to transfer the chemical.

4. Disconnect the vial from the vacuum manifold.

5. Using the pipette or syringe, transfer the desired amount of the chemical from the original container to the upper part of the sample vial.

6. Slowly open the valve to the lower part of the sample vial. Do not let all of the chemical flow into the bottom of the vial. Do not allow any air to flow into the bottom of the vial. Close the sample valve while leaving a small amount of the chemical in the upper part of the vial. This minimizes the amount of air contamination in the sample. Dispose of excess chemical from the upper part of the vial in the appropriate waste container.

7. Connect the vial filled with chemical to the vacuum manifold. Open the valve between the manifold and the sample vial to pump the air from the top of the sample vial. At this point, the valve on the sample vial remains closed. Prepare liquid nitrogen in a small container (a Styrofoam coffee cup works well).

8. Submerge the sample vial in liquid nitrogen until the chemical freezes. Open the valve to the vial for 5-10 seconds and then close the valve. Notice the pressure rise in the manifold as non-condensable gases are pumped away from the frozen sample.

9. Remove the liquid nitrogen and allow the chemical to thaw.

10. Repeat this process until the pressure rise after opening the sample vial valve during step 2 is negligible.

B.2.4 Tip imaging and cleaning

1. Ensure pressure is below 1×10^{-9} torr prior to performing FEM. If pressure is above that value, the image will be unstable and eventually the tip will fail.

2. Apply voltage to the MCPs and PS slowly.

3. Set tip voltage to negative power supply.

4. Slowly increase tip voltage until an image is visible. Record the applied voltage.

5. Reduce tip voltage to zero and turn off MCP/PS detector slowly.

6. Switch tip voltage to positive power supply and CE voltage to the negative power supply.

7. Leak 1×10^{-4} torr Ne into the chamber and wait one minute.

8. Slowly turn on MCP and PS voltages.

9. Slowly increase tip and CE voltage until an image becomes visible. Record voltage.

10. Keep increasing voltage until a field of 4 V/Å is reached

B.2.5 Dosing procedures

1. Set both the tip and counter electrode power supplies to remote

2. Start Labview program and define dosing time

3. Set tip and CE to appropriate voltage

4. Dose appropriate gases. After introducing gases to chamber, press "Start dosing time" button in Labview program. Record max pressure

5. Close valves/stop dosing

6. Top off liquid nitrogen in downtube and wait for pressure to drop to $5-6\times10^{-9}$ torr. Record time required for pressure to drop.

7. Turn on MCPs

8. After turning on MCPs, press "Start experiment" button in Labview.

9. Recording will stop automatically when the experiment is done, turn off tip supply and switch to local, turn off NIM bin, and temperature controller.

B.2.6 Ramp field desorption

1. Set both the tip and counter electrode power supplies to remote

2. Start Labview program and define dosing time

3. Set tip and CE to appropriate voltage

4. Dose appropriate gases. After introducing gases to chamber, press ”Start dosing time” button in Labview program. Record max pressure

5. Close valves/stop dosing

6. Top off liquid nitrogen in downtube and wait for pressure to drop to $5-6\times10^{-9}$ torr. Record time required for pressure to drop.

7. Turn on MCPs

8. After turning on MCPs, press ”Start experiment” button in Labview.

9. Recording will stop automatically when the experiment is done, turn off tip supply and switch to local, turn off NIM bin, and temperature controller.

B.2.7 Pulsed field desorption

1. Set a channel in the delay generator to deliver a TTL pulse and another to deliver a NIM pulse. This can be done by setting the time delay of both channels to the same value and then press the ”FCN” key until the pulse amplitudes appear (the default value is +5 V). Then, move the cursor to the value for D and push the ”+” key until the NIM value appears on the screen.

2. Set both the tip and counter electrode power supplies to manual

3. Set the tip and counter electrode voltages

4. Dose experimental substrate and evacuate substrate reagents

5. Turn on MCPs

6. Connect pulser to the coupling capacitor and start the pulser using the instructions in the manual. For starting the pulses, switch the DDG switch to internal trigger. A green LED should go on and indicate that the DDG is delivering pulses. Also, the WINDOW LED on the PTA should turn on.

7. Dose electrolyte solvent, oxygen, and other species of interest

8. Open PTA histogram program in the old computer. At this point, the CPU LED should go on.

9. Turn on the preamplifier power supply and start recording a few seconds later. This is done by pressing the start button in the PTA program screen.

10. When recording finishes, shut down reagent flow into the chamber and allow pressure to go down. Turn off MCPs.

11. While chamber pumps down, save spectrum following instructions from the user manual. To save the data in a usable format, select all data, go to ”Print Spectrum", and print as file. Then, save the data as a .rpt file. Once this is done, the .rpt file can be extracted using a 3 1/2” floppy disk or a CD.

12. Turn tip towards imaging detector and clean using field desorption. If using carbon, heat up tip and expose to oxygen to remove any residues of the carbon adlayer.

13. For processing the data files, use the ”PFD boxcar integrator” file and save the boxcar integrated data as a csv file. This file can then be opened in Excel for further analysis.

Appendix C

CHARACTERIZATION OF THE WATER ELECTROLYSIS REACTION MECHANISM ON GADOLINIA-DOPED CERIA

Prior to working on the alkali metal-O_2 project, I worked on characterizing water electrolysis on Solid Oxide Electrolysis Cells (SOEC). My work focused on characterizing porous electrodes and thin flims on H_2O-H_2 environments. The work performed on porous electrodes includes both experimental and modeling results, while the thin film work only includes modeling results. This section is an adapted version of References [249] and [250].

C.1 Introduction

A significant challenge in the transition to a renewable energy based economy involves the transition away from a fossil fuel economy in the transportation sector [251]. Such a transition can be achieved through synthesis of liquid fuels using methods such as Fischer-Tropsch (FT) synthesis, where synthesis gas is used to produce hydrocarbons [1]. One route for synthesis gas production involves electrolysis, where H_2O and CO_2 are reacted to form CO and H_2. Electrolysis can be performed on SOECs, where high temperature conductive ceramics are used [252]. Typical materials include a composite of nickel and yttria-stabilized zirconia (Ni/YSZ) and the H_2O/CO_2 electrode, YSZ as the electrolyte, and lanthanum strontium manganite (LSM) as the oxygen electrode [253]. Despite good performance, Ni/YSZ is limited by its low durability, carbon deposition, and sulfur poisoning [254]. An alternative to Ni/YSZ involves the use of mixed ionic and electronic conducting ceramics (MIECs). Some advantages of MIECs include a more efficient use of the electrode (the reaction region is not constrained to the metal/electrolyte/gas three-phase boundary), reduced carbon deposition when used in reducing environments, and stable performance for both hydrocarbon and hydrogen oxidation [254, 255].

Among MIECs, doped ceria has attracted significant interest due to improved performance compared to other materials under similar conditions [254]. Despite a significant body of knowledge regarding the behavior of ceria [254, 256], there is debate regarding the reaction mechanism for water electrolysis. The application of surface science techniques such as ambient pressure XPS (APXPS) to this problem has provided new information about the phenomena occurring in the surface of the electrodes [257, 258]. Zhang and coworkers [257] and Feng et al [258] have reported the use of AP-XPS to study the surface species involved in the reaction. However, there is still controversy regarding the rate-determining step. While Zhang et al proposed dissociative adsorption of water into a hydroxyl group and a neutral hydrogen atom as the rate determining step, Feng et al proposed a dual hydroxyl dissociation as the rate-determining step. The work described in this chapter couples continuum modeling with electrochemical impedance spectroscopy (EIS) to gain further understanding regarding the reaction mechanism.

C.1.1 Electrochemical Impedance Spectroscopy

In EIS, a sinusoidal perturbation in either voltage or current is applied to the sample. A schematic of an EIS experiment is shown in Figure C.1. The upper portion shows an electrochemical system being perturbed using a sinusoidal voltage, plotted as v(t) vs t. The resulting current response, plotted as i(t) vs t, exhibits a different magnitude and phase shift. Impedance is the complex ratio of voltage to current. In a typical EIS experiment, the impedance response is measured as functions of input frequency. Impedance data are typically presented as a function of frequency either in Nyquist or Bode plots. In a Bode plot, the magnitude and phase shifts are plotted as functions of frequency, while Nyquist plots show the imaginary component plotted against the real component, parametric with frequency [104]. A sample Nyquist plot is shown in the lower portion of Figure C.1. An advantage of EIS is its capability to isolate processes by time scale [259]. However, EIS is a linear technique and therefore, cannot distinguish between different non-linear rate laws [260, 261]. The common example of such a limitation is the presence of Gerischer-like behavior, where diffusion and reaction kinetics are co-limiting, which can be associated to multiple mechanisms with the proper choice of fitting parameters. In addition, partial pressure dependence

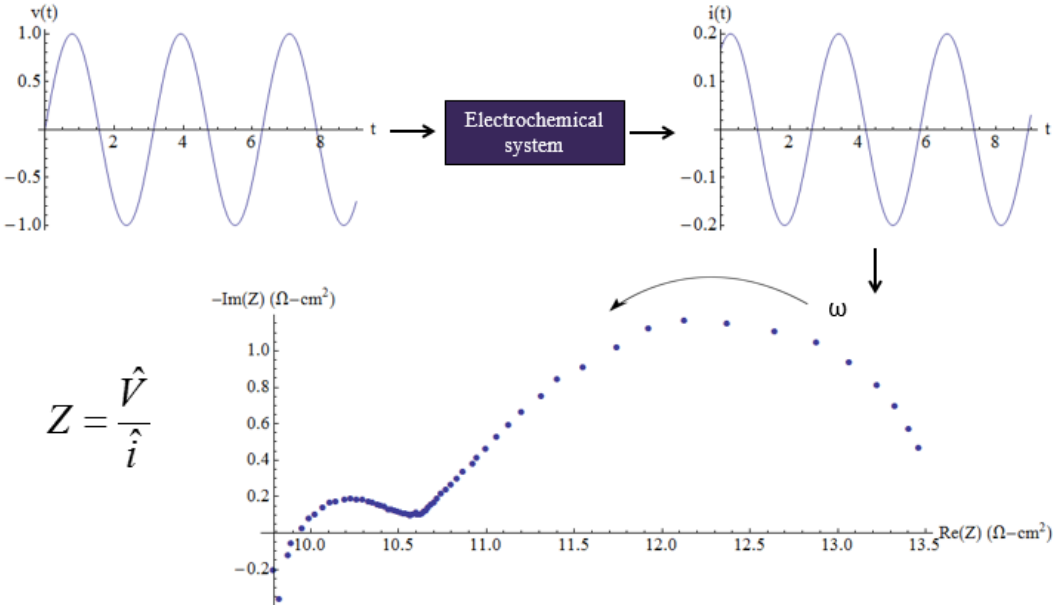

Figure C.1: Graphical depiction of EIS. The upper portion shows an electrochemical system being perturbed using a sinusoidal voltage, v(t). The system response is shown as i(t). The resulting Nyquist plot is shown in the lower portion, with the equation for impedance being show to the elft of the Nyquist plot.

can be problematic since multiple rate-determining steps can show similar trends.

An alternative to EIS is to use a non-linear variant of this technique, known as non-linear EIS (NLEIS) [261]. NLEIS has proven capable of isolating complex reaction mechanisms. A schematic of an NLEIS experiment is shown in Figure C.2. The upper part of the figure shows an electrochemical system undergoing a sinusoidal voltage perturbation. In contrast to EIS, NLEIS experiments measure the impedance response as a function of frequency and perturbation amplitude. For sufficiently large amplitudes, the response will exhibit higher order harmonics that can be extracted through Fourier analysis. This can be observed in Figure C.2, where the current response, i(t), is a . The higher order harmonic responses are unique for a mechanism and therefore,

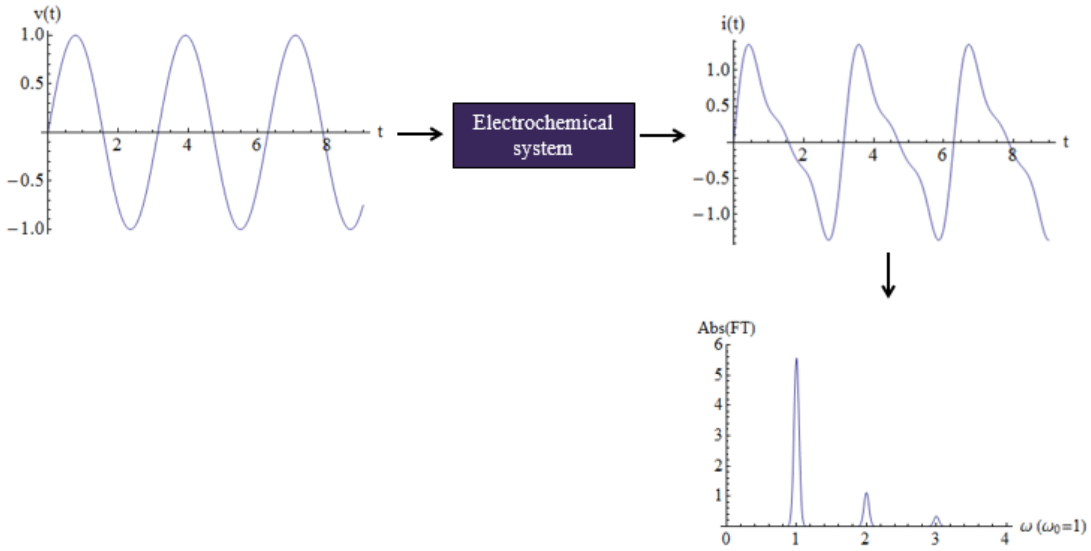

Figure C.2: Graphical depiction of NLEIS. The upper portion shows an electrochemical system being perturbed using a sinusoidal voltage, v(t). The system response is shown as i(t). The Fourier transform magnitude of the current, Abs(FT), plot is shown below as a function of the harmonic order.

NLEIS can be used to determine likely reaction mechanisms when coupled with a reaction model. Wilson et al [261] performed experiments on oxygen reduction and showed that NLEIS can isolate distinct features for determination of the rate law governing O_2 reduction, thus providing insights about the reaction mechanisms. Those authors showed that, even though some mechanisms might have the same linear response, their non-linear responses differ and therefore, NLEIS can be used to identify a reaction mechanism.

C.2 Experimental Methods

C.2.1 Sample preparation

Symmetrical GDC button cells were prepared with a screen printing method on YSZ (Zircar) pellets. The pellets were made by pressing YSZ powder at 3500 psi with a cylindrical die. The resulting pellets were then sintered at 1600 °C for 2 h using 2 °C/min heating and cooling ramps. The GDC ink was fabricated using the procedure outlined by Green [262]. Specifically, GDC powder (Praxair) was mixed with α-terpineol, ethyl cellulose, and oleic acid using a three-roll mill. Glassy carbon beads were then added to the resulting mixture, followed by ball milling. GDC electrodes were then screen printed on the YSZ electrolyte pellets and fired using the procedure described by Green [262]. A SEM image of a cell is shown in Figure C.3. The resulting electrodes were porous with a thickness of about 5 μm.

C.2.2 Experimental Procedure

A schematic of the experimental setup is shown in Figure C.4. For electrochemical measurements, the cells were placed in a Probostat and heated to temperature. EIS measurements were made with a Solartron 1287 potentiostat at zero bias, a frequency range of 0.01 to 10,000 Hz, and perturbation amplitude of 10 mV. Measurements were performed for both symmetrical and half-cell configurations. Once a stable profile was achieved, NLEIS was performed with a sinusoidal current input at zero DC bias, a frequency range of 0.02 to 10,000 Hz, and 20 amplitudes per frequency ranging from 0.1 mA to 1.5 mA. The limits for each specific case were established such that there a visible fifth order harmonic. In both cases, a total gas flow of 100 sccm was used. The cells were tested at 700, 750 and 800 °C under different hydrogen and water concentrations, listed in Table C.1. Experimental results were fitted using a macrohomogenous model (more details in the modeling section) and analyzed using previously outlined protocols [261].

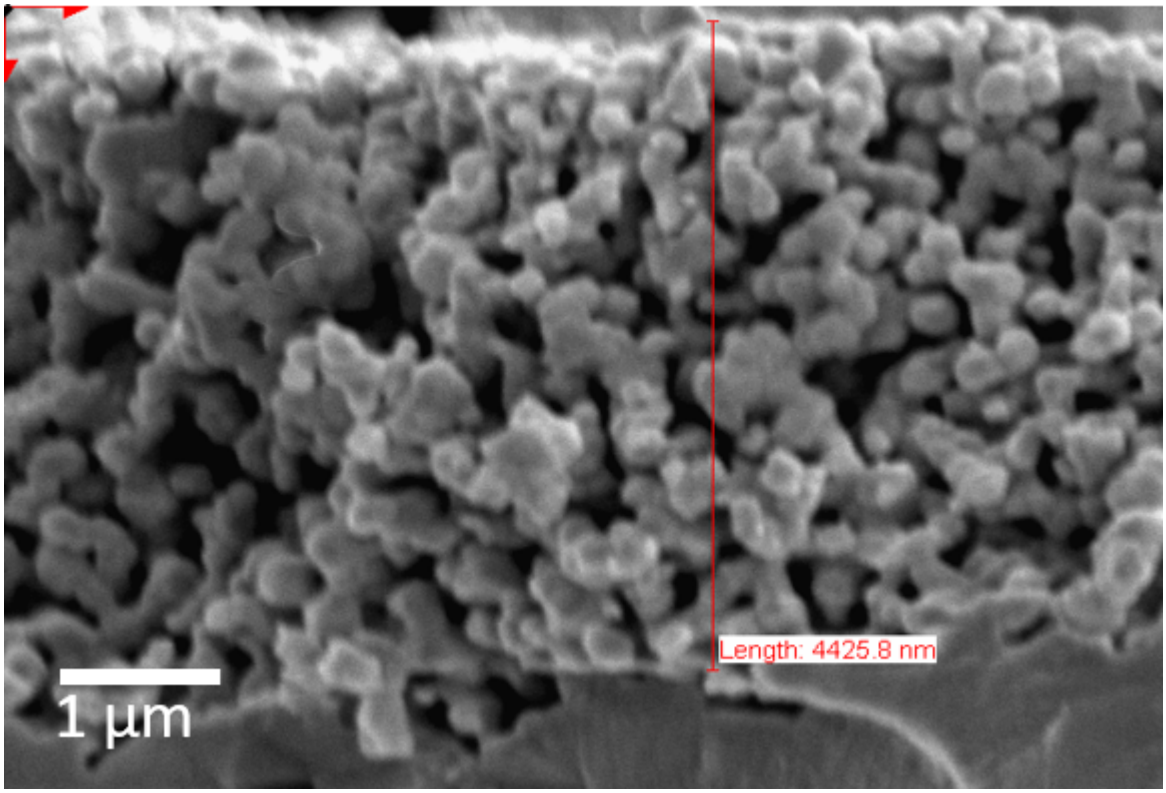

Figure C.3: SEM image of a porous GDC-10 electrode on a YSZ electrolyte substrate before electrochemical characterization. The electrode was fired at a temperature of 1200 °C for 2 h.

Hydrogen content (%)	Water content (%)	p_{O2} (bar) at 750 ° C	p_{O2} (bar) at 800 ° C
97	3	2.79×10^{-23}	4.07×10^{-22}
50	3	1.11×10^{-22}	1.63×10^{-21}
25	3	4.76×10^{-22}	6.51×10^{-21}
10	3	2.79×10^{-21}	4.76×10^{-20}
5	3	1.11×10^{-20}	1.63×10^{-19}

Table C.1: EIS/NLEIS experimental conditions. The effective p_{O2} values were determined using the thermodynamic model proposed by Yashiro et al. [256]

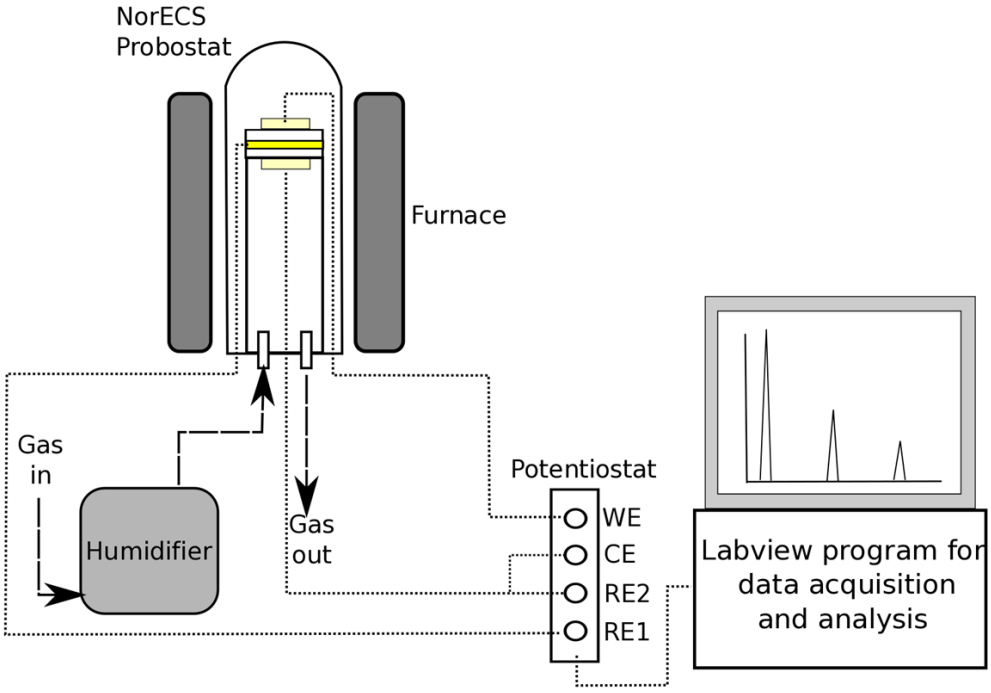

Figure C.4: Experimental setup for impedance experiments. The electrode was fired at a temperature of 1200 °C for 2 h.

C.3 Model descriptions

C.3.1 Reaction models

Reaction rate expressions were derived using the theoretical framework proposed by Adler et al. [260]. The mechanisms proposed by Zhang et al. (referred to as Mechanism 1) [257] and Feng and co-workers (referred to as Mechanism 2) [258] were considered and are depicted in Fig. C.5. Mechanism 1 is composed of 4 steps: water dissociative adsorption to form an adsorbed hydrogen atom and a hydroxyl group involving electron transfer (step 1), hydroxyl dissociation to form an adsorbed hydrogen atom and an oxygen ion involving electron transfer (step 2), adsorbed hydrogen atom association and evolution of hydrogen gas from the surface (step 3), and oxygen ion incorporation into the bulk (step 4). In Mechanism 1, step 1 is considered the rate determining step. Meanwhile, Mechanism 2 is composed of 6 steps: water adsorption onto a vacancy (step 1), water dissociation to form two hydroxyl groups (Step 2), hydroxyl dissociation into two adsorbed hydrogen atoms and 2 oxygen ions involving electron transfer (step 3), adsorbed hydrogen atom association to form an adsorbed hydrogen molecule (step 4), hydrogen evolution (step 5), and oxygen ion incorporation into the bulk. In this case, the rate determining step is a combination of steps 3, 4, and 5.

The rate expression is determined using the formalism developed by Adler et al [260]. The generic rate expression is provided by Equation C.1, where r_i is the rate for a particular step, $\Re_i$ is a kinetic function that depends on the thermodynamic conditions of the gas and solid, and Λ_i is the thermodynamic driving force [249].

$$r_i = \Re_i \left[1 - \exp \frac{\Lambda_i}{RT} \right] \tag{C.1}$$

C.3.2 Thermodynamics

Thermodynamics were described using a point-defect model [256]. The effect of the gas environment on equilibrium vacancy concentration can be determined using a thermodynamic factor, A. In a scenario where the surface exhibits a different thermodynamic behavior, the surface ther-

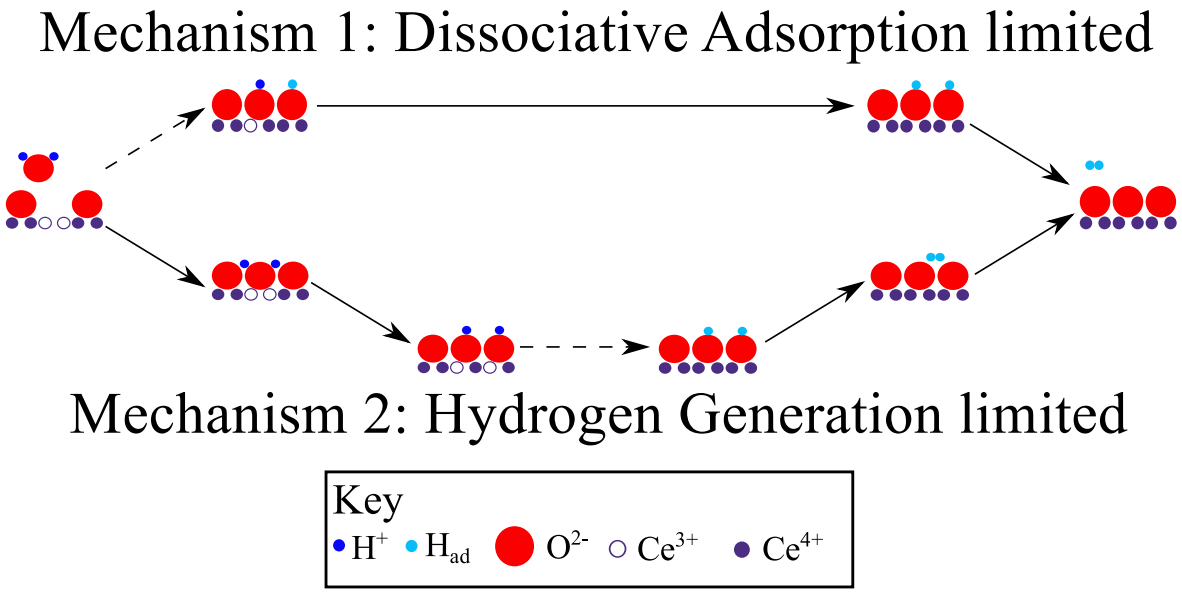

Figure C.5: Reaction mechanisms proposed by Zhang et al. (left) and Feng et al. (right). The rate-determining step proposed by the authors in each case is shown as a dashed arrow.

modynamic factor is referred as A_s. The factor is defined in Equation C.2, where $P_{O_2,eff}$ is the equilibrium oxygen partial pressure, x_v is the vacancy concentration, x_{v_0} is the equilibrium vacancy concentration, and ψ is a dimensionless vacancy concentration perturbation, defined by Equation C.3.

$$A = -\frac{1}{2}\frac{\delta P_{O_2,eff}}{\delta \ln x_v} = 1 + \frac{8x_{v,0}(\psi+1)}{4x_{v,0}(\psi+1)-x} + \frac{8x_{v,0}(\psi+1)}{1-4x_{v,0}(\psi+1)} \tag{C.2}$$

$$\psi = \frac{x_v - x_{v,0}}{x_{v,0}} \tag{C.3}$$

where $P_{O_2,eff}$ is the equilibrium oxygen partial pressure. Some modeling scenarios assume that the bulk and surface vacancy concentrations are different. In such cases, Equation C.4 is used to describe the relationship between the bulk and surface thermodynamic factors, where *i* can refer to either vacancies or electrons.

$$A d\ln x_i = A_s d\ln x_{i,s} \tag{C.4}$$

C.3.3 Porous electrodes

The experimental results were analyzed using a 1D macrohomogeneous model using the approach proposed by Adler et al [263]. The phenomena considered in the model are shown in Figure C.6. In addition, the model considers an increased surface vacancy concentration compared to that of the bulk.

The dimensionless equations for the model are shown below. Equation (C.5) describes the dimensionless vacancy balance. Vacancy fluxes, N_v, at the electrode/electrolyte interface (y=0) and the electrode/gas interface (y=L) are used as the boundary conditions and are given by Equations (C.6) and (C.7). Meanwhile, the dimensionless voltage is given by Equation (C.8).

$$\frac{\delta \psi}{\delta t} = \nabla \cdot [A \nabla \psi] - r_i \tag{C.5}$$

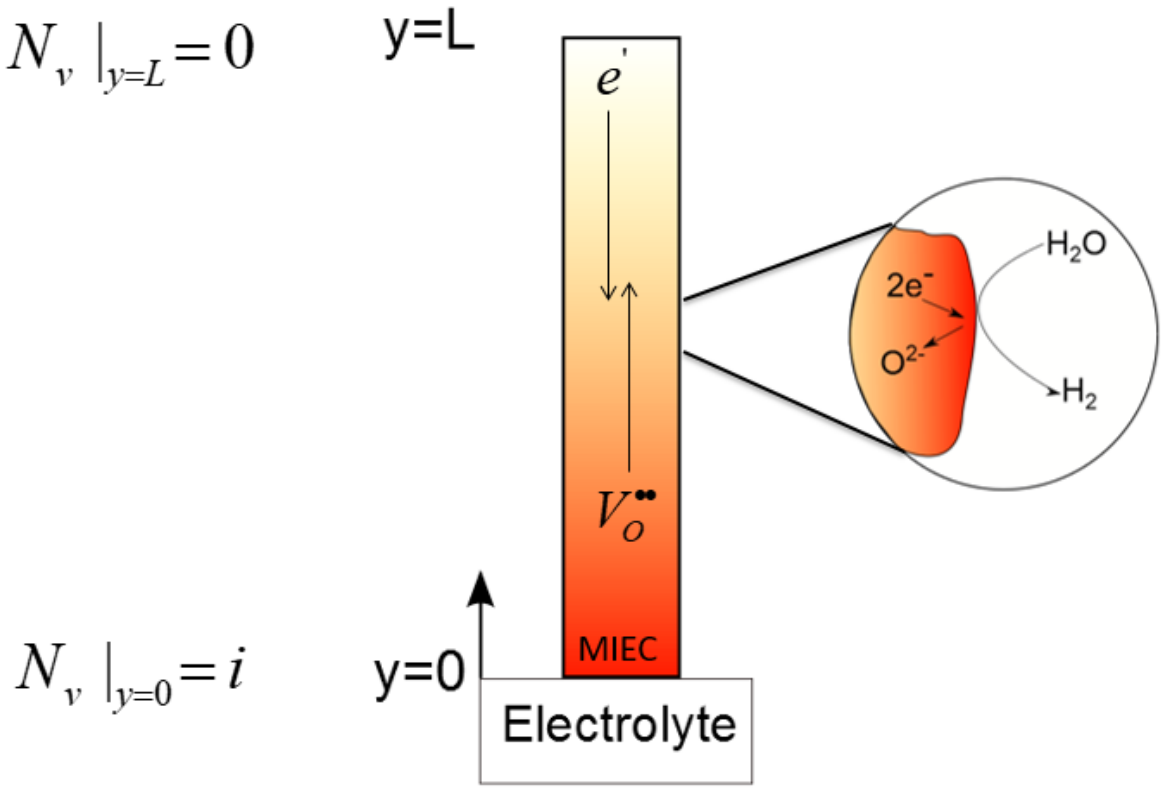

Figure C.6: Schematic of the model system. Water is assumed to be reduced to H_2 at the ceria surface, consuming 2 e^- and producing an oxygen ion in the bulk. Ion transport to the electrolyte occurs through diffusion. Boundary conditions for ion transport are shown at the electrolyte/MIEC interface (y=0) and current collector/MIEC interface (y=L)

$$N_{v,y=0} = A\left(\frac{\delta\psi}{\delta\xi}\right)_{\xi=0} = \alpha\cos(\sigma\tau) \tag{C.6}$$

$$N_{v,y=1} = 0 \tag{C.7}$$

$$U = \ln\left(\frac{(1-4x_{v,0})^2(4x_{v,0}(\psi+1)-x)^2(\psi+1)}{[(4x_{v,0}-x)^2(1-4x_{v,0}(\psi+1))]^2}\right)_{\xi=0} \tag{C.8}$$

where ξ is the dimensionless position, τ is the dimensionless time, σ is the dimensionless frequency, α is the current perturbation amplitude, and r_i is the reaction rate. The definitions for each variable are given in Equations (C.9)-(C.12).

$$\xi = \frac{y}{L} \tag{C.9}$$

$$\sigma = \omega t* \tag{C.10}$$

$$\tau = \frac{t}{t*} \tag{C.11}$$

$$\alpha = \frac{i}{i*} \tag{C.12}$$

where ω is the dimensional frequency and L is the electrode thickness. κ, dimensional characteristic time (t^*), and current (i^*) are defined in Equations (C.13)-(C.15).

$$\kappa = \frac{a\tau_s\Re_i L^2}{x_{v0}c_O D_v(1-\varepsilon)A_0} \tag{C.13}$$

$$t^* = \frac{L^2\tau_s}{D_v A_0} \tag{C.14}$$

$$i^* = 2F\frac{x_{v0}c_O(1-\varepsilon)D_v}{\tau_s L} \tag{C.15}$$

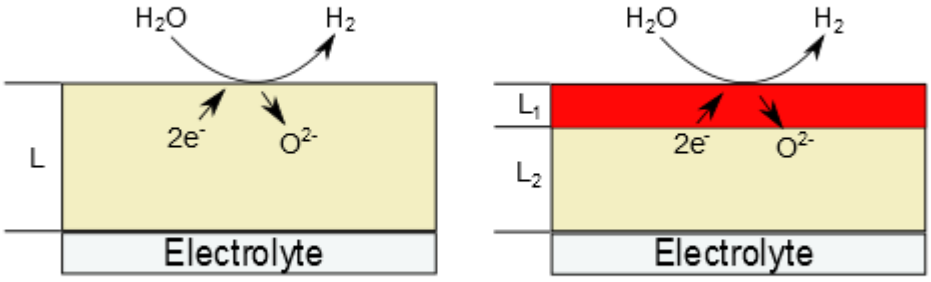

Figure C.7: Schematic of a thin film. The left inset shows the model system assuming a uniform film, while the right inset shows the model system when an ehnaced polaron (electron) concentration is observed. The surface region is shown in red.

where D_v is the bulk vacancy diffusivity, ε is the electrode porosity, τ_s is the electrode tortuosity, c_O is the concentration of oxygen vacancy sites, A_0 is the thermodynamic factor evaluated at $x_v = x_{v,0}$, and a is the electrode surface area.

C.3.4 Thin film models

The model system is shown in Figure C.7. A stirred tank approach proposed by Wilson et al [264] was used to predict the non-linear harmonic response. Two scnearios were considered: one where the surface and the bulk have the same composition and the other where bulk and surface have different compositions. In contrast to the porous electrode model, electron concentration x_e was used as the state variable.

The electron balance of the uniform scenario is shown in Equation C.16, where χ is the dimensionless electron concentration perturbation, defined in Equation C.17. Meanwhile, x_{e0} is the equilibrium electron concentration and x_e is the electron concentration.

$$\frac{\delta\chi}{\delta t} = N_{e,\xi=0} - N_{e,\xi=1} = \alpha\cos(\sigma\tau) - r_i \tag{C.16}$$

$$\chi = \frac{x_e - x_{e,0}}{x_{e,0}} \tag{C.17}$$

The electron balance for the surface-enhanced scenario is shown in Equation C.18, where γ is the fraction of the film that contains an increased concentration of electrons, χ_s is the perturbation variable in the surface, and $x_{e0,s}$ is the concentration of electrons in the surface.

$$(1-\gamma)\frac{\delta\chi}{\delta t} + \gamma\frac{x_{e0,s}}{x_{e0}}\frac{\delta\chi_s}{\delta t} = N_{e,\xi=0} - N_{e,\xi=1} = \alpha\cos(\sigma\tau) - r_i \tag{C.18}$$

In addition to the 2 rate-limiting scenarios described previously, a third limiting step was explored in the thin film work. Such a step involves hydroxyl dissociation (step 2 in Mechanism 1) as rate-determining.

C.4 Results and Discussion

C.4.1 Porous electrodes

EIS plots are shown in Figure C.8. At high frequency, an inductive tail attributed to electrical connections appears as a line with a positive imaginary component. This is followed by 2 arcs: a high frequency arc attributed to electrode-electrolyte interfacial processes and a low frequency arc attributed to reactions and oxygen transport across the material. The chemical feature exhibits a Gerischer-like (teardrop) shape feature at high hydrogen contents, attributed to a co-limitation of vacancy diffusion and reaction kinetics [249]. As the hydrogen content decreased, the chemical features started to adopt a semicircular-like shape. Such a shape can be attributed to kinetic limitations at lower hydrogen contents, leading to the observed semicircular-like shape [263].

The change in shape as a function of decreased hydrogen content was included in the model using an adjustable parameter called κ, defined as the ratio between the reaction and bulk vacancy diffusion rates. Figure C.9 shows the effect of κ in the concentration profiles throughout the electrode. When κ is small, the vacancy concentration throughout the electrode thickness is nearly uniform and the electrode is kinetically limited. This is observed in EIS as a semicircular spectrum, shown in blue on Figure C.9. As κ increases, concentration gradients start to develop in the

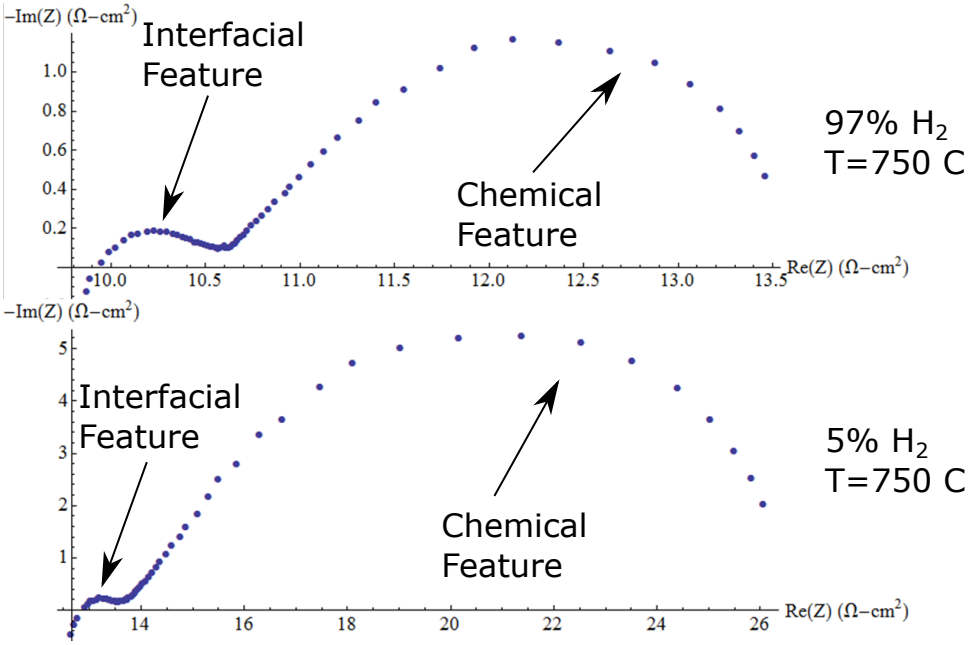

Figure C.8: EIS results for a porous electrode. Water is assumed to be reduced to H_2 at the ceria surface, consuming 2 e^- and producing an oxygen ion in the bulk. Ion transport to the electrolyte occurs through diffusion.

electrode and a diffusion tail (45° degree straight line) appears at high frequency in EIS spectra. Such a spectrum is shown in red. Finally, as κ approaches infinity, concentration gradients are confined to the electrode/electrolyte interface and only a small portion of the electrode is active. This manifests in EIS spectra as a Gerischer (teardrop-like) impedance, shown in green in Figure C.9 [265].

Figure C.10 shows experimental NLEIS results with model fits for the 2 different reaction scenarios proposed in Figure C.5. The left side of the figure shows plots for U22, the second harmonic response. Meanwhile, the right side shows U33, the third harmonic response. In all cases, phasor lines drawn from the origin to ω_{peak}/n are shown, where ω_{peak} is the frequency at which the imaginary component of the EIS response reaches its maximum and n is the harmonic number. For example $n=2$ for the second harmonic. The results show that Mechanism 2 can capture the shape and qualitative trends of the experimental spectra. However, the model predicts a smaller U22 response for $y_{H2}=0.97$ and $y_{H2}=0.25$. In addition, the model fails to capture the low frequency behavior for U33, where the experimental spectra exhibit a low frequency tail in the first quadrant. Further refinement of the model can be achieved by adding multidimensional transport, as well as treating the surface as a double layer instead of just using a thermodynamic equilibrium expression to describe surface enhancement. Another alternative involves performing experiments on thin films. Such an approach would allow to characterize reaction kinetics without seeing the effect of transport limitations. In addition to the models done for porous electrodes, work was done in modeling impedance response on thin film electrodes and studying the effects of surface enhancement in the system [249].

C.4.2 Thin film models

Figure C.11 shows the predicted EIS response for the 2 possible mechanisms. The response is scaled such that the maximum value of the real component has a mangitude of 1. Both EIS spectra have the same shape and magnitude, showing that it is not possible to distinguish between rate laws by only looking at the linear response.

Figure C.12 shows predicted second and third harmonic responses for the different rate-limiting

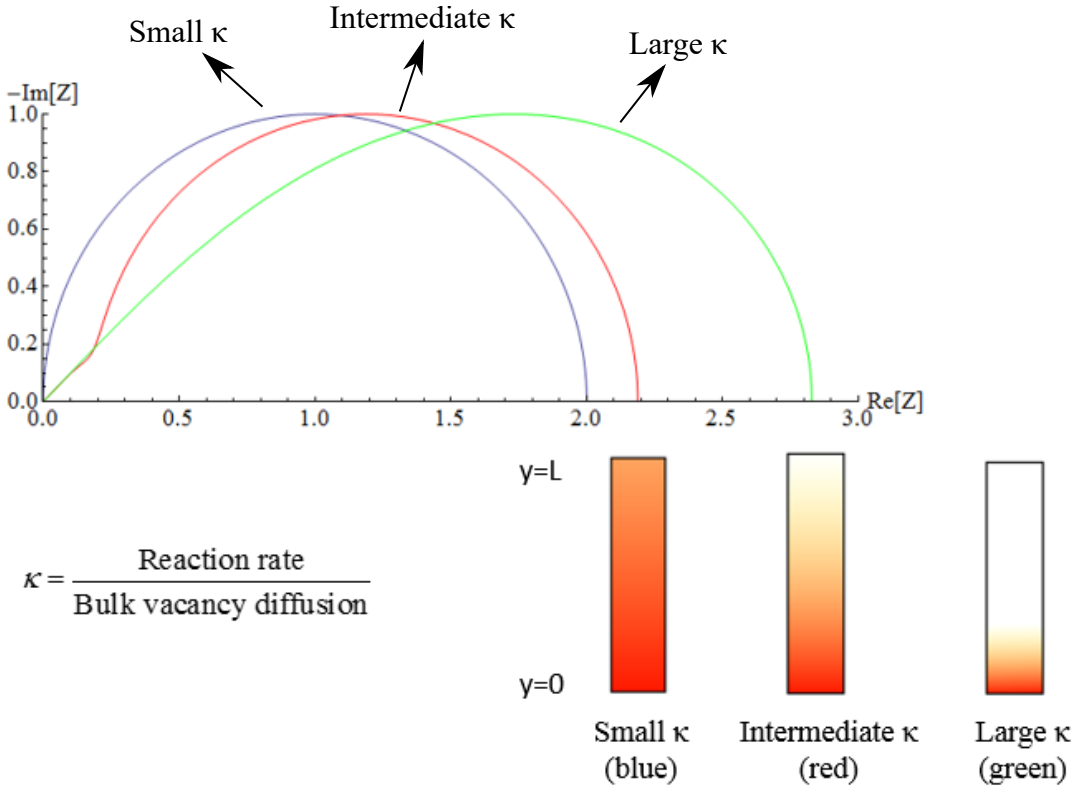

Figure C.9: Effect of κ in impedance spectra and concentration profiles. The upper left corner shows dimensionless Nyquist plots for different values of κ. Low κ is shown in blue, medium κ is shown in red, and infinitely large κ is shown in green. The bottom left corner shows concentration profiles for different values of κ. Areas shown in red have higher concentration of vacancies, while areas with depleted vacancy concentration are shown in white.

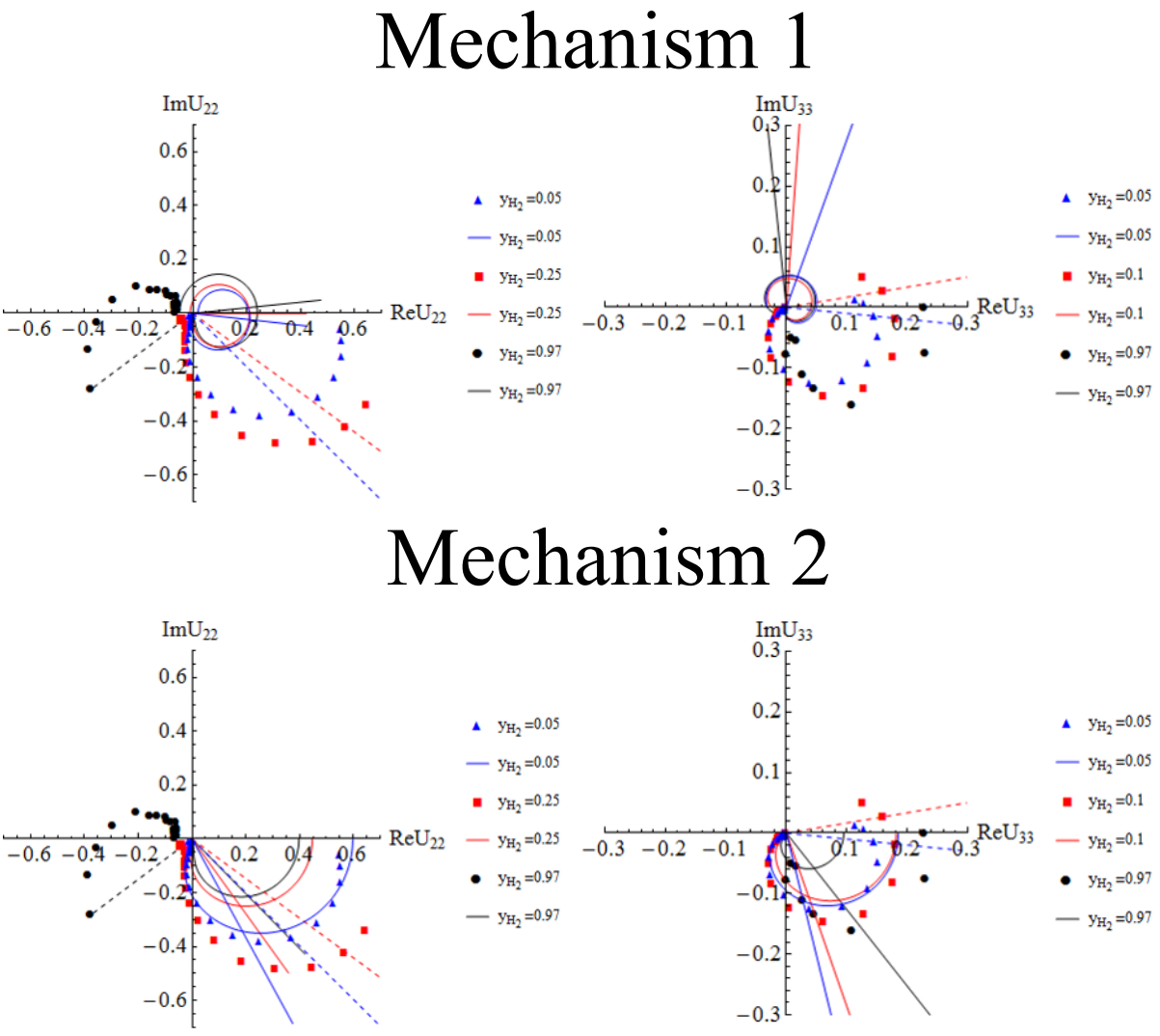

Figure C.10: NLEIS results for a porous electrode. In all cases, experimental results are shown as symbols and model fits are shown as lines. The plots on the left show the second harmonic, while those on the right show the third harmonic.

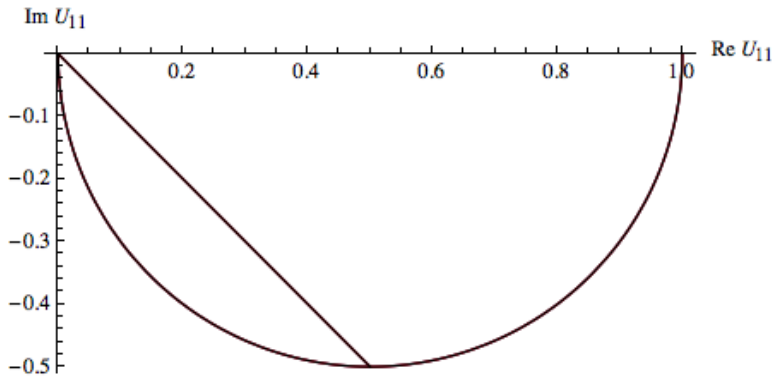

Figure C.11: Scaled EIS results for the thin film models.

scenarios. The modeling results show that it is possible to distinguish between the 3 mechanisms using NLEIS. Figure C.13 shows the effect of surface enhancement in the predicted spectra. Both the hydroxyl dissociation-limited and Mechanism 1 scenarios show drastic changes in spectra shape upon inclusion of surface enhancement. Meanwhile, Mechanism 2 exhibits minimal shape differences, with the only changes occuring in the relative magnitudes of the real and imaginary components. The changes that occur upon inclusion of surface enhancement are not affected by the thickness of the surface layer [250].

C.5 Outlook

The work presented in this section provided a basis for the use of NLEIS towards characterizing water electrolysis in high temperature ceramics. However, further refinements are needed. First, the model used to describe water electrolysis cannot provide a good fit to the experimental results. The model can be improved by including additional features such as multidimensional transport [265] or developing a more accurate model for describing the surface behavior that takes space-charge effects into account. In addition, an important assumption of the Adler-Lane-Steele model used in this work is a unity electronic transference number [263]. However, doped ceria has non-unity transference number in many of the experimental conditions used in this study [266]. Therefore, it

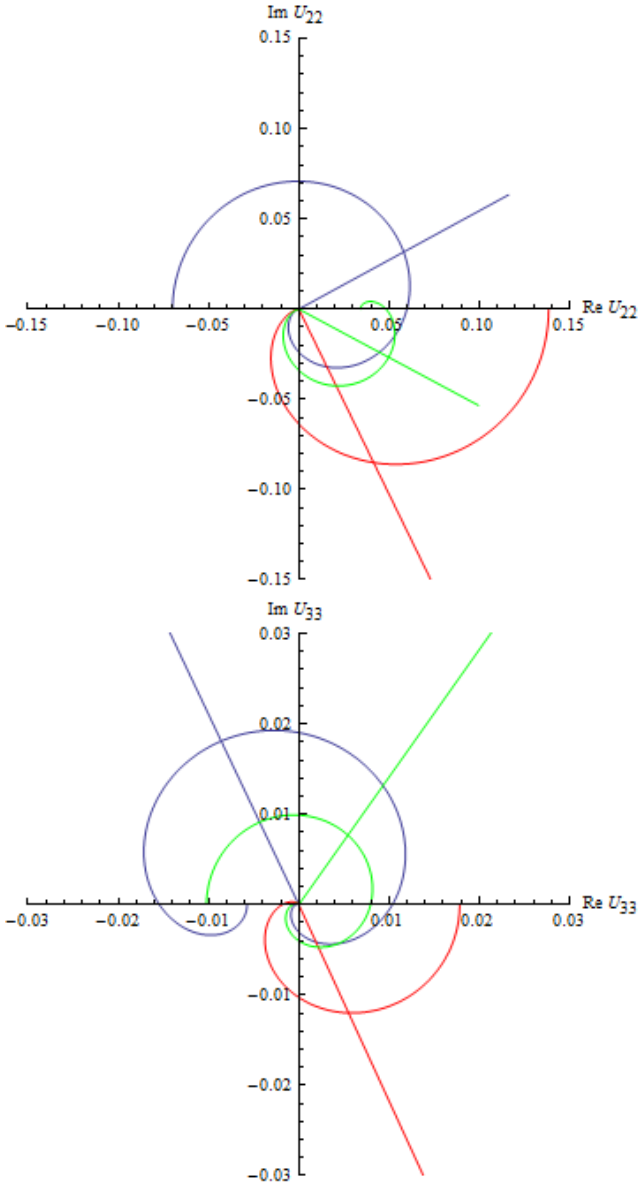

Figure C.12: NLEIS results for a uniform, thin film model with $A_0 = 1.2$. The upper plot shows the predicted second harmonic and the bottom plot shows the predicted third harmonic response. In all cases, the blue spectrum corresponds to Mechanism 1, the green spectrum corresponds to Mechanism 2, and the red spectrum corresponds to the hydroxyl dissociation-limited scenario.

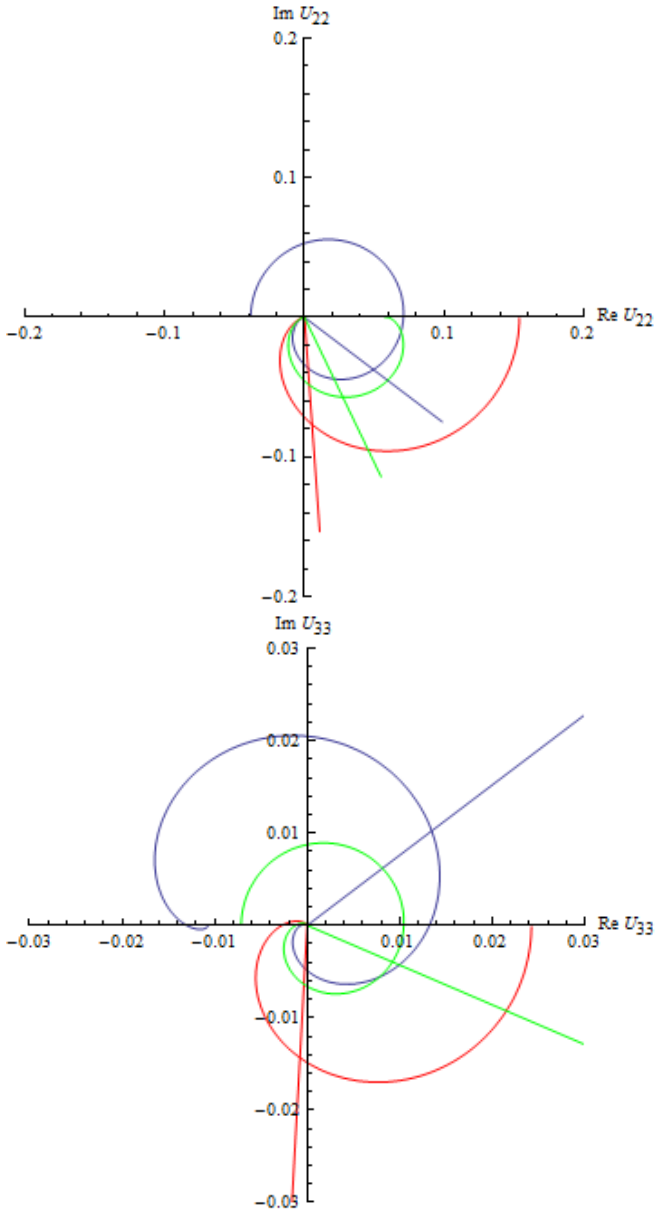

Figure C.13: NLEIS results for a thin film model with enhanced electron concentration in the surface with $A_0 = 1.2$ and $\gamma = 0.001$. The upper plot shows the predicted second harmonic and the bottom plot shows the predicted third harmonic response. In all cases, the blue spectrum corresponds to Mechanism 1, the green spectrum corresponds to Mechanism 2, and the red spectrum corresponds to the hydroxyl dissociation-limited scenario.

is necessary to include gradients in electron chemical potential [263]. In addition, thin film experiments are necessary to determine the likely rate-limiting step. The thin film model described in this chapter provides further confirmation that NLEIS can distinguish between different rate-limiting scenarios, as well as surface enhancement effects.

VITA

Honorio Valdés Espinosa de los Monteros was born on September 13, 1989 in El Paso, TX. He grew up in Querétaro, Mexico and started college in 2007 at the University of Connecticut. He graduated with Bachelor of Science degrees in Biomedical Engineering and Chemical Engineering in 2012. Upon graduation, he started graduate school in the Department of Chemical Engineering at the University of Washington, obtaining his Master of Science degree in 2015.